The Astrophysical Journal Supplement Series, 282:2 (46pp), 2026 January https://doi.org/10.3847/1538-4365/ae0e61
© 2025. The Author(s). Published by the American Astronomical Society.
OPEN ACCESS

FIELDMAPS Data Release: Far-infrared Polarization in the "Bones" of the Milky Way

Simon Coudé[1,2,3], Ian W. Stephens[1], Philip C. Myers[2], Nicole Karnath[2,4], Howard A. Smith[2], Andrés E. Guzmán[5], Jessy Marin[2,6], Catherine Zucker[2], B.-G. Andersson[7], Zhi-Yun Li[8], Leslie W. Looney[9], Giles Novak[10,11], Thushara G. S. Pillai[12], Sarah I. Sadavoy[13], Patricio Sanhueza[14], and Archana Soam[15]
[1] Department of Earth, Environment, and Physics, Worcester State University, Worcester, MA 01602, USA; simon.coude@nao.ac.jp
[2] Center for Astrophysics | Harvard & Smithsonian, 60 Garden Street, Cambridge, MA 02138, USA
[3] National Astronomical Observatory of Japan, National Institute of Natural Sciences, 2-21-1 Osawa, Mitaka, Tokyo 181-8588, Japan
[4] Space Science Institute, 4765 Walnut St, Suite B, Boulder, CO 80301, USA
[5] Joint Alma Observatory (JAO), Alonso de Córdova 3107, Vitacura, Santiago, Chile
[6] Jodrell Bank Centre for Astrophysics, Department of Physics and Astronomy, The University of Manchester, Manchester, M13 9PL, UK
[7] McDonald Observatory and Department of Astronomy, University of Texas at Austin, Austin, TX 78712, USA
[8] Astronomy Department, University of Virginia, Charlottesville, VA 22904, USA
[9] Department of Astronomy, University of Illinois, 1002 West Green Street, Urbana, IL 61801, USA
[10] Center for Interdisciplinary Exploration and Research in Astrophysics (CIERA), 1800 Sherman Avenue, Evanston, IL 60201, USA
[11] Department of Physics & Astronomy, Northwestern University, 2145 Sheridan Road, Evanston, IL 600208, USA
[12] Haystack Observatory, Massachusetts Institute of Technology, 99 Millstone Road, Westford, MA 01886, USA
[13] Department of Physics, Engineering Physics and Astronomy, Queen's University, Kingston, ON K7L 3N6, Canada
[14] Department of Astronomy, School of Science, The University of Tokyo, 7-3-1 Hongo, Bunkyo, Tokyo 113-0033, Japan
[15] Indian Institute of Astrophysics, II Block, Koramangala, Bengaluru 560034, India
Received 2025 January 30; revised 2025 September 12; accepted 2025 September 28; published 2025 December 15

Abstract

Polarization observations of the Milky Way and many other spiral galaxies have found a close correspondence between the orientation of spiral arms and magnetic field lines on scales of hundreds of parsecs. This paper presents polarization measurements at 214 μm toward 10 filamentary candidate "bones" in the Milky Way using the High-resolution Airborne Wide-band Camera on the Stratospheric Observatory for Infrared Astronomy. These data were taken as part of the Filaments Extremely Long and Dark: A Magnetic Polarization Survey and represent the first study to resolve the magnetic field in spiral arms at parsec scales. We describe the complex yet well-defined polarization structure of all 10 candidate bones, and we find a mean difference and standard deviation of $-74° \pm 32°$ between their filament axis and the plane-of-sky magnetic field, closer to a field perpendicular to their length rather than parallel. By contrast, the 850 μm polarization data from Planck on scales greater than 10 pc show a nearly parallel mean difference of $3° \pm 21°$. These findings provide further evidence that magnetic fields can change orientation at the scale of dense molecular clouds, even along spiral arms. Finally, we use a power law to fit the dust polarization fraction as a function of total intensity on a cloud-by-cloud basis and find indices between -0.6 and -0.9, with a mean and standard deviation of -0.7 ± 0.1. The polarization, dust temperature, and column density data presented in this work are publicly available online.

Unified Astronomy Thesaurus concepts: Interstellar filaments (842); Star formation (1569); Milky Way magnetic fields (1057); Dust continuum emission (412); Far infrared astronomy (529); Polarimetry (1278)

1. Introduction

Far-infrared and radio observations of nearby spiral galaxies have shown a close relationship between the orientation of magnetic field lines and the structure of spiral arms (e.g., A. S. Borlaff et al. 2021; E. Lopez-Rodriguez et al. 2021; A. S. Borlaff et al. 2023; S. Martin-Alvarez et al. 2024). Generally, spiral arms are hosts to regions of high-mass star formation, which themselves provide feedback (e.g., supernovae) that contributes to maintaining and amplifying the galactic magnetic field through turbulence-driven dynamos (see R. Beck 2015; and references therein). In turn, the process of star formation, which occurs within filamentary molecular clouds, may itself be regulated by this magnetic field at small scales (e.g., P. André et al. 2014; K. Pattle et al. 2023). Characterizing magnetic fields at multiple scales within spiral galaxies can therefore improve our insights into their evolution.

Original content from this work may be used under the terms of the Creative Commons Attribution 4.0 licence. Any further distribution of this work must maintain attribution to the author(s) and the title of the work, journal citation and DOI.

Within the Milky Way, our own barred spiral galaxy (e.g., T. M. Dame et al. 2001; J. S. Urquhart et al. 2014), the large-scale magnetic field projected on the plane of the sky is found to be mostly parallel to the Galactic disk as seen by the Planck Space Telescope at the scale of the clouds themselves (Planck Collaboration et al. 2015a). This parallel orientation agrees well with the signatures seen in other spiral galaxies (T. J. Jones et al. 2020; A. S. Borlaff et al. 2021), suggesting that magnetic field lines follow spiral arms. Indeed, such a signature in the plane of the sky can exist at large scales even if, in 3D, the field itself has a significant line-of-sight component, such as helical geometry with observable polarity reversals (M. Tahani 2022). Unfortunately, at the scales probed by Planck ($>5'$ at 850 μm), it is not possible to resolve the magnetic field within the filaments where star formation occurs, even within the solar neighborhood (<500 pc). Furthermore, our point of view within the Galactic disk complicates the identification of star-forming regions associated with specific spiral arms (e.g., C. Zucker et al. 2015).

Infrared-dark clouds (IRDCs) in particular are a class of dense and cold molecular clouds that appear to trace spiral arms well. They are opaque in the mid-infrared and often

elongated in shape (M. Perault et al. 1996; S. J. Carey et al. 1998, 2000; M. P. Egan et al. 1998; P. Hennebelle et al. 2001; S. D. Price et al. 2001; R. A. Benjamin et al. 2003; S. J. Carey et al. 2009; N. Peretto & G. A. Fuller 2009), and they are candidate progenitors of high-mass star formation (T. Pillai et al. 2006a; J. M. Jackson et al. 2010; P. Sanhueza et al. 2012; J. C. Tan et al. 2014; P. Sanhueza et al. 2019; K. Morii et al. 2023). Based on the observed properties of the best-known IRDCs, A. A. Goodman et al. (2014) proposed that this category of objects could be the "bones" of the Galaxy, which are giant molecular structures closely following the "spines" of spiral arms in both position and velocity space. Only a few dozen filaments have been determined to be potential bone candidates (K. Wang et al. 2016; C. Zucker et al. 2018). Bones were further studied using simulations, but it was not possible to recover their observed lengths and widths without including magnetic fields and self-gravity (C. Zucker et al. 2019).

Since the thermal emission of interstellar dust in IRDCs peaks in the far-infrared (K. Wang et al. 2015), it is an ideal wavelength regime to characterize their magnetic fields through measurements of dust polarization (K. Pattle & L. Fissel 2019). Indeed, in most of the interstellar medium, spinning asymmetric dust grains with paramagnetic properties will have their long axis preferentially aligned to be perpendicular to magnetic field lines, as long as they are within an anisotropic radiation field. This mechanism, known as radiative alignment torques (RATs), is responsible for partially polarizing their thermal emission (A. Lazarian & T. Hoang 2007; T. Hoang & A. Lazarian 2008). Alternative mechanisms, such as radiative alignment without magnetic fields (k-RAT), can also theoretically polarize dust emission in the far-infrared and submillimeter, but evidence for these mechanisms has only been found in a limited number of extreme environments (e.g., K. Pattle et al. 2021; B. G. Andersson et al. 2024). In the typical case of optically thin dust emission in molecular clouds, the plane-of-sky component of the magnetic field can be inferred from observed polarization maps at far-infrared and millimeter wavelengths (approximately 50 μm to 3 mm) by rotating the polarization vectors by 90° (e.g., B. G. Andersson et al. 2015).

An important discovery from Planck dust polarization maps of nearby star-forming regions is that the Galactic magnetic field structure appears to change direction toward molecular clouds whose hydrogen column density N_{H_2} is above 10^{21} cm^{-2} (Planck Collaboration et al. 2016). Indeed, magnetic field lines in these clouds tend to be perpendicular to the length of dense filaments (e.g., N. L. Chapman et al. 2011; Y. Doi et al. 2020; A. Kaminsky et al. 2023). This property has been extensively studied using magnetohydrostatic models (K. Tomisaka 2014, 2015). In contrast, lower-density striations have been observed to follow magnetic field lines into self-gravitating filaments, potentially funnelling gas toward star-forming cores (P. Palmeirim et al. 2013; T. G. S. Pillai et al. 2020). While fewer observations exist toward IRDCs (and specifically bones), early polarization observations toward these objects indicate that a similar behavior may be occurring in at least some regions of two high-mass filaments (T. Pillai et al. 2015; I. W. Stephens et al. 2022). However, stellar feedback from ongoing massive star formation could also lead to more complex field structures due to expanding H II bubbles (M. Tahani et al. 2023; I. Bešlić et al. 2024).

In this paper, we present the complete set of observations from the Filaments Extremely Long and Dark: A Magnetic Polarization Survey (FIELDMAPS), a legacy program of the Stratospheric Observatory for Infrared Astronomy (SOFIA) to map the polarized dust emission in 10 candidate bones of the Milky Way using the High-resolution Airborne Wide-band Camera (HAWC+) at 214 μm. The primary goal of this paper is to produce a set of systematically reduced and fully comparable polarization maps at a resolution of 18.″7 to serve as the foundation for statistically significant studies of the magnetic field properties in these unique star-forming environments. For this reason, this survey also includes updated data products for observations included in previous studies (I. W. Stephens et al. 2022; N. B. Ngoc et al. 2023). The resulting public archive of high-resolution polarimetric data toward candidate bones of the Milky Way will probe a different regime of high-mass star-forming environments compared to studies of the Central Molecular Zone (see FIREPLACE survey; N. O. Butterfield et al. 2024a, 2024b; D. Paré et al. 2024) and of nearby molecular clouds (see BISTRO survey, e.g., D. Ward-Thompson et al. 2017). These data will also increase the number of regions where the relation between filament and magnetic field orientations can be studied (e.g., K. Pattle et al. 2017; K. Monsch et al. 2018; Y. Doi et al. 2020; D. Arzoumanian et al. 2021; D. Lee et al. 2021).

The contents of this paper are divided as follows: In Section 2, we detail the acquisition and reduction of the astronomical observations used in this work. In Section 3, we present the polarization and magnetic field maps for all 10 candidate bones of this survey, we compare the magnetic field structure with Planck data, we fit the polarization efficiency for each target, and we discuss the physical significance of our results. Additional technical considerations are also addressed in the Appendices.

2. Observations

2.1. SOFIA

SOFIA was an airborne observatory jointly operated by NASA and the German Aerospace Center (DLR) from 2010 to 2022.[16] SOFIA was built from a Boeing 747-SP airframe modified to house a Nasmyth–Cassegrain telescope with an effective diameter of 2.5 m and designed to quickly swap instruments between a series of flights. The observatory flew at an altitude of 13 km, above 99% of the water vapor in the atmosphere, which made it capable of observing wavelength regimes between 5 and 600 μm that are inaccessible from the ground. SOFIA's mobility allowed it to operate from both the Northern and Southern Hemispheres, thus making it one of a few observatories capable of accessing the entire night sky.

HAWC+ was a far-infrared polarimetric camera available as a SOFIA facility instrument from 2018 to 2022 (C. D. Dowell et al. 2010; D. A. Harper et al. 2018). Its main components were three cryogenically cooled 32 by 40 detector arrays composed of transition-edge sensors and separated by a polarizing beam splitter, with two arrays in reflection and one in transmission. In polarization mode, a half-wave plate rotated to four specific angles with a DC brushless air-coil motor would be introduced into the light path before the beam

[16] https://irsa.ipac.caltech.edu/Missions/sofia.html

Table 1
Characteristics of the HAWC+ Observing Bands Used for This Work (D. A. Harper et al. 2018)

Band	λ (μm)	FWHM (arcsec)	Pol. FOV (arcmin)	Detector[a] (arcsec)	Pixel[b] (arcsec)
A	53	4.85	1.4 × 1.7	2.55	1.21
E	214	18.2	4.2 × 6.2	9.37	4.55

Notes.
[a] Detector pixel size of the instrument.
[b] Map pixel size of the resulting data products.

splitter, and only two arrays were used (one in reflection and one in transmission) to recover the Stokes *Q* and *U* parameters. This instrument was capable of observing in five bands: 53 μm (band *A*), 63 μm (band *B*), 89 μm (band *C*), 154 μm (band *D*), and 214 μm (band *E*). For each band used in this paper, Table 1 provides the full width at half-maximum (FWHM) of the telescope's beam, the instrument's instantaneous field of view (FOV) in polarization, the size of the instrument's detectors on the sky, and the final pixel size of the resulting data products.

FIELDMAPS is a SOFIA Legacy Program (08_0186, PI: I. Stephens) to map the magnetic field structure in 10 candidate bones of the Galaxy using HAWC+ observations of dust polarization at 214 μm (see also I. W. Stephens et al. 2022). The observations for program 08_0186 were acquired between 2020 September and 2022 July during SOFIA Cycles 8 and 9. This survey also uses archival data at 214 μm from SOFIA programs 05_0109 (PI: I. Stephens), 05_0206 (PI: T. Pillai), and 06_0027 (PI: I. Stephens). Program 06_0027 also included 53 μm data, which are presented in Appendix C. The observations used for this paper are all publicly available on the NASA Infrared Science Archive (IRSA). The updated data products created for this data release paper are available online on the FIELDMAPS Dataverse at doi:10.7910/DVN/NUXGJE. The target selection for the survey is explained in Section 2.1.1, the HAWC+ observing modes used in Appendix A, and the data acquisition and processing in Section 2.1.2. A detailed breakdown of observations on a source by source basis is given in Appendix B.

2.1.1. Target Selection

The 10 science targets for the FIELDMAPS survey were selected from the list of large-scale filaments collated by C. Zucker et al. (2018) as candidate bones. From this point, we will refer to these targets as bones instead of candidate bones for simplicity, but we emphasize that the properties of these objects are still actively studied and that their categorization could change in the future. The resulting sample includes bones found near both arm and interarm (spur) regions of the Galaxy. Specifically, we observed bones associated with the following six structures defined by M. J. Reid et al. (2016): the Carina near arm, Centaurus-Crux near arm, the Norma arm, the Sagittarius near and far arms, and the Scutum near arm (ScN). The ScN in particular is slightly overrepresented due to being associated with a majority of the bones identified by C. Zucker et al. (2015). The detailed properties of the bones observed for the FIELDMAPS survey are given in Table 2.

Our target list includes seven bones (Filaments 1, 2, 4, 5, 6, 8, and 10) that each fulfill at least five out of six of the criteria established by C. Zucker et al. (2015). The most relevant criteria for this study are that the long axis of these bones is parallel within 30° to the Galactic disk, and they are found to be within 20 pc from the Galactic midplane and within 10 km s^{-1} of the global longitude–latitude–velocity track of their nearest spiral arm. We also include three large-scale Herschel filaments (G24, G47, and G49) from K. Wang et al. (2015) that were part of the subset of contiguous filaments from C. Zucker et al. (2018). While these candidates failed one or more of the original bone selection criteria (C. Zucker et al. 2015), their physical properties otherwise closely resemble those of the seven other bones in this survey. For these reasons, we make no distinction between previously identified bone and large-scale Herschel filament, and we simply identify both categories as bones as in I. W. Stephens et al. (2022).

Our target selection was made from the subset compiled by C. Zucker et al. (2018) of 18 filaments showing contiguity in Herschel-derived column density maps. We used 250 μm data from the Herschel Infrared Galactic Plane Survey (Hi-GAL) to choose the bones that had the highest predicted brightness contrast between foreground and background. For 10 of the bones, most of the filamentary structure was at least 600 MJy sr^{-1} above the local background emission. At this contrast level, significant polarization could be detected by HAWC+ in the bones with minimal integration time. In comparison, the remaining eight bones would have required much longer exposures, including the prototypical bone candidate Nessie (J. M. Jackson et al. 2010; A. A. Goodman et al. 2014). Nevertheless, the 10 selected bones should be a representative sample of the known population based on their physical properties (such as mass and length; C. Zucker et al. 2018) and varying degrees of star formation activity (see Section 3.1).

Due to their position in the Galaxy, most of the targets in our sample were previously observed in the infrared by surveys of the Galactic plane (e.g., M. Perault et al. 1996; S. D. Price et al. 2001; R. A. Benjamin et al. 2003; S. J. Carey et al. 2009; S. Molinari et al. 2010). Follow-up studies using these surveys subsequently identified several of these targets as IRDCs (e.g., N. Peretto & G. A. Fuller 2009), giant molecular filaments (GMFs; S. E. Ragan et al. 2014; K. Wang et al. 2015; J. Abreu-Vicente et al. 2016; K. Wang et al. 2016), and bones (C. Zucker et al. 2015, 2018). Filament 6 in particular is one of the earliest IRDCs found in the Galactic plane (S. J. Carey et al. 1998; M. P. Egan et al. 1998, identified as G11.11–0.12), and so, it is the most extensively studied object in the FIELDMAPS sample (e.g., S. J. Carey et al. 2000; D. Johnstone et al. 2003; T. Pillai et al. 2006b, 2015; T. Henning et al. 2010; K. Wang et al. 2014; T. Pillai et al. 2015).

The distances and associated spiral arms listed in Table 2 have been modified from the original catalog published by C. Zucker et al. (2018), which used the Bayesian approach from M. J. Reid et al. (2016). These changes were made to reflect the updated Galactic structure model from the Bar and Spiral Structure Legacy (BeSSeL) Survey (M. J. Reid et al. 2019),[17] except for Filament 6 and G49 for which we use the most recent maser-derived parallax distances instead (see G011.10-00.11 in Table 1 of J. J. Li et al. 2022; and

[17] http://bessel.vlbi-astrometry.org/

Table 2
General Properties of the 10 Milky Way Bones Studied for the FIELDMAPS Survey

Name	R.A. (hh:mm:ss)	Decl. (±dd:mm:ss)	l (deg)	b (deg)	Velocity (km s^{-1})	$D_{\odot}$ (kpc)	$D_{\rm Gal}$ (kpc)	Length (pc)	Width (pc)	Mass ($10^3\,M_{\odot}$)	ϕ_F (deg)	Arm
Filament 1	18:41:31	−05:30:17	26.90	−0.31	68	4.2	4.9	20	1.5	4.0	93	ScN
Filament 2	18:38:49	−07:02:08	25.24	−0.42	57	3.8	5.1	38	1.1	10.5	74	ScN
Filament 4	18:30:23	−10:27:51	21.23	−0.15	66	4.3	4.5	19	1.8	7.1	96	Nor
Filament 5	18:25:09	−12:48:32	18.56	−0.10	46	4.0	4.7	61	1.3	41.5	82	Nor
Filament 6[a]	18:10:32	−19:21:14	11.14	−0.12	31	4.1	4.3	30	1.4	28.0	87	Nor
Filament 8	17:41:05	−31:13:12	357.54	−0.37	4	1.3	7.0	11	0.7	2.1	86	CrN
Filament 10	16:16:27	−50:52:01	332.42	−0.12	−49	2.9	5.9	50	1.2	31.2	95	CtN
G24	18:32:57	−07:48:58	23.87	+0.52	96	5.3	4.0	76	1.7	37.6	108	Nor
G47	19:16:40	+12:45:03	47.13	+0.30	58	4.2	6.2	38	1.1	11.3	70	SgN
G49	19:22:37	+14:10:10	49.06	−0.31	68	5.2	6.3	57	1.4	47.4	99	SgF

Note. The coordinates for each cloud were determined using the HAWC+ data in this work, and they are provided in both the ICRS (R.A. and decl.) and Galactic (longitude l and latitude b) reference frames for convenience. $D_{\odot}$is the estimated distance of the cloud from the Sun, using the cloud velocities from Table 1 of C. Zucker et al. (2018) and updated using the model from M. J. Reid et al. (2019), except for Filament 6 and G49 where we, respectively, use the maser-derived parallax distances from J. J. Li et al. (2022) and Y. W. Wu et al. (2014). $D_{\rm Gal}$ is the distance of the cloud from the Galactic center, assuming a Sun–Galactic center distance $R_{\odot} = 8.275$ kpc (GRAVITY Collaboration et al. 2019, 2021) and a solar height $z_{\odot} = 20.8$ pc above the Galactic disk (M. Bennett & J. Bovy 2019). The length, width, and mass of each bone are updated from Tables 2 and 3 of C. Zucker et al. (2018) using the updated distances $D_{\odot}$ from this table. The widths in particular are the median FWHMs obtained from the Herschel dust emission in each bone. The angle ϕ_F is the fitted orientation of each filament as measured east of Galactic north (see Section 3). The spiral arms associated with each bone are identified as the Carina near arm (CrN), the Centaurus-Crux near arm (CtN), the Norma arm (Nor), the Sagittarius near arm (SgN), the Sagittarius far arm (SgF), and the Scutum near arm (ScN; M. J. Reid et al. 2016; C. Zucker et al. 2018; M. J. Reid et al. 2019).

[a] Also nicknamed the "Snake" (K. Wang et al. 2014, 2015), not to be confused with the "Snake Nebula" (Barnard 72).

G049.19-00.34 in Table 3 of Y. W. Wu et al. 2014). The width, length, and mass of each bone were also scaled by the ratio of the new to old distances, and this scaling is squared for the mass. Similarly to C. Zucker et al. (2018), we use a far distance probability prior $P_{\rm far}$ of 0.01 for Filaments 1, 2, 4, 5, 6, 8, and 10 since they show unambiguous near-IR extinction features (see related figures in Section 3.1 and Appendix J), while the default value of 0.5 is used for G24, G47, and G49. For these last three sources, using $P_{\rm far}$ value of 0.01 or 0.5 does not impact the associated arms. The $P_{\rm far}$ probability is used to disentangle the near/far ambiguity when calculating kinematic distances (M. J. Reid et al. 2016). The uncertainties provided by the distance calculator vary between 6% and 16%, with a median of 9% for the sample.

Notable changes from C. Zucker et al. (2018) include that Filament 5 is slightly more likely to be associated with Norma instead of Scutum near, Filament 8 with Carina instead of Centaurus-Crux near, and G49 with the near arm instead of the far arm of Sagittarius. For Filament 6, the parallax distance of 4.1 ± 0.2 kpc from J. J. Li et al. (2022) is larger than the most likely (with a probability $P = 0.61$) kinematic distance of 2.9 ± 0.2 kpc in Scutum near obtained from the BeSSeL calculator. The parallax distance for this filament is instead in better agreement with the second solution from the calculator (with $P = 0.39$) at a kinematic distance of 3.8 ± 0.3 kpc in Norma. While J. J. Li et al. (2022) still refer to Filament 6 as being part of the Scutum arm, we report Norma as its associated arm in Table 2 to remain consistent with the process used for the other targets in the sample. In contrast, for G49, the parallax distance of 5.2 ± 0.3 kpc from Y. W. Wu et al. (2014) is within the uncertainties of the kinematic distance of 5.5 ± 0.5 kpc, and so, there is no change to the associated nearest arm.

The identification of the closest spiral arm for each bone in Table 2 relies specifically on the model from M. J. Reid et al. (2019), and the results could change when using a different model (e.g., J. P. Vallée 2008). Additionally, new 3D extinction maps of the solar neighborhood with Gaia have shown the existence of significant dust structures between spiral arms (C. Zucker et al. 2023). We reiterate that the targets in our sample are candidate bones, and that their classification could change in the future. However, even if they existed in interarm regions instead, their known properties and relative positions within the disk would still make them uniquely suited to study the role of magnetic fields in dense star-forming filaments of the Galactic plane.

2.1.2. Data Acquisition

The characteristics of the two HAWC+ observing modes, chop-nod and scan imaging, are detailed in Appendix A. In summary, the chop-nod observing mode used the secondary mirror of the telescope to alternate between the target and two sky positions to improve the background subtraction, while the scan mode instead moved the primary mirror in a Lissajous pattern to maximize the integration time on the target (D. A. Harper et al. 2018). In each case, when performing polarization observations, the half-wave plate was rotated to four position angles (5.°0, 50.°0, 22.°5, and 72.°5) in order to recover the linear Stokes parameters (I, Q, and U; see Section 3.2).

The observations for the FIELDMAPS legacy program (08_0186) were originally designed to use the chop-nod polarimetry mode of HAWC+ at 214 μm (band E), similarly to those from previous programs also included in this survey (05_0109, 05_0206, and 06_0027), due to the scan mode not being fully commissioned for the Cycle 8 SOFIA Call for Proposals. The "off" positions required for the initially planned chop-nod observing strategy were determined using data from the Herschel Hi-GAL survey, but finding symmetrical "off" positions without bright astronomical sources proved challenging due to the proximity of the science targets to the Galactic disk. In contrast, as discussed in Appendix A, the scan mode did not require choosing distinct "off" positions

for background subtraction, and it was a more efficient observing mode than chop-nod.

With the advent of shared-risk when observing for the scan polarimetry mode of HAWC+ in Cycle 8, all the proposed observations were redesigned from chop-nod to scan with the help of the HAWC+ Instrument Science team before the program was scheduled to be observed. Additional modifications were made during Cycle 9 (i.e., after 2021 July 1) to add overlapping scans to the remaining sources in order to limit potential edge effects and obtain a more even coverage of the filaments. Two bones in our sample were observed using chop-nod, Filament 5, and Filament 6 (the "Snake"), but only Filament 6 was observed exclusively in this mode as part of SOFIA programs 05_0109 and 06_0027. Filament 5 is the sole target in our sample with both scan and chop-nod observations, as a single field was observed in chop-nod mode for programs 05_0206 at 214 μm and 06_0027 at 53 μm (see Appendix C).

The detailed descriptions of all observations included in the FIELDMAPS survey are given in Appendix B. For each bone, we list the observing modes used, the SOFIA flights during which data were obtained, the Level 0 files (raw instrumental data) that had to be discarded before data reduction, if any, as well as the reasons why, and the astronomical observation requests (AORs) used by the HAWC+ instrument software for each planned telescope pointing. These AORs contain most of the information required to write the headers of the Flexible Image Transport System (FITS) files for the level 2, 3, and 4 data products created by the reduction pipeline (see Appendix B).

The typical observing parameters of the Lissajous scans for SOFIA program 08_0186 were horizontal x and vertical y amplitudes of 120″, respectively, noted as cross-elevation and elevation in the AOR files and the FITS headers. Since these amplitudes already provided a mostly symmetrical coverage, we kept the default range of scan angles from $-30°$ to $+30°$. Although it had no significant impact on our observing strategy, it is worthwhile to note that HAWC+ Lissajous scan angles used an azimuth-elevation reference frame instead of an equatorial one before Cycle 9. The scan duration for each pointing was set to 60 s. We aimed for an equal number of repeats for each pointing to provide even coverage of each bone, although in some cases the exact number may have varied slightly depending on the available time during each flight. In practice, each pointing would be repeated at least twice before proceeding to the next, so each filament would be covered sequentially from one end to the other over the course of one or multiple flights. For Filament 6, which was observed exclusively in chop-nod mode, AORs for program 05_0206 and 06_0027 used nod times of 40 and 50 s, respectively, and both programs used chop amplitudes of 250″. Finally, we also include chop-nod observations of Filament 5 in both band A and band E, which we compare to the scan mode observations in Appendix C.

2.1.3. Data Processing

We used the SOFIA data reduction pipeline (SOFIA Redux version 1.3.0; M. Clarke & R. V. Vliet 2023) to systematically process level 0 HAWC+ polarization observations downloaded from IRSA into level 4 data products for the FIELDMAPS survey. The HAWC+ scan mode reduction package used by SOFIA Redux is a Python adaptation of the Java-based CRUSH data reduction software (A. Kovács 2008a), and most of the reduction parameters are shared between the two packages.

For each bone, all the available level 0 scan data were loaded into SOFIA Redux using the default reduction parameters provided except for the additional parameters *fixjumps = True* and *rounds = 30*. The *fixjumps* parameter identifies and compensates for potentially anomalous flux jumps on individual detectors. The *rounds* parameter controls the number of iterations for the map-making algorithm. A higher number of iterations can improve the recovery of extended emission, but at the cost of increased noise and longer computation times (A. Kovács 2008a). We found that doubling the number of rounds from the default 15 was sufficient to systematically recover the polarized emission across the length of most bones in our sample, but we also note that previous studies of the Central Molecular Zone have reliably recovered extended emission with SOFIA Redux by using a number of rounds as high as 85 (N. O. Butterfield et al. 2024a). In contrast, we only used the default reduction parameters provided in SOFIA Redux for chop-nod observations of Filaments 5 and 6.

When a large set of level 0 scan files is provided to the HAWC+ reduction pipeline, the software processes consecutive files (sometimes up to 24, with four per repeat) sharing the same AOR number, obtained from the same flight into a single level 2 data product. These level 2 data products are then calibrated from instrumental counts to jansky per pixel and merged into level 3 data products for each flight. Appendix B lists all the files that had to be discarded for each flight, and Appendix D describes how the level 2 files for Filament 4 were corrected for positional errors. SOFIA Redux uses calibration standards based on observations of Uranus, Neptune, and other solar system objects obtained at the start of each HAWC+ flight series during the lifetime of the instrument. The flux calibration accuracy is expected to be within 10%, which is sufficient for this work as we are mainly interested in the polarization fraction P and angle θ, relative quantities derived from the Stokes I, Q, and U parameters (see Section 3.2). Finally, the merged level 3 data products from each flight are combined by the pipeline into a single "multimission" level 4 data product.

The pixel scale of the final data product is 4.″55, and the effective resolution is 18.″7 instead of the diffraction-limited 18.″2 due to the smoothing step during the map-making process. We verified the accuracy of this effective beam by rereducing calibration observations of Neptune obtained at 214 μm during Flights 607, 787, and 884 and fitting a 2D Gaussian in the CARTA data analysis tool. We also found that observations of Neptune in chop-nod and scan polarization modes during Flights 607 and 884 show similar beam profiles. However, we could not find chop-nod observations of Neptune in the total intensity mode, and so, we cannot directly measure the effect of the smoothing steps between the chop-nod and scan mode reduction pipelines in SOFIA Redux at this time. Nevertheless, for this work, we will refer to 18.″7 as the beam size for HAWC+, although it may be a small overestimation for chop-nod observations.

The resulting level 4 data products for each bone are FITS files with multiple extensions containing the Stokes I, Q, and U parameters and their uncertainties, as well as derived quantities such as the polarized intensity I_P, the polarization fraction P, and the rotation angle θ_P. The calculation of these polarization

properties is detailed in Section 3.2. The complete structure and contents of the level 4 HAWC+ data products are described by M. S. Gordon et al. (2018) and M. Clarke et al. (2022).

The final step of the data reduction process was to transform the coordinate system of the level 4 data products from the International Celestial Reference System (ICRS) to the Galactic Coordinate System (GCS). The full description of the transformation from ICRS to GCS is provided in Appendix E. The FIELDMAPS data products are provided in both coordinate systems through the survey data repository on the Harvard Dataverse. Since studies of objects within the Galaxy often use the GCS system, this paper will use the GCS data exclusively to present the bones.

2.2. Herschel

The Herschel Space Observatory was a far-infrared mission operated by the European Space Agency (ESA), with support from NASA, from 2009 May to 2013 June (G. L. Pilbratt et al. 2010).[18] The telescope for Herschel had an effective diameter of 3.28 m, and the spacecraft carried two imaging cameras: the Photodetecting Array Camera and Spectrometer and the Spectral and Photometric Imaging Receiver (SPIRE). For this work, we use observations from Hi-GAL (S. Molinari et al. 2010) combining five of the continuum bands covered by these two instruments: 70, 160, 250, 350, and 500 μm.

The data we used were produced from the raw Hi-GAL observations following the recipe described by A. E. Guzmán et al. (2015) to obtain continuum maps at a resolution of $36\farcs4$ (G. Aniano et al. 2011). The resulting data products differ from those of the Hi-GAL survey by using a background subtraction technique that more effectively separates Galactic cirrus or other emission from the molecular clouds themselves; it also corrects for the unknown zero levels of the Herschel photometric scales (A. E. Guzmán et al. 2015). This process emphasizes the accurate measurement of cold, dark filamentary structures like the bones of the FIELDMAPS survey. The continuum data from the Hi-GAL program were obtained in the parallel, fast-scanning mode and reduced with version 9.2.0 of the Herschel pipeline. The method convolves the five-band image set to the lowest available resolution (i.e., the 500 μm SPIRE beam) using the convolution kernels of G. Aniano et al. (2011). The background is subtracted from the images for each field and for each observing band under the assumption that it constitutes a smooth additive component arising from diffuse emission in front and/or behind the filament.

The background model has two constraints: its value has to be less than the emission at each pixel of the image, within a 2σ margin, and it cannot vary by more than than 10% over a scale of $2\farcm5$. The iterative algorithm first creates a smoothed image by setting to zero the spatial frequencies corresponding to flux variations on angular scales smaller than $2\farcm5$. Whenever a pixel in the smoothed image is larger than the corresponding pixel in the original image by more than 2σ, it is replaced by the value in the original image. The result of the first iteration then replaces the starting image, and the algorithm continues to iterate this process until the difference between two consecutive iterations is below 5% in all pixels.

An example of the differences between each step of this iterative process across the Galactic disk is illustrated in Figure 1 of A. E. Guzmán et al. (2015). We find that the dust emission maps produced in this way are better at removing foreground and background emission than using the Herschel pipeline alone, thus enabling a more accurate determination of the dust column densities in each source. Indeed, when fitting the spectral energy distribution (SED) using these new maps, we typically find average dust temperatures T_d in our filaments that are a few degrees cooler than previous estimates (see Figure 5 in A. E. Guzmán et al. 2015). As emphasized by C. Zucker et al. (2018), this background subtraction method will also affect the measurement of the filaments' density profiles.

For this work, we use the Herschel data described in this section to obtain maps of the molecular hydrogen gas column density $N_{\rm H_2}$ and dust temperature T_d for each bone. The parameters used for the SED fit are a gas-to-dust ratio $R_{g/d}$ of 100, a mean molecular weight μ of 2.8, and a spectral index of the emissivity β of 1.75. Additionally, in Appendix F, we use these fits to calculate the expected spectral flux densities at 214 μm for each bone and compare them to HAWC+ measurements in order to investigate potentially missing large-scale emission in the FIELDMAPS data.

2.3. Planck

The Planck Space Observatory was the companion far-infrared mission to Herschel, also operated by ESA with support from NASA from 2009 May to 2013 October (Planck Collaboration et al. 2011).[19] Equipped with a 1.9 m by 1.6 m elliptical reflector, Planck's primary goal was to map the cosmic microwave background (CMB) with continuum and polarization observations using its two onboard instruments: the Low Frequency Instrument (30–70 GHz) and the High Frequency Instrument (HFI; 100–857 GHz). A by-product of the Planck mission was an all-sky map of polarized dust emission across the Galaxy. In this paper, we use Public Release 3 polarization maps obtained by the HFI at 353 GHz (850 μm) with an effective resolution of $5'$ (Planck Collaboration et al. 2020a, 2020b). For each bone, we downloaded 2° by 2° maps of the Stokes I, $Q_{\rm cmb}$, and $U_{\rm cmb}$ parameters from the IRSA legacy archive. Each map was calibrated from units of the cosmic background temperature $K_{\rm cmb}$ to megajansky per steradian using the conversion factors from Table 6 of Planck Collaboration et al. (2014). We also converted the Stokes $Q_{\rm cmb}$ and $U_{\rm cmb}$ maps in the COSMO/HEALPix convention (K. M. Górski et al. 2005; Planck Collaboration et al. 2015a) to Stokes $Q_{\rm gcs}$ and $U_{\rm gcs}$ using the International Astronomical Union (IAU) convention (e.g., J. P. Hamaker & J. D. Bregman 1996) rotated to be in the GCS coordinate system (see Appendix E).

2.4. Spitzer

The Spitzer space telescope was an infrared mission operated by NASA from 2003 August to 2020 January.[20] Spitzer was equipped with an 85 cm mirror, and the platform carried two photometric imagers: the Infrared Array Camera (G. G. Fazio et al. 2004) covering four bands at 3.6, 4.5, 5.8, and 8.0 μm, and the Multiband Imaging

[18] https://irsa.ipac.caltech.edu/Missions/herschel.html

[19] https://irsa.ipac.caltech.edu/Missions/planck.html

[20] https://irsa.ipac.caltech.edu/Missions/spitzer.html

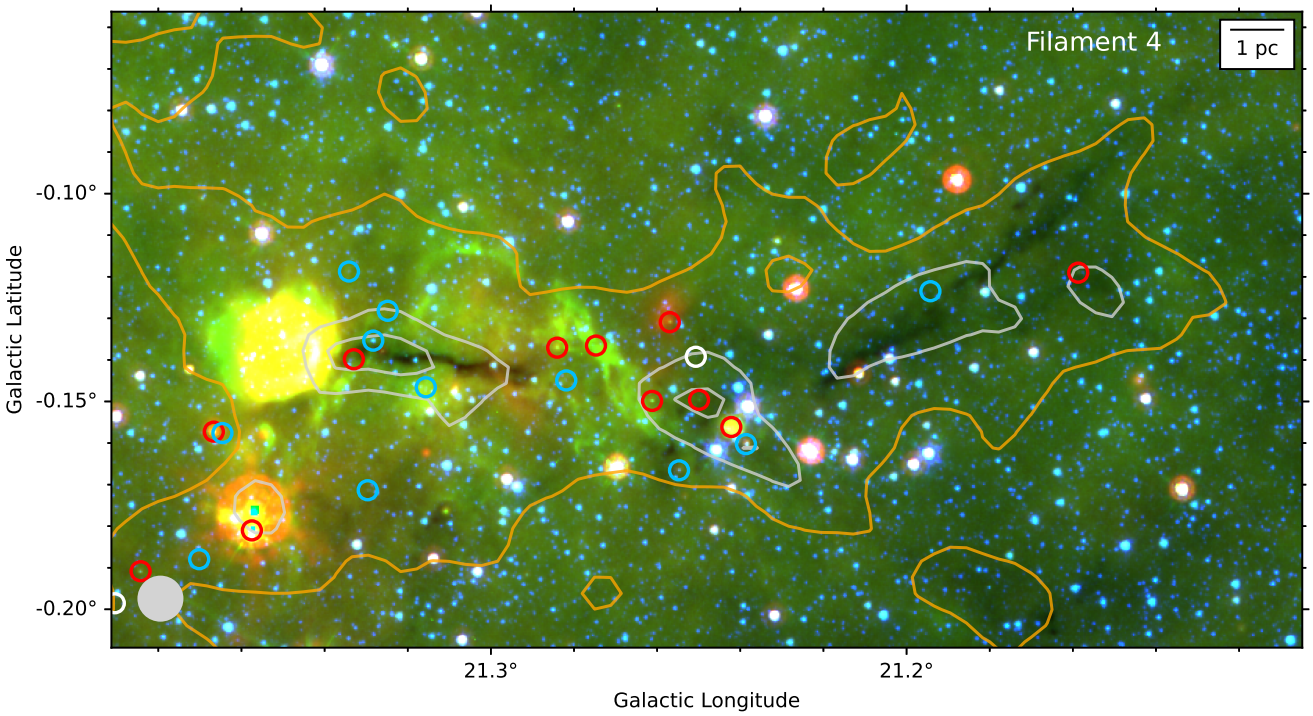

Figure 1. Spitzer red (24 μm), green (8.0 μm), and blue (3.6 μm) composite image for Filament 4. The color levels were chosen to highlight the infrared-dark features of the bone. Class I and flat-spectrum (red), Class II (blue), and Class III (white) YSOs from the literature are identified with circles. The three contours trace Herschel-derived N_{H_2} column densities of 0.5, 1.0, and 1.5 $\times$ 10^{22} cm^{-2}, with the lowest level identified in orange for clarity. The Herschel beam at 500 μm is given by the gray circle at the bottom left. A reference length of 1 pc is provided at the top right, assuming a distance $D_{\odot}$ of 4.5 kpc to the cloud (see Table 2).

Photometer for Spitzer (G. H. Rieke et al. 2004) at 24, 70, and 160 μm. For this work, we use archival data of the Galactic plane from the Galactic Legacy Infrared Midplane Survey Extraordinaire (GLIMPSE; R. A. Benjamin et al. 2003) and from the MISPGAL survey (S. J. Carey et al. 2009) survey to create infrared images of each bone.

3. Results

3.1. Star Formation Activity

The list of young stellar objects (YSOs) used for this work was obtained from the catalog produced by M. Zhang et al. (2019). In their catalog, the YSOs were identified and classified via multiband photometric catalogs spanning the near- to far-infrared. The UKIRT Infrared Deep Sky Survey (A. Lawrence et al. 2007), the Vía Láctea survey (D. Minniti et al. 2010), and the Two Micron All Sky Survey point-source catalog (M. F. Skrutskie et al. 2006) provided the near-IR identifications. The mid-infrared archival data were obtained from the Spitzer galactic plane surveys, GLIMPSE (R. A. Benjamin et al. 2003) and MISPGAL (S. J. Carey et al. 2009), in addition to ALLWISE (E. L. Wright et al. 2010) and the Red Midcourse Space Experiment Source survey (S. L. Lumsden et al. 2013). The far-infrared data used to identify protostellar objects were also obtained from the Hi-GAL survey (S. Molinari et al. 2010). In this paper, we only include Class I, flat-spectrum, Class II, and Class III YSOs compiled by M. Zhang et al. (2019). We also performed a literature search for massive YSOs, as well as masers,[21] for each bone (e.g., B. E. Svoboda et al. 2016; H. Beuther et al. 2019).

To illustrate the typical star formation activity in the bones, Figure 1 shows the positions of Class I, II, III, and flat-spectrum YSOs for Filament 4 on a composite red (24 μm), green (8.0 μm), and blue (3.6 μm) image from the GLIMPSE and MIPSGAL surveys with Spitzer. The color levels were chosen to highlight the infrared-dark features of the filament, although the H II region to the east is saturated as a result. Figure 1 also includes contours of Herschel-derived N_{H_2} column density from 0.5 to 1.5 $\times$ 10^{22} cm^{-2}. Filament 4 was chosen as an example because it shows clearly identifiable features associated with IRDCs and signs of ongoing star formation. Appendix J provides similar images for each bone. While we found no confirmed maser for the region displayed by Figure 31 in Appendix J, several have been detected across the FIELDMAPS targets, and their positions are plotted in Figures 28–32 in Appendix J.

3.2. Derived Polarization Properties

Polarization vectors (also called "pseudovectors" or "half-vectors" due to their 180° ambiguity) are defined using the Stokes parameters, with Stokes I being the total intensity of the incoming light, and Stokes Q and U being the linear components describing the fraction of polarized light P and the rotation angle θ. Following the IAU convention, the polarization angle θ is measured on the celestial sphere from north to east. The relations between these quantities are given by $Q = P\,I\cos(2\theta)$ and $U = P\,I\sin(2\theta)$.

The full description of how each parameter is calculated during the data reduction process of HAWC+ observations is given by M. S. Gordon et al. (2018) and M. Clarke et al. (2022), although we note here that they use a slightly different notation for the polarization fraction. For the FIELDMAPS survey, we provide data products in both the ICRS and GCS

[21] https://maserdb.net/

reference frames. The process of calculating the updated Stokes parameters $Q_{\rm gcs}$ and $U_{\rm gcs}$ from Stokes $Q_{\rm icrs}$ and $U_{\rm icrs}$ is detailed in Appendix E. From this point forward, we will refer to Stokes $Q_{\rm gcs}$ and $U_{\rm gcs}$ as Stokes Q and U for simplicity, and because the results in this paper were obtained using the data products rotated in the GCS frame.

We detail below the equations used to derive the polarization properties and their uncertainties from the measured Stokes I, Q, and U parameters, assuming the cross-terms of the error covariance matrix are small (M. S. Gordon et al. 2018). First, the polarized intensity I_p is simply written as

$$I_p = \sqrt{Q^2 + U^2}, \tag{1}$$

with the uncertainty δ_{I_p}:

$$\delta_{I_p} = \sqrt{\frac{(Q\ \delta_Q)^2 + (U\ \delta_U)^2}{Q^2 + U^2}}, \tag{2}$$

where δ_Q and δ_U are the uncertainties for Stokes Q and U, respectively. Although the noise for Q and U can be assumed to be normally distributed, the quadratic form of the polarized intensity I_p means that it instead follows a Rice distribution with a positive bias for low signal-to-noise measurements (K. Serkowski 1958; J. F. C. Wardle & P. P. Kronberg 1974; K. Pattle et al. 2019). This bias needs to be removed to obtain the debiased polarized intensity I'_p:

$$I'_p = \sqrt{I_p^2 - \delta_{I_p}^2}. \tag{3}$$

Following this relation, the difference between the biased I_p and debiased I'_p intensities will be less than 6% for a signal-to-noise ratio of 3 and above. The HAWC+ data reduction pipeline uses a variation of this method to debias P directly instead of I_p (see Equation (3) from M. S. Gordon et al. 2018), but we show in Appendix G that both methods are equivalent for the signal-to-noise thresholds used in this work. Finally, Equation (3) gives one of the most common approaches to debiasing polarization data, but we note that the accuracy of this process and the use of alternative methods have been studied extensively in the past (e.g., J. Naghizadeh-Khouei & D. Clarke 1993; L. Montier et al. 2015; M. Vidal et al. 2016; K. Pattle et al. 2019).

From there, we define the debiased polarization fraction P as

$$P = 100\%\ \frac{I'_p}{I} = 100\%\ \frac{\sqrt{Q^2 + U^2 - \delta_{I_P}^2}}{I}, \tag{4}$$

which we will express as a percentage here. From this point, we will refer to the debiased polarization fraction P simply as the polarization fraction, as we never use the biased quantity for this work. The uncertainty δ_P on the polarization fraction is given by

$$\delta_P = 100\%\ \frac{I_p}{I}\sqrt{\left(\frac{\delta_{I_p}}{I_p}\right)^2 + \left(\frac{\delta_I}{I}\right)^2}, \tag{5}$$

where δ_I is the uncertainty for the Stokes I total intensity.

The polarization angle θ in degrees is given by

$$\theta = \frac{180^\circ}{2\,\pi}\arctan\left(\frac{U}{Q}\right), \tag{6}$$

with a valid range of -90° to 90°, which fully covers the range of possible angles for the polarization vectors described here. Specifically, we use of the two-argument arctan 2 function in Python to solve the quadrant degeneracy of arctan when dividing the Stokes U and Q parameters. The uncertainty δ_θ is then expressed as

$$\delta_\theta = \frac{180^\circ}{2\,\pi}\ \frac{\sqrt{(U\ \delta_Q)^2 + (Q\ \delta_U)^2}}{Q^2 + U^2}. \tag{7}$$

Finally, as discussed in Section 1, we obtain the plane-of-sky orientation θ_B of the magnetic field by rotating the polarization angle θ by 90°.

Table 3
Number of Detected Polarization Vectors and Noise Characteristics for Each Bone

Name	$N_{\rm pol}$	$N_{\rm beam}$	M_{δ_I}	M_{δ_Q} (mJy arcsec^{-2})	M_{δ_U}
Filament 1	5574	420	0.059	0.076	0.076
Filament 2	14,459	1089	0.077	0.105	0.104
Filament 4	10,876	819	0.060	0.078	0.078
Filament 5	6266	472	0.092	0.123	0.121
Filament 6	6522	491	0.081	0.118	0.119
Filament 8	3367	253	0.166	0.211	0.211
Filament 10	8881	669	0.241	0.299	0.295
G24	26,222	1976	0.088	0.111	0.111
G47	9553	720	0.044	0.055	0.056
G49	12,824	966	0.215	0.243	0.240

3.3. Polarization and Magnetic Field Maps

For the analysis covered in this paper, we used the data products described in Section 2.1.3 to create catalogs of polarization vectors at 214 μm that fulfill the following selection criteria: signal-to-noise thresholds of $I/\delta_I > 10$ and $P/\delta_P > 3$, and a maximum polarization fraction $P < 30\%$. The upper limit in polarization fraction and the larger signal-to-noise cutoff for Stokes I were chosen to remove any vector with an anomalously high polarization fraction, as Planck found a maximum polarization fraction $p_{\rm max}$ of $22.5^{+3.5}_{-1.5}\%$ in the interstellar medium (Planck Collaboration et al. 2020c). Large values of the polarization fraction P could be a result of filtering large-scale emission in the Stokes I map (see Appendix F).

For each bone, Table 3 gives the total number of vectors $N_{\rm pol}$ in those catalogs, as well as the lower limit $N_{\rm beam}$ of independent beam positions with a detection of polarization (i.e., one measurement per beam area). The number $N_{\rm beam}$ is approximated by multiplying the number of detected polarization vectors $N_{\rm pol}$ by the ratio of the area of a 4.″55 square pixel and the area of a circle with the same diameter as the 18.″7 effective beam FWHM at 214 μm (resulting in a factor ∼0.075). We also include in Table 3 the median uncertainties M_{δ_I}, M_{δ_Q}, and M_{δ_U} of the Stokes I, Q, and U parameters, respectively, for the catalog of polarization vectors for each bone.

Figures 2–11 present the polarization observations for the FIELDMAPS survey. Each figure is divided into two panels, with the top panel being the map of inferred magnetic field

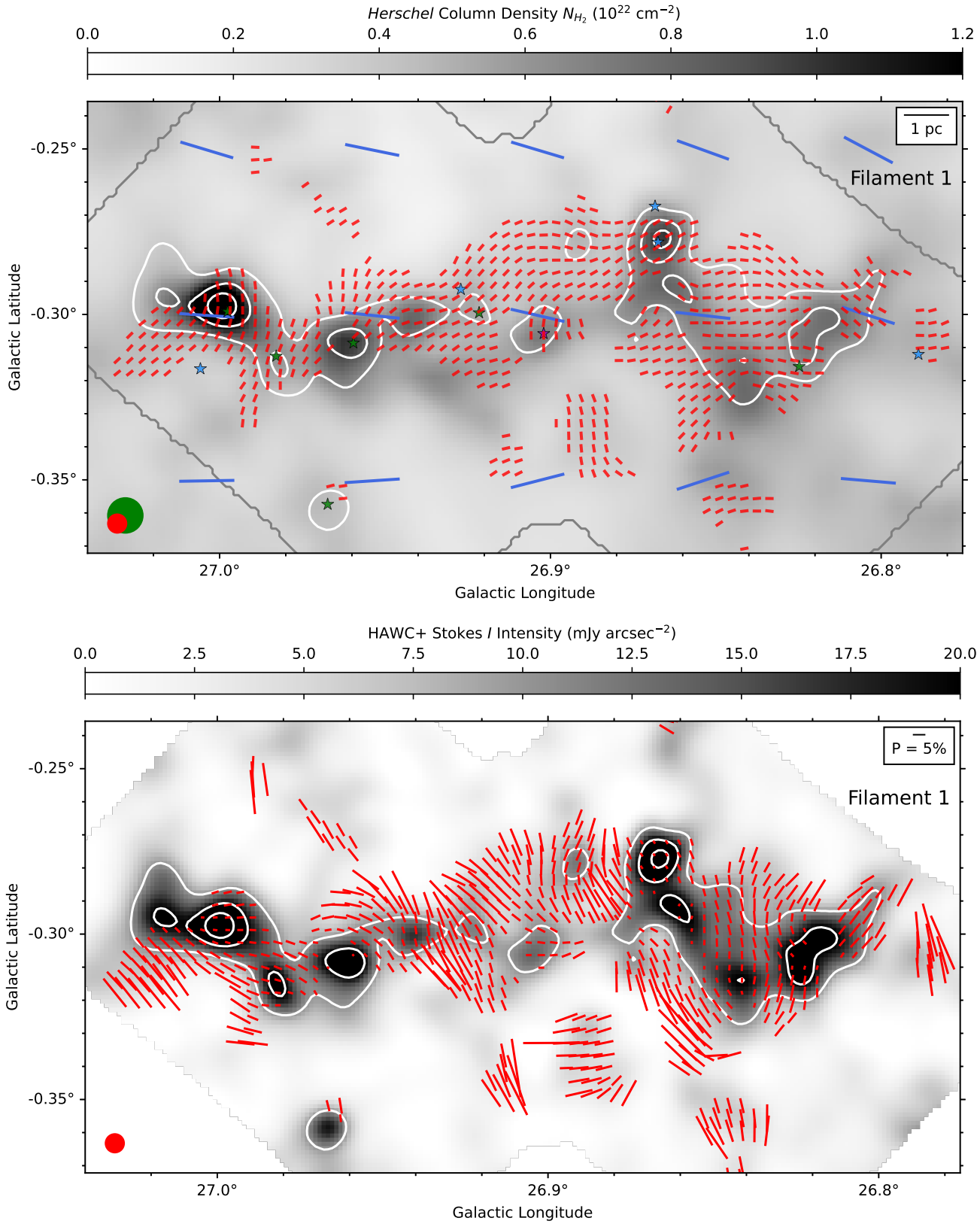

Figure 2. Filament 1. Top: the inferred magnetic field structure (HAWC+ 214 μm, red; Planck 850 μm, blue) plotted on the Herschel-derived $N_{\rm H_2}$ column density map (gray). The magnetic field angle θ_B is obtained from rotating the polarization angle θ by 90°. Class I (green), flat-spectrum (violet), and Class II (blue) YSOs are identified with star symbols. The gray contour denotes the area observed by HAWC+. The circles denote the beam sizes of HAWC+ (red) and Herschel (green). Bottom: the polarization measurements (red) plotted on the HAWC+ Stokes I total intensity map (gray) at 214 μm. The vector length shows the polarization fraction P. For each panel, only every third vector is plotted for both SOFIA and Planck data, and the white contours trace the Stokes I total intensity from 10 mJy arcsec^{-2} and increasing by steps of 10 mJy arcsec^{-2}. See Section 3.3 for details.

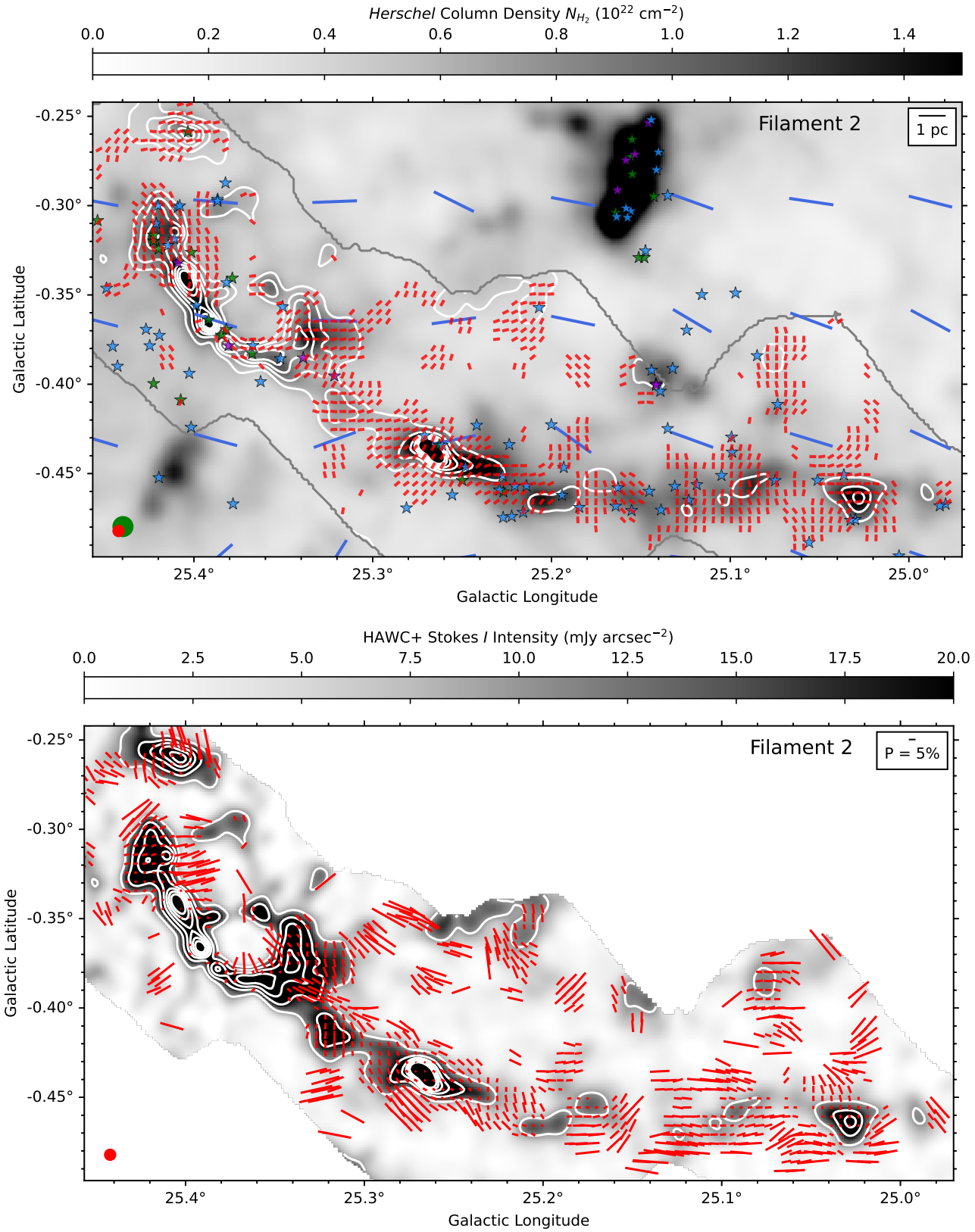

Figure 3. Filament 2. Same as Figure 2, with every fourth vector plotted for both SOFIA and Planck data. See Section 3.3 for details.

vectors and the bottom panel being the map of measured polarization vectors, as described below.

Magnetic field maps. The top panels of Figures 2–11 show the plane-of-sky magnetic field structure inferred from both HAWC+ 214 μm (red vectors) and Planck 850 μm (blue vectors) polarization observations. These magnetic field vectors, with their orientation θ_B rotated by 90° from the derived polarization angle θ, are plotted over the molecular

Table 4
Circular Mean and Standard Deviation of Polarization Angles in the Four Brightest Regions of G49

Region	l (deg)	b (deg)	$\overline{\theta}$ (deg)	σ_θ (deg)
G49a	48.913	−0.285	−46.5	7.3
G49b	48.987	−0.298	−89.2	28.1
G49c	49.211	−0.342	28.0	21.9
G49d	49.266	−0.339	40.1	8.9

hydrogen column density N_{H_2} (gray scale) obtained from Herschel continuum data (see Section 2.2). To facilitate the visualization of the magnetic field structure, the vector lengths are fixed to a single arbitrary length for each map, and we vary the sampling of the plotted HAWC+ and Planck vectors depending on the bone (see individual captions). Sampling every fourth polarization vector is equivalent to plotting 1.0 vector per beam element for HAWC+ and 1.25 vector per beam element for Planck. The white contours trace the HAWC + 214 μm Stokes I total intensity for the following levels starting at 10 mJy arcsec^{-2} and increasing by steps of 10 mJy arcsec^{-2}, unless stated otherwise in the caption. The beam sizes of HAWC+ (18.″7; red circle) and Herschel (36.″4; green circle) are also given, and, while we do not show it on the plot since it is too large, we note here that the Planck beam is (5′). A scale bar is provided to show a reference length of 1 pc for each bone, using the distances listed in Table 2. Also shown are the Class I (green stars), flat-spectrum (violet stars), and Class II (light blue stars) YSOs identified for this work (see Section 3.1).

Polarization maps. The bottom panels of Figures 2–11 show the HAWC+ 214 μm polarization vectors (red) plotted over the Stokes I map (gray scale). The orientation of each vector is given by the polarization angle θ derived from the Stokes Q and U parameters. The length of each vector is its associated polarization fraction P, and a reference length of $P = 5\%$ is provided. To facilitate the comparison between the top and bottom panels of each figure, the white contours in the bottom panel also trace the HAWC+ 214 μm Stokes I total intensity for the following levels starting at 10 mJy arcsec^{-2} and increasing by steps of 10 mJy arcsec^{-2}, unless stated otherwise in the caption. The HAWC+ beam size (18.″7) is indicated with a red circle.

For Filament 5, the results of the chop-nod observations are plotted in Figure 18 of Appendix C.

3.4. Distributions of Polarization Angles

We compiled the polarization angles θ from the vector catalogs of each bone as histograms in Figures 12 and 13. The total number of elements in each histogram is given by the $N_{\rm pol}$ parameter in Table 3. Each histogram covers a 180° range centered on the circular mean $\overline{\theta}$ of the distribution. This variable range takes into account the 180° ambiguity for half-vectors, which means that the lower and upper limits of the x-axis for each histogram are equal. We use directional statistics to find an accurate mean value of the polarization angle distribution (e.g., Y. Doi et al. 2020). Specifically, the circular mean and standard deviation for each bone were calculated using the library of statistical functions from the SciPy Python package with boundaries of −90° and 90°. Using the circular mean value calculated for each bone, we find an average polarization angle of $67.^\circ9 \pm 30.^\circ9$ for our sample, which is equivalent to $-22.^\circ1 \pm 30.^\circ9$ for the magnetic field orientation relative to Galactic north.

Table 5
Magnetic Field and Filament Orientations for Each Bone Relative to Galactic North

Name	$\overline{\theta}_B$ (deg)	$\overline{\theta}_{PB}$ (deg)	ϕ_F (deg)	$\delta\overline{\theta}_B$ (deg)	$\delta\overline{\theta}_{PB}$ (deg)
Filament 1	119.3	84.1	93	−26.3	8.9
Filament 2	153.1	80.6	74	−79.1	−6.6
Filament 4	134.8	93.6	96	−38.8	2.4
Filament 5	6.1	91.1	82	75.9	−9.1
Filament 6	5.3	77.9	87	81.7	9.1
Filament 8	150.3	84.5	86	−64.3	1.5
Filament 10	115.8	96.4	95	−20.8	−1.4
G24	31.1	88.9	108	75.9	18.1
G47	155.2	116.0	70	−85.2	−46.0.
G49	176.5	54.7	99	−77.5	44.3

We note that the histogram of a random distribution of angles from −90° to 90° will tend toward a continuous uniform distribution, which has a standard deviation of $180^\circ/\sqrt{12} \approx 52.^\circ0$. The circular standard deviation in the limit of a circular uniform distribution is not as well defined, but we nonetheless caution against overinterpreting values σ_θ greater than 50° as a general rule.

Figure 14 presents the stacked histogram combining all the distributions shown in Figures 12 and 13, each identified with a different color. The circular mean and standard deviation of the resulting stacked distribution of polarization angles are $65.^\circ6 \pm 56.^\circ6$, which are equivalent to $-24.^\circ4 \pm 56.^\circ6$ for the corresponding mean magnetic field angle. Even with a greater weight from the bones with the highest number of detected polarization vectors, the resulting circular mean is within a few degrees from the average of the circular means of each individual bone. Despite the larger circular standard deviation of $56.^\circ6$, the stacked distribution is nevertheless clearly peaked around the mean. As a whole, the mean magnetic field measured with HAWC+ in the bones is therefore closer to perpendicular to the Galactic disk than parallel to it.

We used Planck polarization data to estimate the average Galactic field orientation in the plane of the sky toward the location of each bone. First, we regridded their respective HAWC+ Stokes I maps to share the same footprint and pixel scale as the Planck maps described in Section 2.3. We then used the regridded HAWC+ data to mask pixels in the Planck maps where the HAWC+ Stokes I intensity was less than zero or undefined. The polarization angles from the remaining pixels in the Planck maps were then used to calculate the circular mean $\overline{\theta}_P$ for each bone, which we identify in Figures 12 and 13 as the green dotted lines. Using the circular mean values of each bone as before, we find an average polarization angle of $-3.^\circ1 \pm 14.^\circ6$ for our sample, which is equivalent to $86.^\circ9 \pm 14.^\circ6$ for the magnetic field orientation relative to Galactic north. These results are in agreement with the expectation of a large-scale magnetic field mostly parallel to the Galactic plane.

Figures 12 and 13 also illustrate the complexity of the plane-of-sky magnetic field structure observed with HAWC+ in each bone. Even Filaments 1, 10, and G47, which are the closest to exhibiting a single-peak distribution, have circular standard

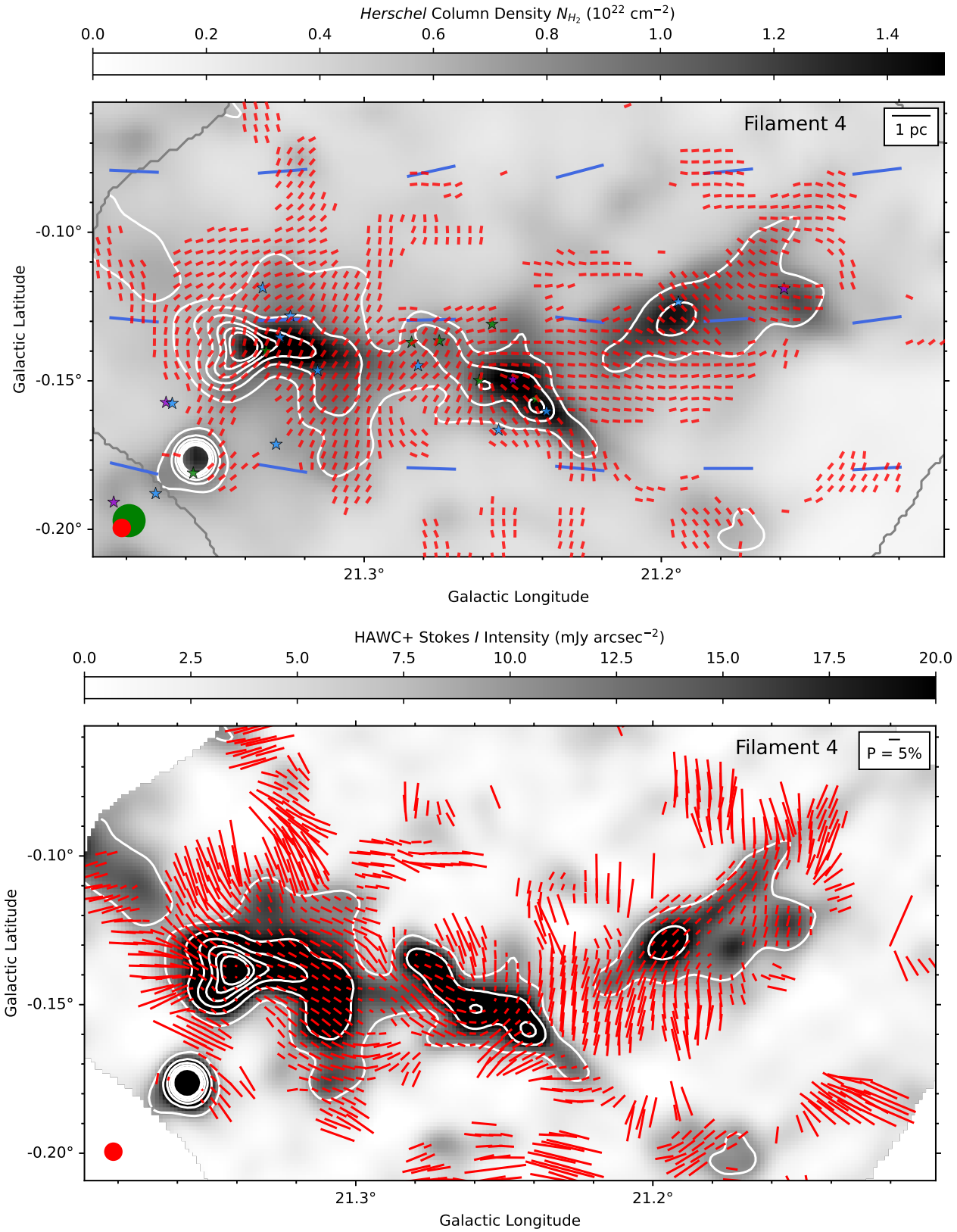

Figure 4. Filament 4. Same as Figure 2, with every third vector plotted for both SOFIA and Planck data. See Section 3.3 for details. This figure displays the same area as Figure 1.

deviations of polarization angles greater than 30°. The large standard deviations are even more evident in the other bones of the sample, and especially for G24 and G49, which each have a circular standard deviation greater than 60° and a nearly flat histogram. It would be tempting then to conclude that the magnetic fields in these objects must be weak and disorganized. A closer look at Figures 2–11, however, shows fields that appear locally well ordered, but often with smoothly

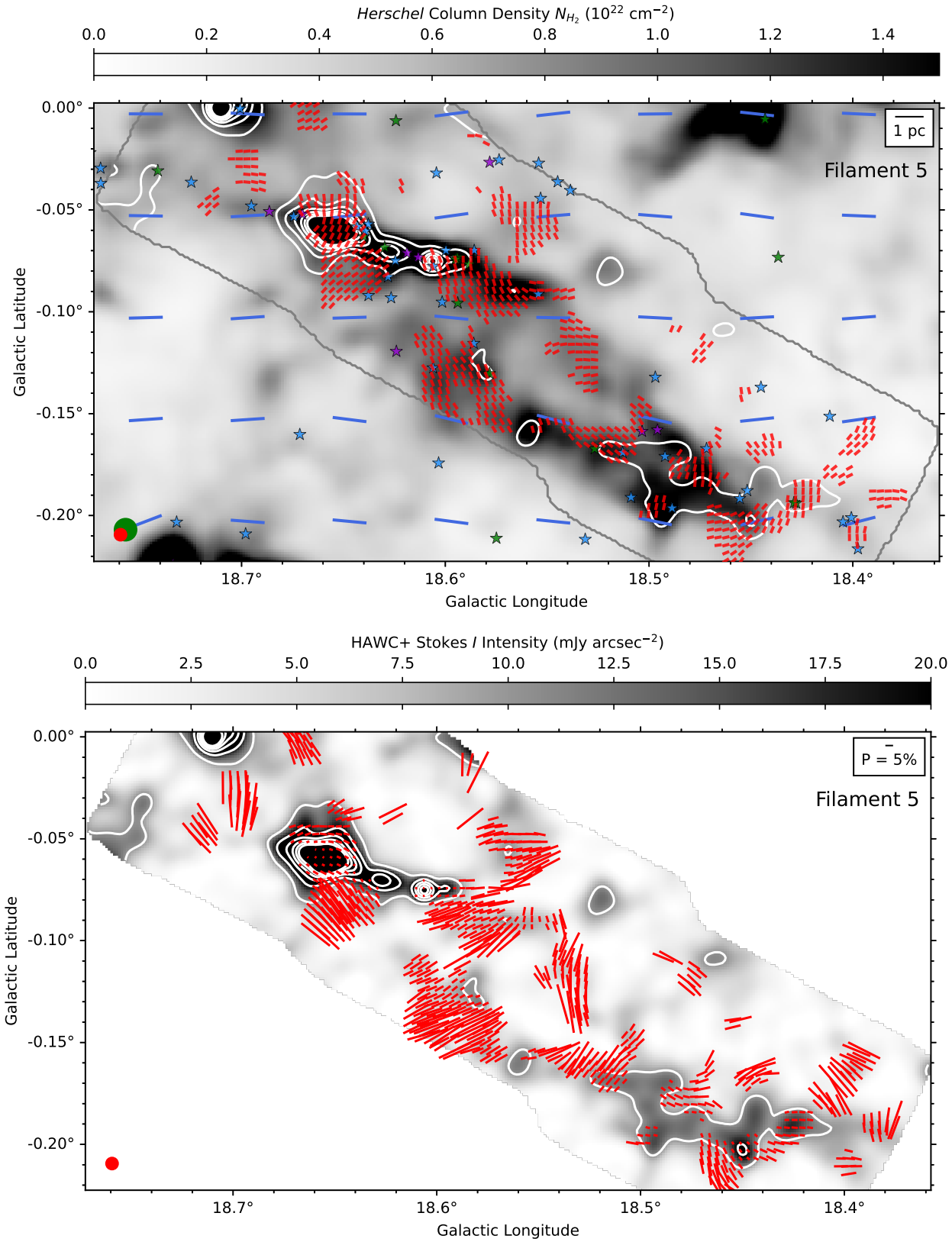

Figure 5. Filament 5. Same as Figure 2, with every third vector plotted for both SOFIA and Planck data. See Section 3.3 for details.

varying orientations between different regions along the length of the bone. Such a behavior has been predicted by Galactic-scale magnetohydrodynamic simulations of giant molecular cloud evolution (B. Zhao et al. 2024). Additionally, combining multiple components of a magnetic field that is well ordered locally into a single histogram can lead to distributions with extended wings, which is a well-documented phenomenon in optical polarimetry (e.g., A. A. Goodman et al. 1990).

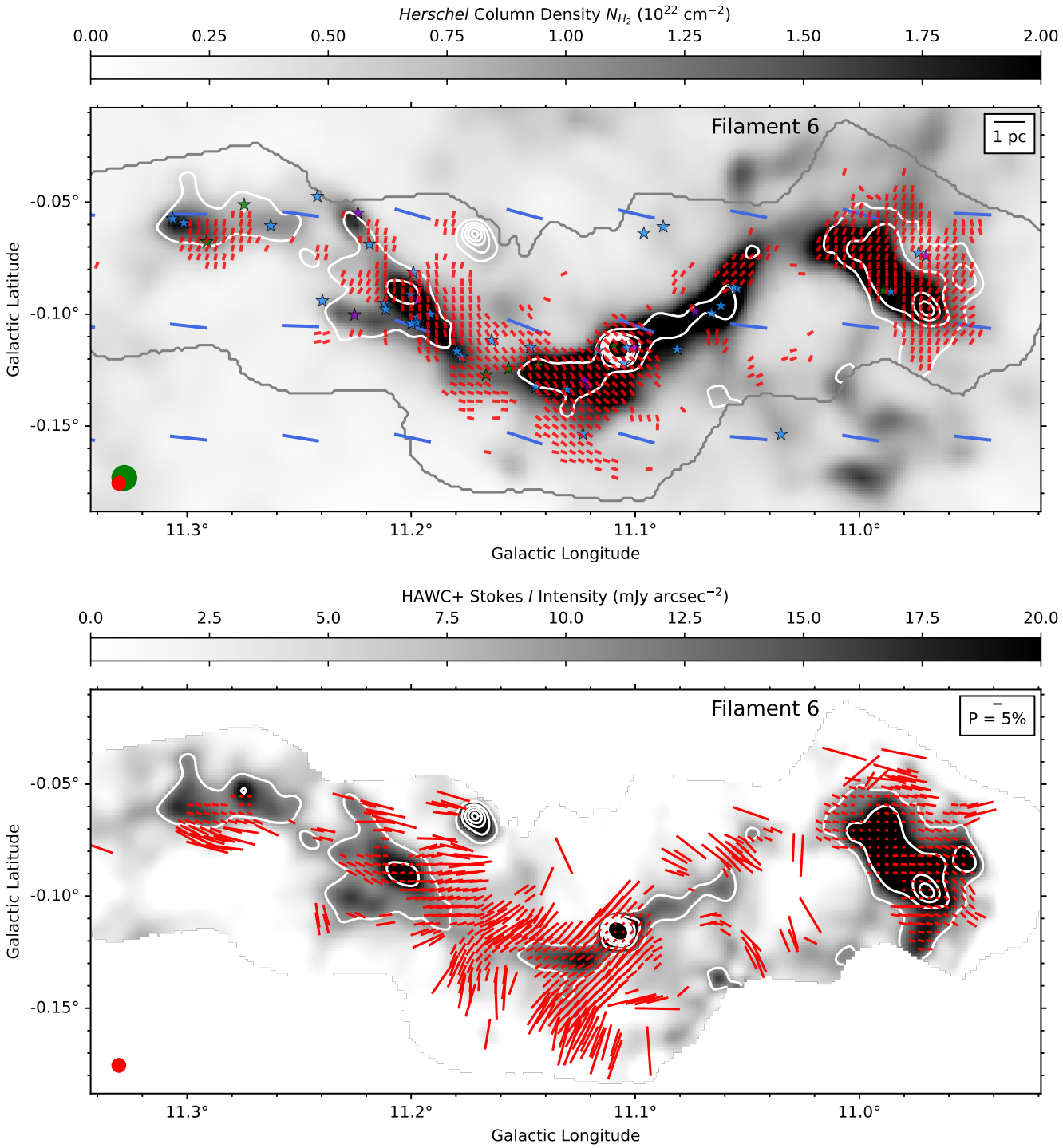

Figure 6. Filament 6 (i.e., the "Snake"). Same as Figure 2, with every third vector plotted for both SOFIA and Planck data. See Section 3.3 for details.

We further investigated the local structure of the magnetic field in G49 by studying the distribution of polarization angles around the four brightest peaks of the bone. We selected G49 because it is the bone with the largest measured circular standard deviation at $65.^{\circ}1$, as seen in Figure 13. Table 4 provides the circular mean $\overline{\theta}$ and standard deviation σ_θ for each region, which were calculated from the polarization vectors contained within a $91''$ by $91''$ box (about 5 times the beam size of HAWC+) centered on the listed coordinates. These regions are identified with green squares in the top panel of Figure 11. The corresponding histograms are shown in Figure 23 of Appendix H. There are two main takeaways from Table 4: the circular mean $\overline{\theta}$ differs significantly for each region, and their respective standard deviation σ_θ is much smaller than the global standard deviation for the bone. The wide distribution of polarization angles for G49 can therefore be explained by the combination of multiple well-ordered magnetic field components across the length of the filament.

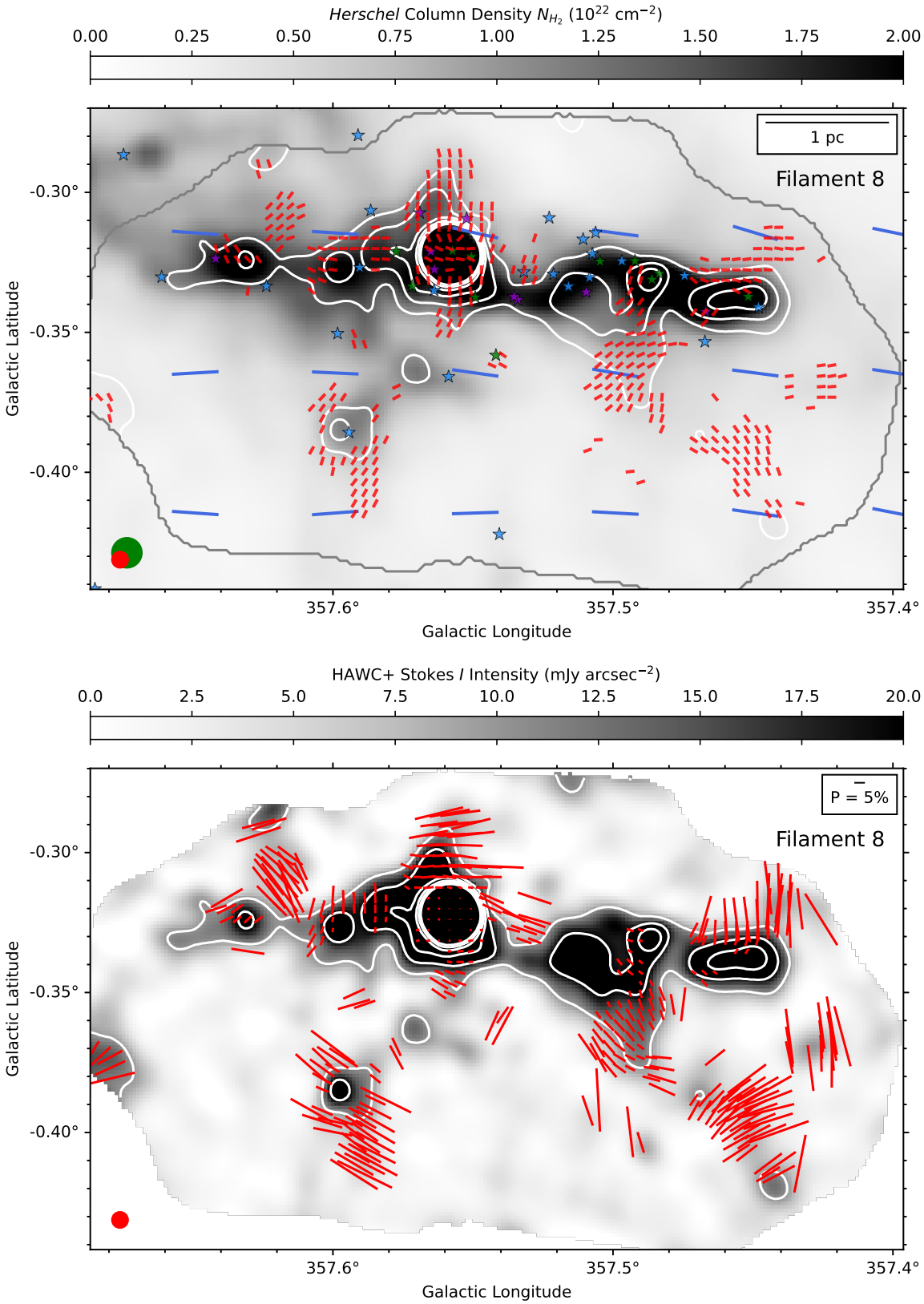

Figure 7. Filament 8. Same as Figure 2, with every third vector plotted for both SOFIA and Planck data. See Section 3.3 for details.

3.4.1. Magnetic Field and Filament Orientations

One of the distinctive features of bones is the orientation of their filamentary structure parallel to the Galactic disk (C. Zucker et al. 2015). As noted in Section 1, the Planck team found that the magnetic field in the disk is also oriented mostly parallel to the Galactic plane (Planck Collaboration et al. 2015a). In contrast, magnetic field lines are generally expected to become orthogonal to the length of dense filaments (e.g., K. Tomisaka 2014; Planck Collaboration et al. 2016;

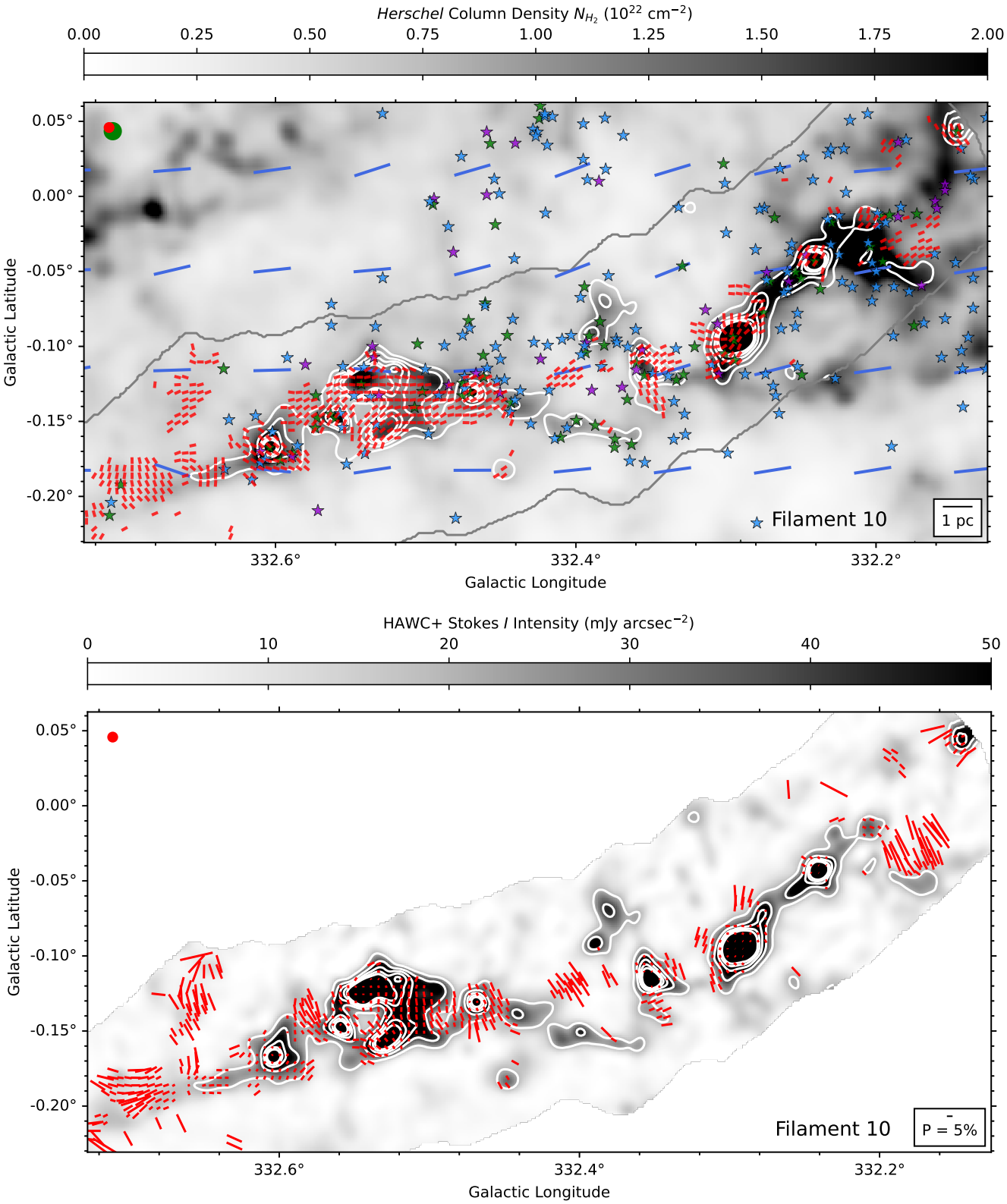

Figure 8. Filament 10. Same as Figure 2, with every fourth vector plotted for both SOFIA and Planck data. The white contours in the bottom panel also trace the HAWC+ 214 μm Stokes *I* total intensity for the following levels starting at 20 mJy arcsec^{-2} and increasing by steps of 20 mJy arcsec^{-2}. See Section 3.3 for details.

K. Pattle & L. Fissel 2019). The FIELDMAPS data provide us with an opportunity to investigate the orientation of magnetic fields in bones relative to their length, and therefore quantify that these fields are closer on average to the Galactic field orientation or to the expected structure in dense filaments.

The spine of the filaments was determined by C. Zucker et al. (2018) using the FILFINDER package (E. W. Koch & E. W. Rosolowsky 2015), which produces masks where the "skeleton" of a filament is traced by a pixel-wide line. We used a least-squares linear regression to find the mean

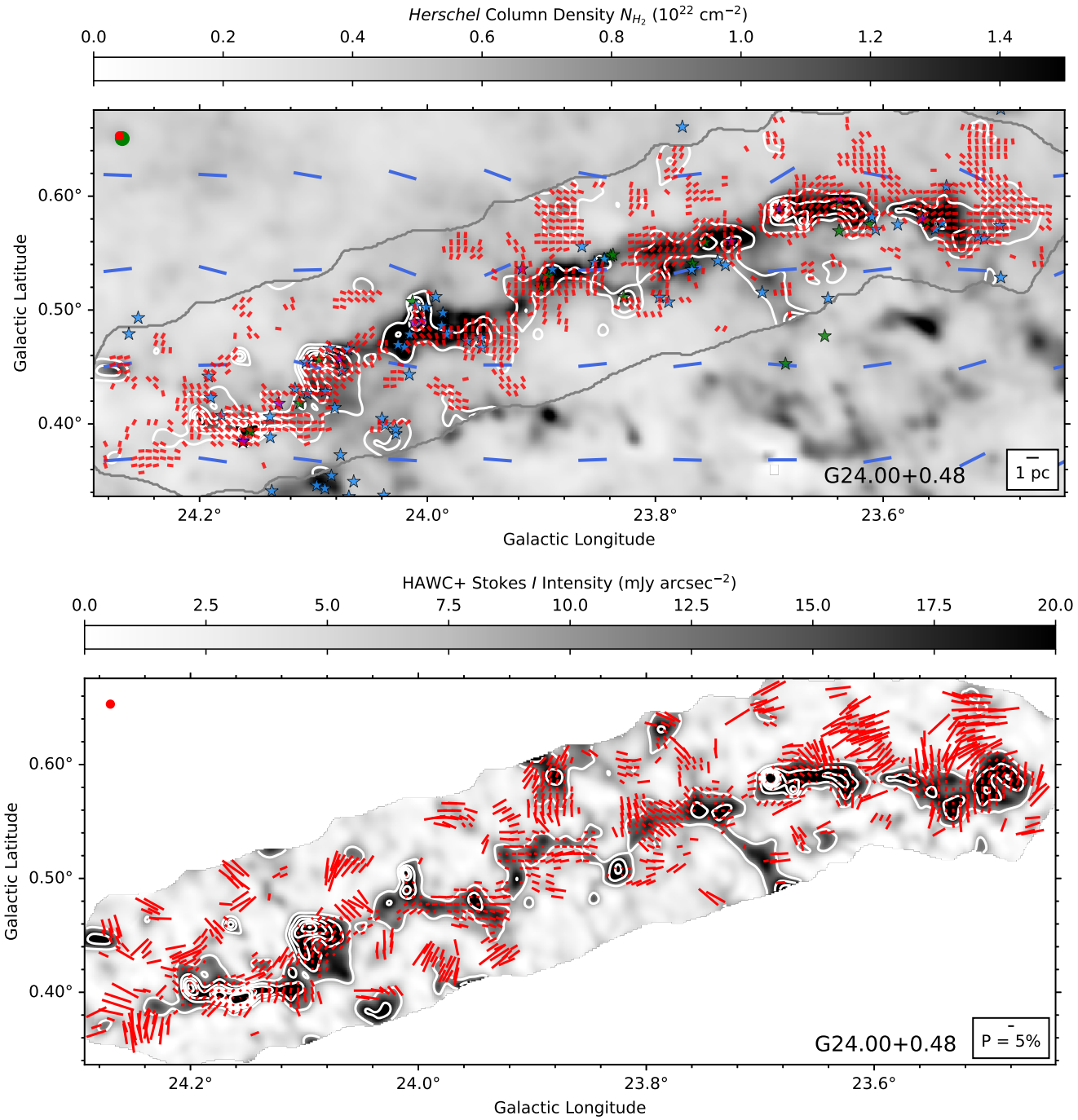

Figure 9. G24. Same as Figure 2, with every fifth vector plotted for both SOFIA and Planck data. See Section 3.3 for details.

orientations ϕ_F relative to Galactic north (e.g., $\phi_F = 90°$ is parallel to the Galactic plane). We show the result of these fits for Filament 10 in Figure 26 of Appendix I, and the corresponding figures for each other bone are available on the FIELDMAPS Dataverse. These orientations ϕ_F are identified in Figures 12 and 13 as the blue dotted lines, as well as in Table 5 using a range of 0°–180° for clarity. We measure the spine position angle of each bone relative to the Galactic plane as $\delta\phi = \phi_F - 90°$, and we find a circular mean and standard deviation of $\langle\delta\phi\rangle = 1\overset{\circ}{.}0 \pm 10\overset{\circ}{.}9$ for the entire sample. While Filament 2, G24, and G47 are slightly more inclined than the rest, all 10 bones fulfill the requirement listed in Section 2.1.1 to be parallel within 30° from the Galactic plane.

We then measured the angle differences $\delta\overline{\theta}_B = \overline{\theta}_B - \phi_F$ and $\delta\overline{\theta}_{PB} = \overline{\theta}_{PB} - \phi_F$ of the average magnetic field directions $\overline{\theta}_B$ from HAWC+ and $\overline{\theta}_{PB}$ from Planck observations, respectively, relative to the orientation ϕ_F of each bone. The values for $\overline{\theta}_B$ and $\overline{\theta}_{PB}$, given in Table 5 using the same 0°–180° range as in Figure 15, were obtained by adding 90° to the circular means $\overline{\theta}$ and $\overline{\theta}_P$ calculated previously. The differences $\delta\overline{\theta}_B$ and $\delta\overline{\theta}_{PB}$ are also given in Table 5 using a range of −90° to 90°. For the HAWC+ data, we find a mean difference $\langle\delta\overline{\theta}_B\rangle$ of $-73\overset{\circ}{.}7 \pm 31\overset{\circ}{.}6$ between the filament axis and the plane-of-sky magnetic field. When using the Planck data, we instead find a difference $\langle\delta\overline{\theta}_{PB}\rangle$ of $2\overset{\circ}{.}8 \pm 21\overset{\circ}{.}0$.

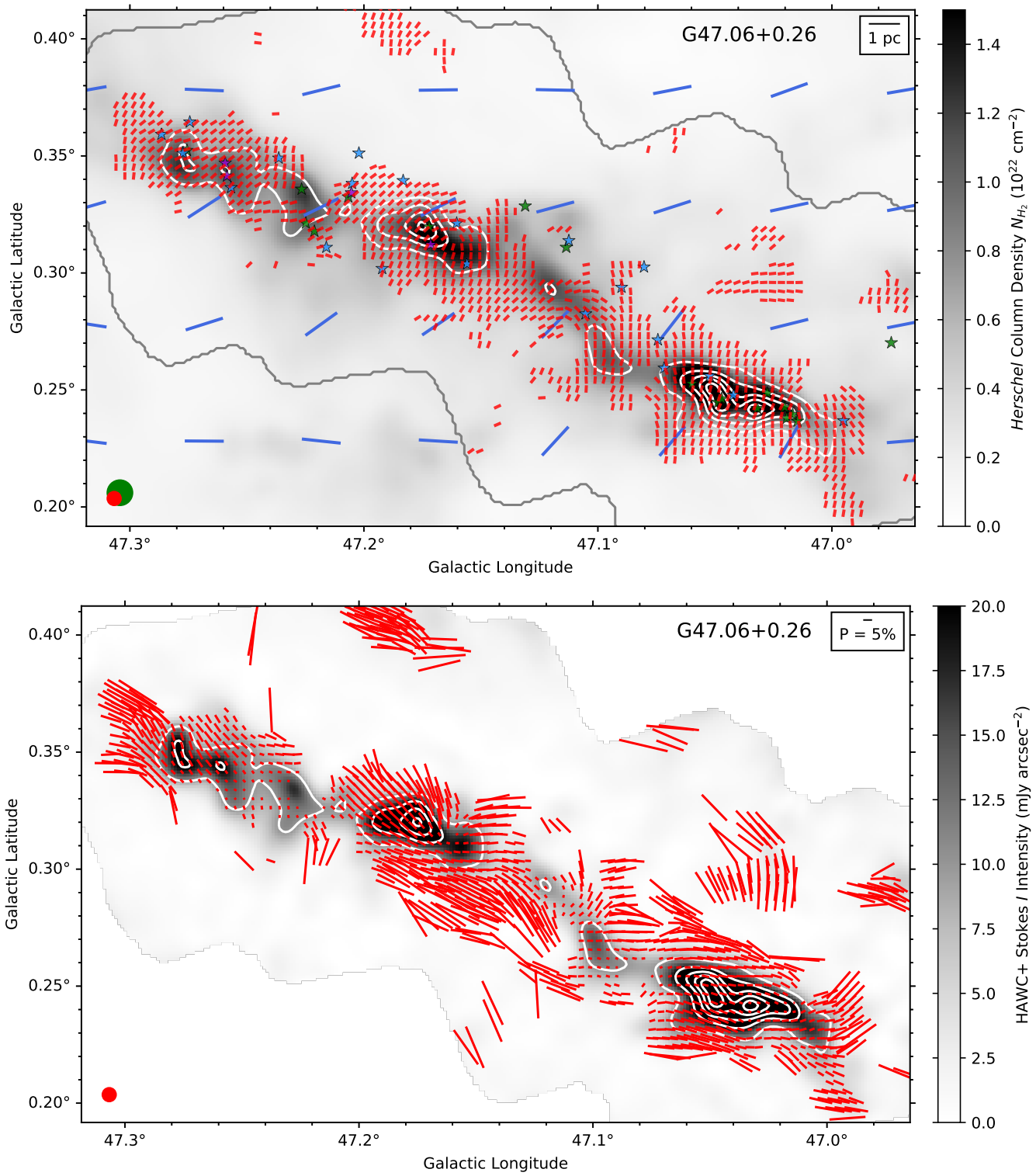

Figure 10. G47. Same as Figure 2, with every third vector plotted for both SOFIA and Planck data. See Section 3.3 for details.

On average, the Planck data trace a magnetic field parallel to the length of the bones, which themselves are nearly parallel to the Galactic plane. This would be in agreement with a scenario where the magnetic field at large scales closely follows the spiral arms of the Galaxy (e.g., A. S. Borlaff et al. 2021). However, we must note that the magnetic field seen by Planck may not be fully representative of the Galactic field at the location of each bone, as the data may be skewed by the integration of multiple components along the line of sight (Planck Collaboration et al. 2015b) and by instrumental effects (Planck Collaboration et al. 2015a). In contrast, the HAWC+ data, which probe smaller scales than Planck and are closer, on average, to being perpendicular to the length of bones, support the expectation that the link between Galactic and local magnetic fields breaks down in dense star-forming regions (e.g., I. W. Stephens et al. 2011). Finally, while these statistics

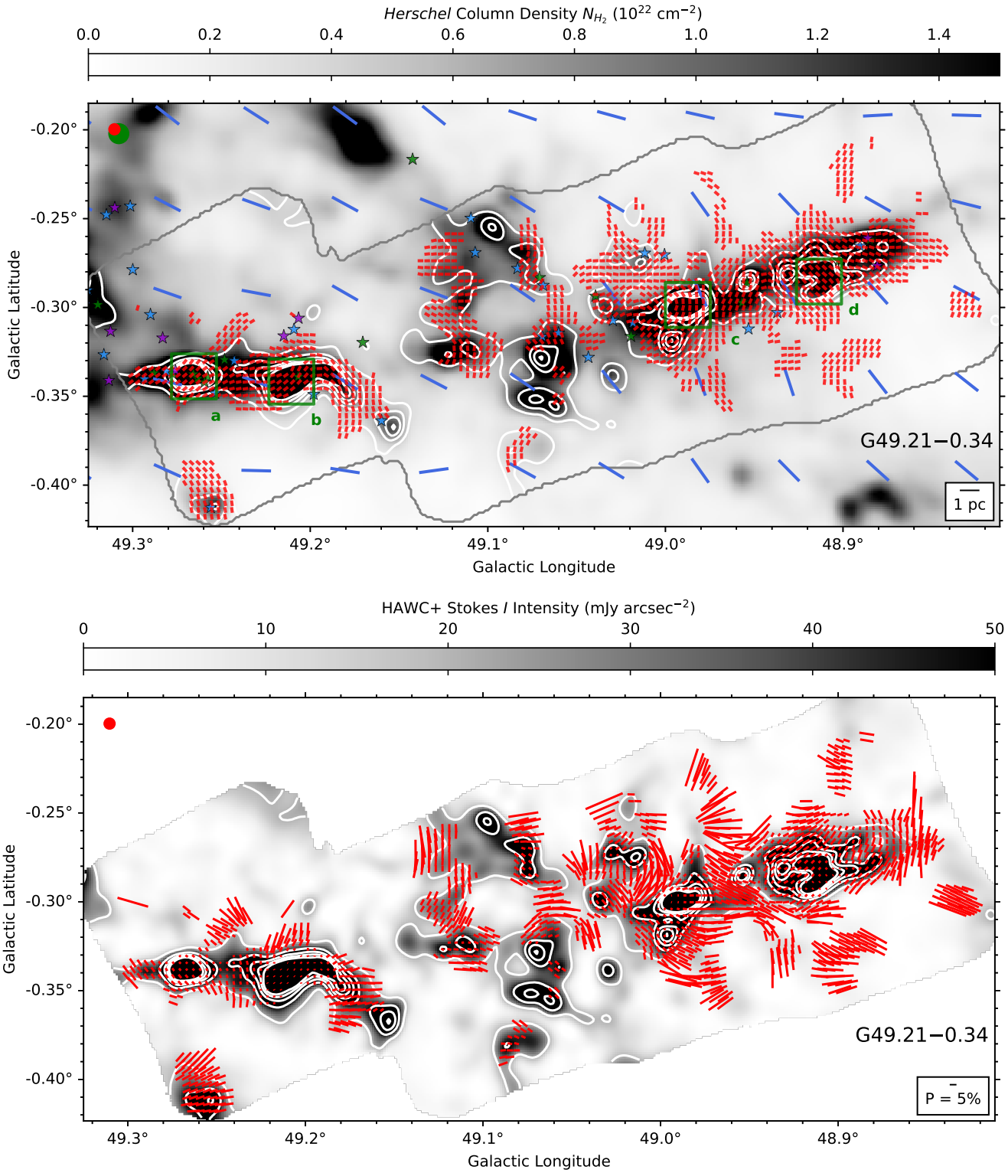

Figure 11. G49. Same as Figure 2, with every third vector plotted for both SOFIA and Planck data. The white contours trace the HAWC+ 214 μm Stokes I total intensity for the following levels starting at 20 mJy arcsec^{-2} and increasing by steps of 30 mJy arcsec^{-2}. See Section 3.3 for details. Additionally, the green squares in the top panel identify the four regions listed in Table 4.

are helpful to glean general trends from the bones as a single population of objects, they may obscure the existence of complex field structures due to feedback from the star formation occurring within them (see Section 3.1).

To investigate these potential trends more closely, Figure 15 shows the comparison between the HAWC+ and the Planck mean magnetic field directions $\overline{\theta}_B$ and $\overline{\theta}_{PB}$ for individual bones. The error bars trace their respective circular standard deviations. The large error bars for the HAWC+ data illustrate the wide spread of polarization angles measured in each filament, as shown in Figures 12 and 13. The two dashed lines indicate the 90° orientation of the Milky Way disk relative to

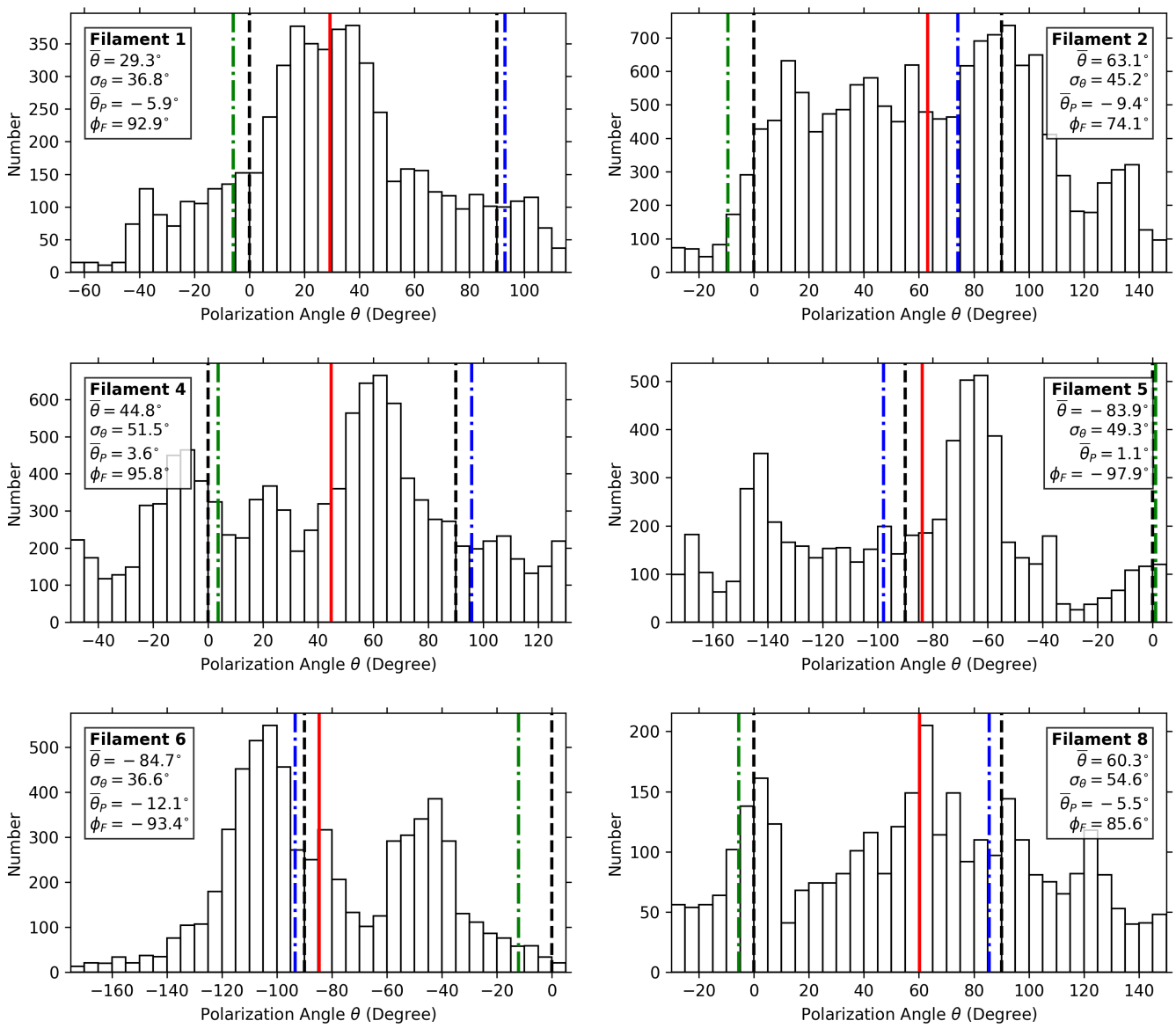

Figure 12. Histograms of polarization angles θ. Continued in Figure 13. All angles are provided relative to Galactic north. The bin size of the histograms is 5°. For each target in this study, the full red line is the circular mean $\overline{\theta}$ of the distribution, the green dashed–dotted line is the circular mean of the Planck polarization angles $\overline{\theta}_P$, and the blue dashed–dotted line is the fitted orientation ϕ_F of the filament (see Section 3.4). Each histogram is centered on the bin containing the circular mean $\overline{\theta}$. Black dashed lines indicate angles of −90°, 0°, and 90° for clarity. The measured circular standard deviation σ_θ for each cloud is also given within the insets. The inferred magnetic field orientation θ_B is obtained from rotating the polarization angle θ by 90°.

Galactic north for both data sets. The diagonals show the difference $\Delta\theta = |\overline{\theta}_B - \overline{\theta}_{PB}|$ for values of 0° (full line), 45° (dotted line), and 90° (dashed–dotted line).

An important trend from Figure 15 is that the Planck magnetic field orientations follow the Galactic disk for most bones, while the HAWC+ data cover a wider range of values. Of note, the two bones farthest from the Galactic center, G47 and G49 (see Table 2), are also the ones where the Planck-derived large-scale magnetic field deviates the most from being parallel to the disk. As shown in Figures 10 and 11, there is a clear shift in the Planck-derived field lines toward the spine of these two bones from a field that is mostly parallel to the Galactic plane elsewhere, including for every other bone in the sample. This could be explained by the relative position on the sky of G47 and G49 approximately 50° from the Galactic center, which means that there is likely to be less dust to integrate along the line of sight in the Planck data compared to the locations of other bones. Indeed, shifts similar to those seen in G47 and G49 in the large-scale field orientation measured by Planck have been observed toward dense filaments in less-crowded lines of sight (e.g., Planck Collaboration et al. 2016; Y. Doi et al. 2020).

3.4.2. Relation to Magnetic Field Strengths

The classical approach to measuring the plane-of-sky amplitude $B_{\rm pos}$ of the magnetic field with polarimetry is through the Davis–Chandrasekhar–Fermi (DCF) method (L. Davis 1951; S. Chandrasekhar & E. Fermi 1953). A common form of the DCF equation is given by R. M. Crutcher

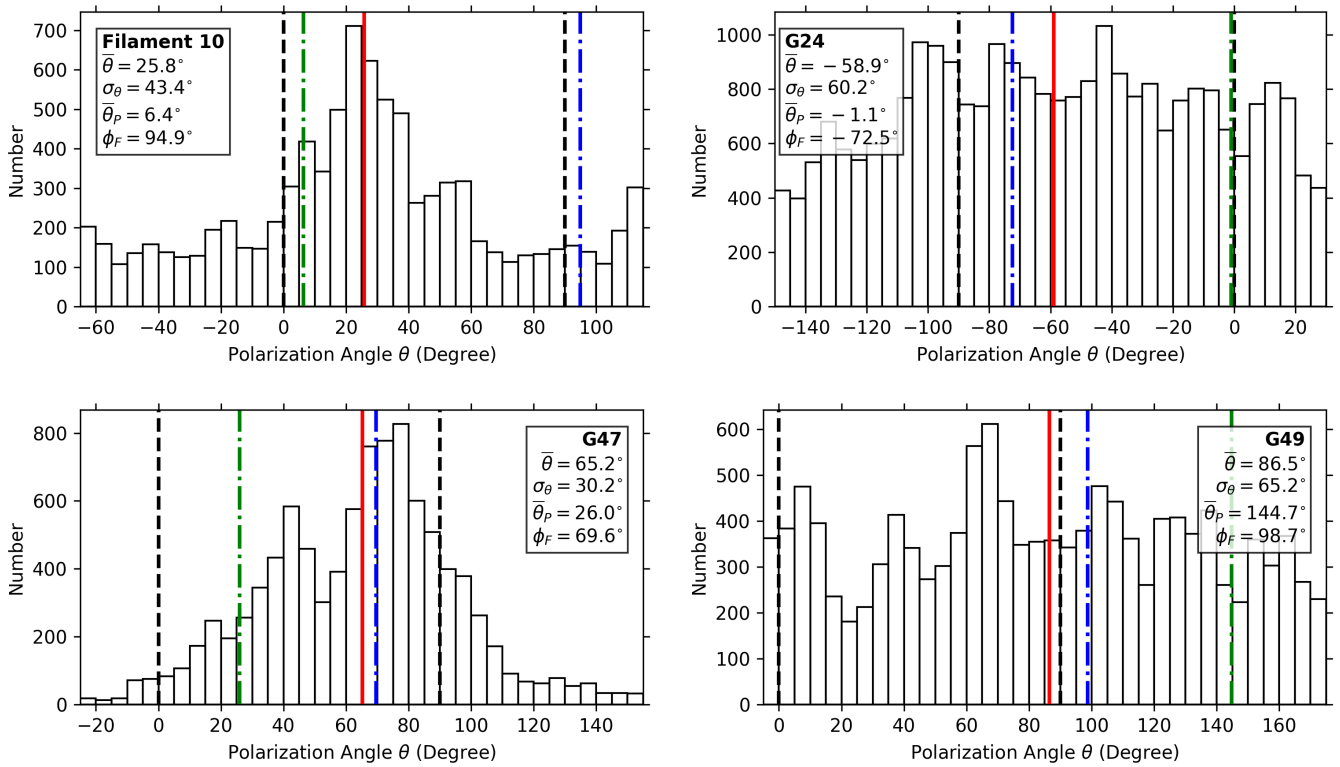

Figure 13. Histograms of polarization angles θ. Continued from Figure 12.

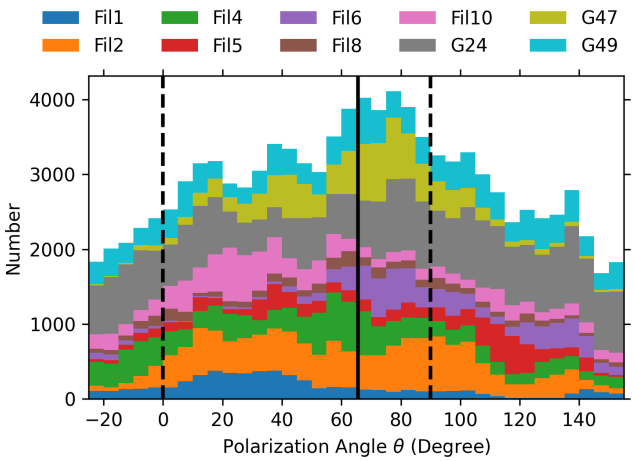

Figure 14. Stacked histogram of polarization angles θ for all the bones covered in Figures 12 and 13. The bin size of the histograms is 5°. Each color represents the contribution from a different bone. The histogram is centered on the bin containing the circular mean $\overline{\theta}$ of the stacked distribution, indicated by the plain black line at 65.°6. Black dashed lines indicate angles of 0° and 90° for clarity.

et al. (2004):

$$B_{\rm pos} = Q\sqrt{4\pi\rho}\,\frac{\sigma_V}{\sigma_\theta}, \tag{8}$$

where ρ is the gas density, σ_V is the nonthermal velocity dispersion of the gas, σ_θ is the dispersion of polarization angles, and Q is a theoretical correction factor often assumed to be ∼0.5 (E. C. Ostriker et al. 2001).

In the context of this paper, the main takeaway from Equation (8) is that the plane-of-sky amplitude $B_{\rm pos}$ is inversely proportional to the angle dispersion σ_θ, and so, larger angle dispersion will invariably result in weaker field strengths for a given gas velocity dispersion and density. However, the DCF method assumes a single ordered field direction for the entire region considered, which does not appear to be the case across the length of any of the bones considered for this survey. Additionally, simulations have shown that the DCF equation may be unreliable when the dispersion σ_θ is larger than 25°, as such values would likely be due to super-Alfvénic turbulence (E. C. Ostriker et al. 2001; I. W. Stephens et al. 2022). The circular standard deviation values listed in Figures 12 and 13 are all above 30°, which is well beyond that theoretical limit even when accounting for measurement uncertainties. It is therefore necessary to investigate the field strengths in more localized regions of the bones in order to obtain narrower dispersions of angles, as illustrated in Table 4.

In the specific case of G47, I. W. Stephens et al. (2022) measured the deviation σ_θ at different locations along its spine with the use of a rectangular $74\farcs0 \times 55\farcs5$ sliding box. With this approach, they found magnetic field strengths that are generally between 20 and 100 μG, with a maximum reaching nearly 200 μG. Most notably, however, is that the resulting mass-to-flux ratio λ (see R. M. Crutcher et al. 2004) for G47 is between 0.2 and 1.7, which means that most regions along the bone are either subcritical (i.e., they are supported against gravitational collapse by the magnetic field when $\lambda < 1$) or critical ($\lambda \approx 1$). The few regions that are supercritical ($\lambda > 1$) appear to be sites of active star formation.

Similarly, T. Pillai et al. (2015) used another variation of the DCF technique, based on the structure function (or angular dispersion function) defined by M. Houde et al. (2009), to find a magnetic field strength greater than 200 μG in Filament 6.

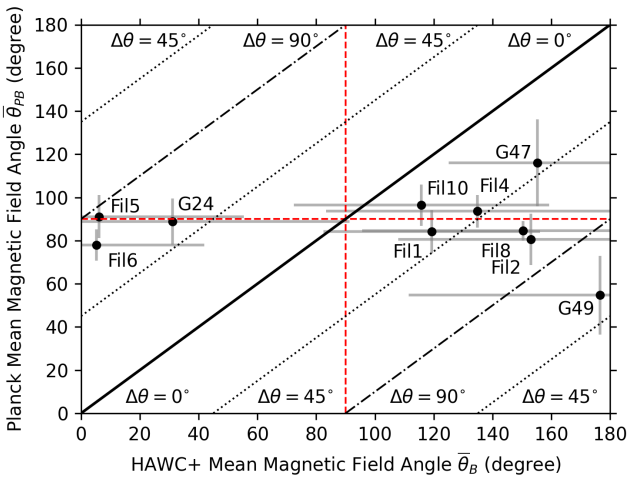

Figure 15. Comparison between the HAWC+ and Planck circular means for the inferred magnetic field angle in each filament. The gray error bars trace the circular standard deviation for both HAWC+ and Planck data. Each bone is identified with a label. The dashed red lines represent the Galactic disk orientation at 90°. The full, dotted, and dashed–dotted lines show the absolute angle differences $\Delta\theta$ of 0°, 45°, and 90°, respectively. The Planck mean magnetic field angles for each bone are closer to being parallel to the Galactic disk than those obtained from HAWC+.

The resulting mass-to-flux ratio λ has an upper limit of 1.1, and so, like G47, the magnetic field in Filament 6 is contributing significantly to supporting the cloud against gravity.

In each case, far from being weak and disordered, the magnetic field in Filament 6 and G47 is instead dynamically important to support these bones against gravitational collapse. The large angle dispersion values shown in Figures 12 and 13 should therefore be seen as an indirect probe of how much the magnetic field's orientation varies along the length of a bone, and not directly as a potential indicator of its strength. With this data release, the magnetic support analysis from I. W. Stephens et al. (2022) has been extended to all 10 bones observed as part of the FIELDMAPS survey to investigate if the trends seen in Filament 6 and G47 are common for Milky Way bones (I. W. Stephens et al. 2025).

3.5. Polarization Efficiency

The fractional polarization P from far-infrared observations can probe, to some extent, the alignment efficiency of a population of interstellar dust grains in a given environment (B. G. Andersson et al. 2015). In fact, this alignment efficiency is generally studied by measuring the polarization efficiency $\epsilon_p = P/\tau$, where τ is the optical depth, and assuming $P \propto \epsilon_p$ for optically thin dust emission in the far-infrared (T. J. Jones et al. 2015).

According to the RAT theory of grain alignment in particular, the polarization efficiency ϵ_p will depend on the grains' size distribution and the radiation field in their surroundings, among other parameters. In a nutshell, the amount of starlight that reaches the dust grains will directly impact how well they will align with magnetic field lines, and larger dust grains are also predicted to have a better alignment. For this reason, it may be more helpful to plot the polarization fraction P against the visual extinction A_V, as was done historically with optical and near-infrared observations. We note that there is a theoretical upper limit for large grains where the internal alignment through the Barnett effect becomes inefficient, but we do not expect it to be significant in the case of the typical Mathis–Rumpl–Nordsieck distributions of sizes in molecular clouds (J. S. Mathis et al. 1977; T. Hoang & A. Lazarian 2008).

However, measuring A_V from far-infrared and submillimeter observations of molecular clouds requires an accurate determination of the emissivity spectral index β and of the reddening factor R_V (e.g., T. J. Jones et al. 2015; S. Coudé et al. 2019). Since we assumed a fixed β of 1.75 (see Section 2.2), new SEDs with β as a free parameter will need to be fitted for each bone in order to obtain far-infrared opacity maps that could be converted into extinction maps. Furthermore, this future work would benefit from the addition of longer-wavelength data, such as observations at 850 μm from the James Clerk Maxwell Telescope (JCMT), to improve the determination of the spectral index β (e.g., S. I. Sadavoy et al. 2013).

Due to the challenges of calculating the visual extinction A_V from data at longer wavelengths, the Stokes I total intensity is sometimes used as an imperfect proxy for the optical depth. The relation between the debiased polarization fraction P defined in Equation (4) and the Stokes I total intensity is plotted in Figures 16 and 17 for the vector catalogs plotted in Figures 2–11. For each bone, we used least squares to fit the logarithmic form of the following power law:

$$P = A\, I^{\alpha}, \tag{9}$$

where A is a proportionality factor, and α is the power-law index. We find an average power-law index $\overline{\alpha}$ of -0.7 ± 0.1 for the entire sample when sampling every fourth vector (i.e., the width of the beam's FWHM), with the full range spanning from -0.59 to -0.91. The results are mostly unchanged when sampling every vector in each data set instead, and the related figures are also available on Dataverse. These indices are comparable to those found in nearby star-forming regions (approximately -0.8) using 850 μm polarization data from JCMT (e.g., from the BISTRO survey; J. Kwon et al. 2018; A. Soam et al. 2018; S. Coudé et al. 2019).

The relation between the polarization fraction P and Stokes I in Figures 16 and 17 reproduces the well-known phenomenon of depolarization, or polarization "hole," seen in high-density environments both in observations (e.g., J. L. Dotson 1996; B. C. Matthews et al. 2002; J. M. Girart et al. 2006; H. B. Liu et al. 2013; F. O. Alves et al. 2014; C. L. H. Hull et al. 2014) and theory (e.g., P. Padoan et al. 2001; T. J. Bethell et al. 2007; V. M. Pelkonen et al. 2009). A steeper power-law index α is expected for inefficient grain alignment in a cloud. With values below -0.5 for α, it is possible that dust grains are poorly aligned within the densest regions of bones. However, K. Pattle et al. (2019) found that the Ricean behavior of the noise δ_{I_p} for the polarization intensity I_p could artificially lead to a steeper power-law index α.

We calculated the reduced chi-square χ^2_r for each fit, which yielded values between 1.5 and 5.3. A value $\chi^2_r > 1$ could be understood as an imperfect fit to the data, but the values we obtain are not surprising considering the large spread of data points in Figures 16 and 17. We also provide the fitting uncertainties rounded up to the second decimal for the power-law index in each figure, but we caution against over-interpreting them due to the data spread. As a comparison

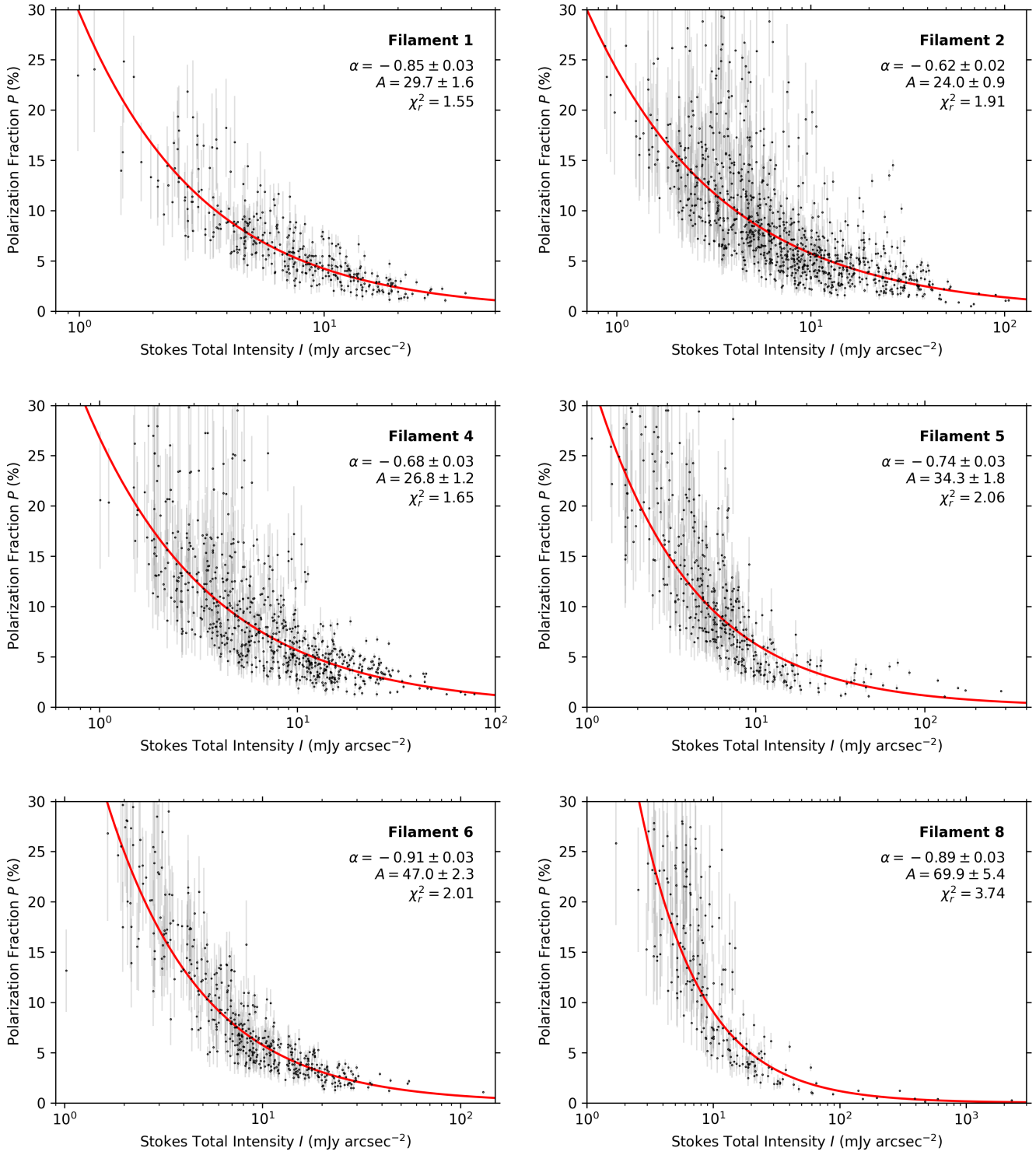

Figure 16. Debiased polarization fraction P as a function of the Stokes I total intensity for the vectors plotted in Figures 2–7. The intensity I is shown on a logarithmic scale to better visualize the spread of P for lower values of I. The best fit to the power law given in Equation (9) is shown as a red solid line for each bone, and the associated parameters A and α are provided directly on the plot. Only every fourth vector is plotted and used for the fit, and the uncertainty in P is shown as gray lines. Continued in Figure 17.

with the Barnard 1 clump, a dark cloud of the Perseus molecular cloud complex, S. Coudé et al. (2019) found a power index $\alpha = -0.85$ and $\chi^2_r = 3.4$, which they argued indicates that the data cannot be modeled accurately by a single power law. In this situation, a region-by-region analysis may be preferable in order to offset the changing physical conditions across the cloud.

Indeed, one of the reasons for the spread of data points in the relation between the polarization fraction P and the Stokes I total intensity, and the difficulty to fit them accurately

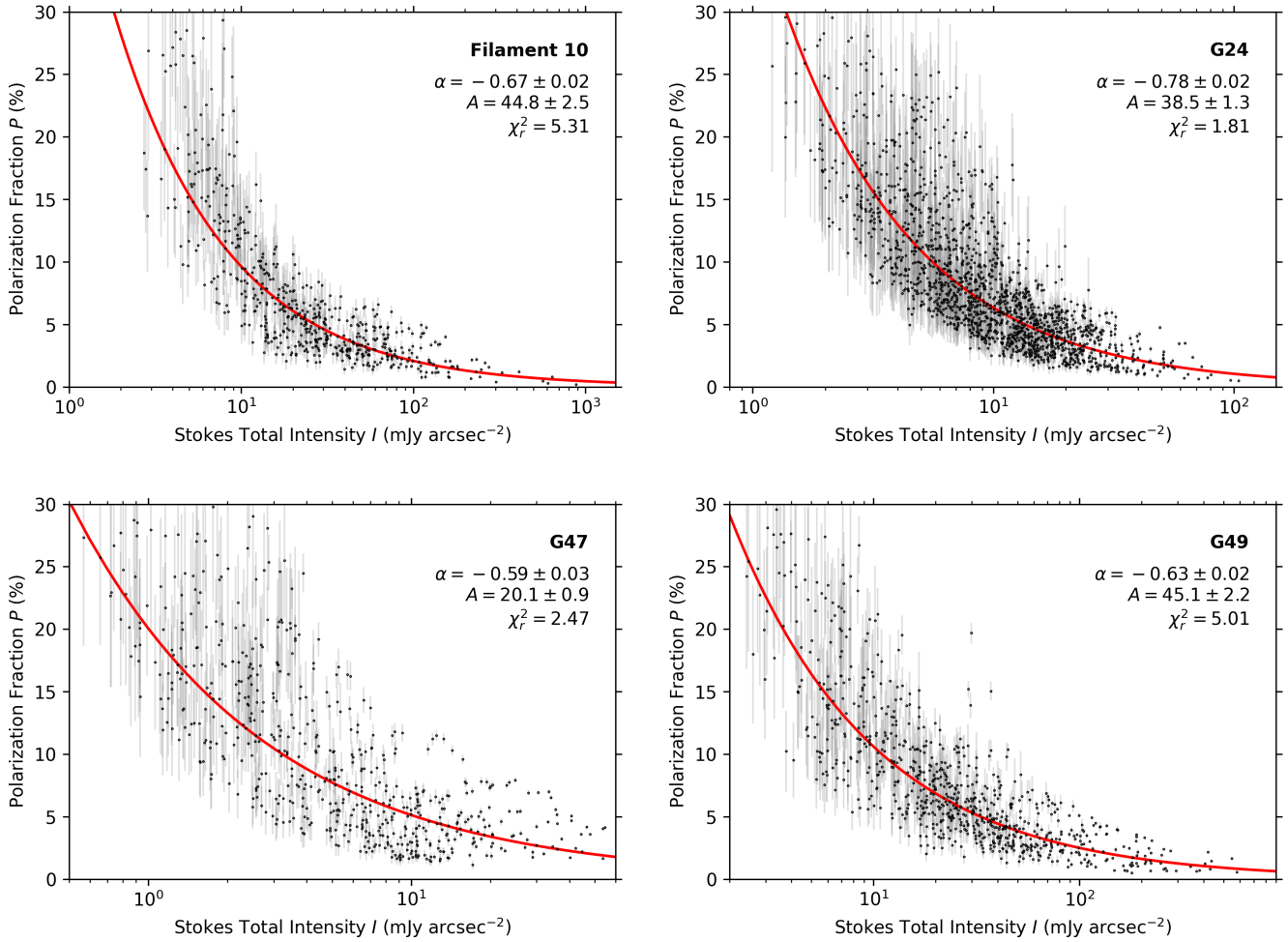

Figure 17. Debiased polarization fraction P as a function of the Stokes I total intensity for the vectors plotted in Figures 8–11. The intensity I is shown on a logarithmic scale to better visualize the spread of P for lower values of I. The best fit to the power law given in Equation (9) is shown as a red plain line for each bone, and the associated parameters A and α are provided directly on the plot. Only every fourth vector is plotted and used for the fit, and the uncertainty in P is shown as gray lines. Continued from Figure 16.

with a single power law, is that we are combining regions with different physical conditions within each bone. Since all the bones in our sample show signs of past or current star formation, it is likely that stellar feedback has affected dust properties across different regions (e.g., see Figure 24 in Appendix I for variations of dust temperatures T_d in Filament 10), which in turn would have an impact on the measured polarization P. Additionally, the dust emission in some regions could be optically thick at 214 μm, but not at 850 μm, which would complicate the comparison of the polarization fraction P between the two wavelengths.

In the far-infrared, the optical depth τ_ν at a frequency ν should be proportional to the hydrogen column density $N_{\rm H_2}$ when β is fixed (see Equation (A2) from T. J. Jones et al. 2015). We therefore investigated the relation between the polarization fraction P and the column density $N_{\rm H_2}$ for each bone, using the column density maps described in Section 2.2. We provide an example of this relation for Filament 10 in the left panel of Figure 25 in Appendix I, using HAWC+ Stokes I, Q, and U data smoothed and reprojected to the same resolution and pixel scale as the Herschel-derived maps. When fitting a power law of the form $P \propto N_{\rm H_2}^{\gamma}$, we find indices γ that are generally steeper than the indices α from Figures 16 and 17, even going as low as $\gamma = -1.40$. This result does not change if we instead use the same nonsmoothed vector catalogs as Figures 16 and 17. However, as exemplified in the left panel of Figure 25 in Appendix I, there is typically a larger spread of data points in each case compared to the relation between the polarization fraction P and Stokes I. These results suggest that the column density $N_{\rm H_2}$ measurements used in this work are not a better proxy for the visual extinction A_V than Stokes I.

Additionally, the polarization fraction P measured with HAWC+ could be overestimated in lower-density regions due to the filtering of large-scale dust emission in the data reduction pipeline. Figures 21 and 22 in Appendix F show that the measured HAWC+ spectral flux densities systematically underestimate those predicted with Herschel data at low intensities. Since the atmosphere is unpolarized, the effect of the background subtraction on the recovered low-level flux could be more pronounced for Stokes I than for Q and U due to how these parameters are individually treated by the HAWC+ pipeline. Following Equation (4), the resulting polarization fraction P would then be overestimated.

To explore this hypothetical effect on the power law given in Equation (9), we considered the unrealistic scenario where Stokes Q and U are fully recovered for large spatial scales by

the HAWC+ pipeline, but not Stokes *I*. We correct for such a discrepancy by replacing the HAWC+ Stokes *I* measurements with the Herschel-predicted 214 μm flux densities from Appendix F. While the resulting polarization fractions are systematically lower than those reported in Figures 16 and 17, the effect on the spectral index α is not as conclusive. Only four bones, Filaments 2, 5, 10, and G49, show new indices below -0.5, as illustrated in the right panel of Figure 27 in Appendix I for Filament 10. If differences exist between the large-scale filtering of Stokes *I*, *Q*, and *U* in the HAWC+ pipeline, they may be insufficient to account for the trends shown in Figures 16 and 17, at least not for all the bones in our sample. In any case, these results highlight the importance of developing instruments and observing strategies capable of reliably recovering fainter, more extended polarized dust emission in order to accurately measure the polarization fraction over a larger range of densities within molecular clouds. Space missions in particular, such as the proposed "PRobe far-Infrared Mission for Astrophysics" (PRIMA; e.g., A. Moullet et al. 2023; L. Cisela et al. 2025; C. D. Dowell et al. 2025; J. Glenn et al. 2025), do not need to remove the contribution of Earth's atmosphere to the data and therefore can more reliably recover large-scale polarized flux.

An additional mechanism to decrease the polarization fraction *P* is the "disruption" (or destruction) of dust grains by radiative torques (T. Hoang et al. 2019). Indeed, in the RAT paradigm of grain alignment, large dust grains could theoretically be torn apart by centrifugal forces if the ambient radiation field is strong enough. Assuming that dust grains are heated by the incoming starlight, the relation between the polarization fraction *P* and the dust temperature T_d can therefore be used to probe this effect. The alignment efficiency of the grains should increase with increasing dust temperature T_d until it reaches a threshold temperature, at which point the polarization fraction *P* will drop noticeably. Using this relation, L. N. Tram et al. (2021a, 2021b) found evidence for grain disruption near the high-mass star Oph S1 of the star-forming region ρ Ophiuchi A and in the starburst region of the 30 Doradus complex in the Large Magellanic Cloud. We also investigated the relation between the polarization fraction *P* and the dust temperature T_d for the FIELDMAPS bones, and we provide an example for Filament 10 in the right panel of Figure 25 in Appendix I using the same smoothed vector catalog as described previously for the gas column density $N_{\rm H_2}$. While there are signs of decreasing polarization fraction *P* above 26 K for some bones, conclusive results would require detailed modeling that is beyond the scope of this paper.

Finally, it is important to state that the polarization fraction *P* will also be affected by potentially unresolved magnetic field structures within the beam of the telescope (e.g., B. G. Andersson et al. 2015; K. Pattle & L. Fissel 2019; and references therein). For example, this could be the result of tangled field lines due to turbulent motions in the gas, which would lead to a polarization signal that partially cancels itself when integrated along the line of sight, thus reducing the polarization fraction. The inclination of field lines relative to the line of sight can also influence the observed fraction of polarization in filaments (Y. Doi et al. 2021b).

Multiwavelength observations in the far-infrared and millimeter regimes are required to lift the degeneracy of these competing effects on the polarization fraction *P*, as the observed grain alignment efficiency is expected to have a wavelength dependence while the integrated field directions should not (e.g., J. M. Michail et al. 2021; L. Fanciullo et al. 2022; L. N. Tram et al. 2024). With radio observations of Faraday rotation, it also becomes possible to measure the line-of-sight component of magnetic fields near GMFs, and thus have a measure of their 3D structure (e.g., M. Tahani 2022). In addition, combining optical polarimetry with distance measurements from the Gaia space telescope can identify the foreground components of dust polarization along the line of sight toward molecular clouds (Y. Doi et al. 2021a, 2024).

4. Discussion

In Section 3.4.1, we compared the magnetic field structure observed in the FIELDMAPS bones to the orientation of each filament and to the large-scale field probed with the Planck telescope. We found a mean difference and standard deviation of $-74^\circ \pm 32^\circ$ between the plane-of-sky magnetic field directions measured with HAWC+ at 214 μm and the filament orientations. The difference measured with Planck at 850 μm is $3^\circ \pm 21^\circ$ instead. The magnetic field orientations measured with HAWC+ are closer to perpendicular to the length of the filaments, which are themselves parallel to the Galactic plane. In comparison, the Planck data trace a field that is nearly parallel on average to the bones. As a reminder, the effective resolutions of HAWC+ at 214 μm and Planck at 850 μm are, respectively, 18.″7 and 5′.

When looking at the Galaxy as a whole with both dust polarization and synchrotron data, the Planck team determined that the Galaxy's magnetic field was homogeneously parallel to the disk up to Galactic latitudes of $\pm 10^\circ$ in most regions (Planck Collaboration et al. 2015a). However, this picture is complicated by the relatively low values of dust polarized intensity measured across the plane, which at the scales probed by Planck are likely due to unresolved field structures and integrated signal along the line of sight. The FIELDMAPS data confirm, at least in bones, that there can be significant changes in the field structure at higher resolutions, as illustrated by the histograms in Figures 12 and 13. Similarly, in the more turbulent Central Molecular Zone of the Galaxy, the FIREPLACE survey observed a complex magnetic field structure with a bimodal distribution split between parallel and perpendicular to the Galactic plane (D. Paré et al. 2024, 2025).

In addition, Planck Collaboration et al. (2016) found that magnetic field orientations tend to become more perpendicular to structures with hydrogen column densities $N_{\rm H}$ above $10^{21}\,{\rm cm}^{-2}$ in star-forming regions of the Gould Belt. The mean field orientations measured in FIELDMAPS data indicate that such a change in orientation must be occurring in bones, although with significant variations along the length of the filaments. In some bones, there is even evidence for a density threshold at which a perpendicular alignment is unambiguously preferred (I. W. Stephens et al. 2025). However, HAWC+ observations are generally only sensitive to higher column densities than those probed by Planck. If the transition in field orientation happens at similar densities in bones as in nearby star-forming regions, then the current Planck data may not be capable of identifying it due to the telescope's resolution and the position of these filaments within the Galactic plane. Higher-resolution observations of dust polarization probing the same densities as Planck are needed, such as those that would be achieved with PRIMA

(e.g., A. Moullet et al. 2023; L. Cisela et al. 2025; C. D. Dowell et al. 2025; J. Glenn et al. 2025).

Nevertheless, we can already make useful comparisons with observations of magnetic fields in other spiral galaxies. The "Survey on extragALactic magnetiSm with SOFIA" (SALSA) in particular found that magnetic fields are closely aligned to spiral arms in both far-infrared and radio data, although with some differences in pitch angle and polarization levels (A. S. Borlaff et al. 2021; E. Lopez-Rodriguez et al. 2022b, 2023). When viewed from within, the resulting plane-of-sky magnetic field would likely exhibit a strong component parallel to the disk, consistent with patterns inferred from the Planck polarization measurements of our own Galaxy (e.g., R. Beck 2015; Planck Collaboration et al. 2015a; A. S. Borlaff et al. 2023).

The SALSA survey also found lower polarization levels in spiral arms than in interarm regions, with the lowest values associated with the locations of active star formation in the arms (E. Lopez-Rodriguez et al. 2022b). Similarly to the Planck polarization measurements discussed previously, this discrepancy can be explained by unresolved field structures, such as a turbulent field in the denser star-forming material probed in the arms (A. S. Borlaff et al. 2021, 2023). Stellar feedback and turbulence from high-mass star formation activity are believed to contribute to the dynamo maintaining the magnetic field of spiral galaxies at large-scales (R. Beck 2015). If the FIELDMAPS bones are colocated with the spiral arms of our Galaxy (see Table 2), then they may be representative of comparable structures within the arms of other galaxies. In that case, the complex magnetic field morphologies observed in the FIELDMAPS polarization data at 214 μm may provide indirect evidence for unresolved structures in far-infrared observations of extragalactic sources.

In Galactic-scale simulations, the magnetic field associated with kiloparsec-long filaments in the cold neutral medium of spiral arms is generally parallel to their axis, in agreement with both Planck and extragalactic results for comparable column densities (R. Pillsworth et al. 2025). Furthermore, models with magnetic fields have been found to significantly increase the dense star-forming gas in filaments when compared to purely hydrodynamic models, with perpendicular fields increasing the accretion rate and line masses of the filaments (R. Pillsworth & R. E. Pudritz 2024). In some cases, magnetic fields can also extend the lifetime of star-forming filaments by dampening the effect of stellar feedback at small scales, allowing more than one episode of star formation to occur (R. Hix et al. 2023). The star formation tracers seen in the Spitzer data from Figure 1 and Appendix J may hint at such a scenario happening in bones. Finally, complex field structures akin to those observed along the length of the FIELDMAPS filaments may also be occurring in multiscale simulations as a result of a number of factors, such as turbulence from supernovae feedback and compression by the expansion of superbubbles (B. Zhao et al. 2024).

5. Summary

In this paper, we provided the full data release of the FIELDMAPS legacy survey, which mapped the polarized dust thermal emission in 10 candidate bones of the Milky Way, referred to here as bones for simplicity, at 214 μm using the HAWC+ camera on board SOFIA. The primary goal of this survey is to characterize the magnetic field structure within these bones, some of the densest filamentary structures associated with the spiral arms of the Galaxy. From these HAWC+ polarization observations, we created maps of the plane-of-sky magnetic field $B_{\rm pos}$ structure across each bone, compared to the gas column density $N_{\rm H_2}$ derived from Herschel observations and the large-scale field structure inferred from 850 μm measurements of polarization with Planck.

We quantified the distribution of polarization angles in all the FIELDMAPS targets. In each case, we identified the mean polarization directions from the 214 μm HAWC+ data and the 850 μm Planck data, as well as the orientation of the bone's spine. The average inclination of the bones is nearly parallel to the Galactic disk at $1^\circ \pm 11^\circ$. We find a mean difference of $-74^\circ \pm 32^\circ$ between their filament axis and the plane-of-sky component of the magnetic field seen by HAWC+. In comparison, the difference between the filament orientation and the large-scale field traced by Planck is $3^\circ \pm 21^\circ$. From these polarization data, we find that these large-scale fields change from being parallel to the Galactic disk to being closer to perpendicular, on average, to the long axis of each bone. At smaller scales, the magnetic field directions within bones are locally well defined, but can change significantly across their length.

We also produced maps of the polarization vectors for all the bones of the FIELDMAPS survey, as well as plots of the relation between the polarization fraction P and the Stokes I total intensity. We fitted a power law in each plot to investigate the polarization efficiency in the bones, and we found an average power-law index and standard deviation of $\alpha = -0.7 \pm 0.1$ across the entire sample. We find similarly steep indices when plotting the polarization fraction P against the gas column density $N_{\rm H_2}$ instead. These fitted indices are comparable to those measured in nearby molecular clouds, and they may point to poor grain alignment in the densest regions of bones. However, several additional factors could contribute to artificially lowering the indices measured from our HAWC + data, and follow-up studies using polarization observations at multiple wavelengths are needed to fully explore the alignment efficiency of dust grains in bones.

Finally, all the data products, analysis codes, and figures produced for this data release paper are made publicly available online at doi:10.7910/DVN/NUXGJE. With its uniform sample of 10 bones, the FIELDMAPS data release is an excellent starting point for follow-up studies using both current and future polarimeters.

Acknowledgments

The NASA/DLR Stratospheric Observatory for Infrared Astronomy (SOFIA) was jointly operated by the Universities Space Research Association (USRA), under NASA contract NNA17BF53C, and the Deutsches SOFIA Institut (DSI) under DLR contract 50 OK 0901 to the University of Stuttgart. Financial support for S.C. and I.W.S. was provided by NASA through award 08_0186 issued by USRA. L.W.L. acknowledges support from NSF AST-1910364 and NSF AST-2307844. P.S. was partially supported by a Grant-in-Aid for Scientific Research (KAKENHI numbers JP22H01271 and JP23H01221) of JSPS.

We thank Atilla Kovács for insightful discussions on the data reduction processes for polarization measurements and the intricacies of the CRUSH software (https://www.sigmyne.com/crush/). We also thank Jens Kauffmann for discussions

on the HAWC+ data reduction processes and Kate Pattle for discussions on depolarization.

We thank the HAWC+ instrument science team for the planning and acquisition of the data used in this project: Ryan Arneson, Peter Ashton, Melanie Clarke, Simon Coudé, Curtis DeWitt, Sareh Eftekharzadeh, Michael Gordon, Kyle Kaplan, Nicole Karnath, Enrique Lopez-Rodriguez, Steve Mairs, Ed Montiel, Dennis O'Flaherty, Sachin Shenoy, and Bill Vacca. Finally, we also thank everyone who contributed to SOFIA during its lifetime for their dedication to the success of this unique mission.

We also thank the anonymous referee for the insightful comments and suggestions.

Herschel was an ESA space observatory with science instruments provided by European-led Principal Investigator consortia and with important participation from NASA. This work was also based on observations obtained with Planck (http://www.esa.int/Planck), an ESA science mission with instruments and contributions directly funded by ESA Member States, NASA, and Canada.

This research has made use of the NASA/IPAC Infrared Science Archive, which is funded by NASA and operated by the California Institute of Technology, of NASA's Astrophysics Data System, and of APLpy, an open-source plotting package for Python (https://aplpy.github.io/).

Facilities: SOFIA, Herschel, Planck, IRSA.

Software: APLpy (T. Robitaille & E. Bressert 2012), Astropy (Astropy Collaboration et al. 2013, 2018, 2022), Photutils (L. Bradley et al. 2024), reproject (T. Robitaille et al. 2020), CARTA (A. Comrie et al. 2021).

Appendix A
Observing Modes

Nod-match-chop. The initial observing mode for HAWC+ was nod-match-chop, or chop-nod for short, a technique described in detail by R. H. Hildebrand et al. (2000). In this mode, the telescope array is moved, or "nodded," between two "nod" positions each found symmetrically on a line centered on the science target. At each "nod" position, the secondary mirror alternates, or "chops," at a frequency of 10.2 Hz between an "on" (target) and an "off" (sky) position. This process of chopping and nodding effectively creates two "off" positions that are used as time-dependent references to remove the sky emission during data reduction (D. A. Harper et al. 2018; M. Clarke et al. 2022). The chop amplitude and angle are chosen so that the "off" positions avoid astronomical sources of emission, although it is not always possible in crowded regions such as the Galactic disk. A typical chop amplitude for SOFIA was between $3\farcm5$ and $4\farcm2$. Additionally, the telescope array is dithered to four positions during a chop-nod observing sequence to limit the effect of bad pixels on the reduced observations. To be complete, a set of chop-nod observations also requires a pair of internal calibration files (IntCal) at the start and at the end in order to measure the phase delay needed for demodulating the chopping time stream, and to apply a flat-field correction accounting for detector gains and bad pixels. Overall, chop-nod when observing was less efficient than on-the-fly mapping due to the time spent off-source and the large overheads, but the sky removal for this technique is generally considered to be more reliable if no astronomical sources are found in the "off" positions.

Scan imaging. The second observing mode for HAWC+ was scan imaging, also often called on-the-fly mapping. Scan imaging was the primary mode for total intensity observations, and it was made available to the community for polarization observations as shared-risk starting in Cycle 8. The main scanning strategy used for HAWC+ was to perform a Lissajous pattern with the telescope array while keeping the secondary mirror fixed (D. A. Harper et al. 2018). A Lissajous pattern is a combination of two sinusoidal functions, one horizontal x and one vertical y, that is nonrepeating when the ratio of frequencies is irrational (in the case of HAWC+, $\omega_y/\omega_x \simeq \sqrt{2}$). Since such a Lissajous scan never returns to the exact same position, it minimizes the effect of various sources of noise in the data, such as bad pixels and the $1/f$ noise (A. Kovács 2008b). For a given reference frame, the parameters that could be tweaked for HAWC+ scans are the horizontal and vertical amplitudes, the range of initial scan angles, the scan rate (typically $100'' \, s^{-1}$ or $200'' \, s^{-1}$), and the duration. A caveat of using a Lissajous scan is that amplitudes that are significantly larger than the detector array's FOV can lead to lower sensitivities in the center of a map due to the larger amount of time spent at the edges.

Polarization. When performing polarization observations with any of the previously described observing modes, the half-wave plate for the selected filter was first inserted into the optical path of the instrument, and then, it was rotated to four distinct angles when observing: $5\fdg0$, $50\fdg0$, $27\fdg5$, and $72\fdg5$ (see D. A. Harper et al. 2018). These four angles are sufficient to recover the linear Stokes parameters (I, Q, and U; see Section 3.2) during data reduction (M. Clarke et al. 2022). Each HAWC+ band had an associated half-wave plate, except for bands A and B, which shared the same.

In chop-nod mode, the half-wave plate was rotated after each nod pair (ABBA; see D. A. Harper et al. 2018) for a given dither position. While this approach increased overheads, chop-nod when observing with HAWC+ generated a single file for each dither position that contains data for all of the four required half-wave plate angles. A typical set of chop-nod polarization observations therefore consists of four files, one for each dither position, sandwiched between two IntCals at the start and at the end. Since each file has all the required angle information, the data reduction pipeline can proceed even if some dither positions are missing (for example, if a set had to be interrupted for any reason).

In scan mode, the half-wave plate was rotated after individual scans. Each scan generated a single file, and so, each file contains information for a single half-wave plate position angle. A full polarization observation in scan mode therefore requires sets of four files, one for each position angle, in order to be processed by the data reduction pipeline. This method led to lower overheads since the half-wave plate was not rotated as often as when observing in chop-nod mode, but at the risk of having to discard an entire set of scans if even one was missing as all four scans had to be completed between line-of-sight rewinds of the telescope array. These rewinds were a necessary component of the stabilization mechanism used to negate the rotation of the sky on the detector array when observing, and this concept is explained in Section 1.2.4 in the SOFIA Observer's Handbook. Overall, polarization observations in scan mode were shown to be an improvement of a factor $\sim$1.8 in sensitivity relative to chop-nod for the same on-source time (E. Lopez-Rodriguez et al. 2022a).

Appendix B
Details of Data Acquisition

AORs were extensible markup language files created and modified using the Unified SOFIA Proposal and Observation Tool. They contained all the configuration information required by the instrument and the telescope array to perform the requested observations, and they were used as the reference to write the headers of the resulting FITS files. If needed, accurate information for individual AORs can be accessed through the headers of level 2 (corrected data) and level 3 (calibrated data) files, while the headers in level 3 (merged data) and level 4 (merged and multimission data) files contain information from only one of the AORs used for the mosaicked data. The ambiguous nomenclature for level 3 HAWC+ data is an historical quirk of the data reduction pipeline, but the two types can be differentiated on IRSA by the Product Type parameters *calibrate* and *merge*, respectively. We only provide level 4 data products as part of the FIELDMAPS survey data repository, and so, the FITS headers of corrected level 2 and calibrated level 3 data products on IRSA remain the best reference for exact information on the configuration of every observation performed for this survey.

In cases where the pipeline would crash during data reduction, we proceeded to inspect each individual polarization set that was obtained across all flights for the affected bones. We identified several anomalous level 0 files as the source of these crashes, and thus discarded them before rerunning the reduction pipeline described previously. As mentioned in Section 2.1.2, we list all the problematic level 0 files for each bone in this appendix. Otherwise, the most significant correction to the data was fixing the observations of Filament 4 taken during Flight 684. Due to a communication error between the instrument and the telescope array, there is a shift in the World Coordinate System (WCS) information recorded in the data for Flight 684. Appendix D explains how the level 2 data products for this flight were corrected to subpixel accuracy before being processed into level 3 and 4 data products.

Filament 1. Filament 1 was observed with HAWC+ in scan mode on Flights 726 (2021 May 5) and 729 (2021 May 11). Files 90 and 111 from Flight 726 were discarded as they are calibration files erroneously associated with this program. Furthermore, two sets of four files from Flight 726 were discarded due to generating errors during data reduction: files 162–165 and 186–189, inclusively. The final level 4 data product was obtained by mosaicking two pointings with overlapping fields of view (AORs #60 and 61).

Filament 2. Filament 2 was observed with HAWC+ in scan mode on Flights 727 (2021 May 6) and 879 (2022 June 1). The final level 4 data product was obtained by mosaicking four pointings with overlapping fields of view (AORs #62, 63, 64, 65, 104, and 105).

Filament 4. Filament 4 was observed with HAWC+ in scan mode on Flights 684 (2020 September 10) and 685 (2020 September 11). Due to a communication error between the instrument and the telescope array, there is a shift in the WCS information for observations taken on Flight 684. Appendix D describes how this shift was corrected manually during the data reduction process. Two sets of four files from Flight 684 were discarded: files 25–28 due to exhibiting a larger WCS shift than other observations during that night, and 74–77 for exhibiting an additional drift in WCS coordinates within a single set of half-wave plate positions. The final level 4 data product was obtained by mosaicking two pointings with overlapping fields of view (AORs #66, 67, 92, 93, and 94).

Filament 5. Filament 5 was observed with HAWC+ in scan mode on Flights 728 (2021 May 7), 732 (2021 May 14), and 734 (2021 May 19). Files 97 and 138 on Flight 732, and 100, 172, and 174 on Flight 734, were discarded due to generating errors during data reduction. All files from Flight 728 were also removed because they showed clear discrepancies with the data obtained during Flights 732 and 734. Based on the flight summary for Flight 728, the calibration of the data obtained for Filament 5 may have been affected by attempts to extend the duration of HAWC+'s cryogenic system during the last leg of the flight.[22] The large instrumental phase offsets observed when performing internal calibration tests on that night did not affect the quality of the observations for G49 compared to Flights 726 and 733, and so, these offsets are unlikely to have independently impacted the data for Filament 5. The final level 4 data product was obtained by mosaicking three pointings with overlapping fields of view (AORs #68, 69, and 70).

Additionally, Filament 5 was also observed at 214 μm with HAWC+ in chop-nod mode on Flight 441 (2017 October 18) for program 05_0109. Unfortunately, even when using a chop distance of 7.′5, one of the two "off" positions used for background subtraction contained a far-infrared source, and so, a fake negative source is found at $l = +18{:}35{:}54.456$ and $b = -0{:}04{:}52.005$. Only one pointing was observed for this program (AOR #4). These observations were followed up at 53 μm on Flight 485 (2018/07/12) for program 06_0206 with a single pointing (AOR #8).

Filament 6 (The Snake). Filament 6 was observed with HAWC+ in chop-nod mode for program 05_0206 on Flight 394 (2017/05/12), and for program 06_0027 on Flight 486 (2018 July 13). The final level 4 data product was obtained by mosaicking seven pointings with overlapping fields of view, two from program 05_0206 (AORs #1, 2) and five from program 06_0027 (AORs #1, 2, 3 , 4, and 5).

Filament 8. Filament 8 was observed with HAWC+ in scan mode on Flight 892 (2022 June 30). The final level 4 data product was obtained by mosaicking three pointings with overlapping fields of view (AORs #73, 74, and 118).

Filament 10. Filament 10 was observed with HAWC+ in scan mode on Flight 894 (2022 July 5). The final level 4 data product was obtained by mosaicking eight pointings with overlapping fields of view (AORs #75, 76, 77, 78, 112, 113, 114, and 115).

G24. G24 was observed with HAWC+ in scan mode on Flights 880 (2022 June 2), 881 (2022 June 3), 882 (2022 June 4), and 886 (2022 June 11). The final level 4 data product was obtained by mosaicking 12 pointings with overlapping fields of view (AORs #79, 80, 81, 82, 83, 84, 106, 107, 108, 109, 110, and 111).

G47. G47 was observed with HAWC+ in scan mode on Flights 687 (2020 September 15), 689 (2020 September 23), and 690 (2020 September 24). The final level 4 data product was obtained by mosaicking four pointings with overlapping fields of view (AORs #85, 86, 87, and 100). These observations were previously published by I. W. Stephens et al. (2022).

[22] See https://irsa.ipac.caltech.edu/data/SOFIA/docs/proposing-observing/flight-plans/index.html.

G49. G49 was observed with HAWC+ in scan mode on Flights 726 (2021 May 5), 728 (2021 May 7), and 733 (2021 May 18). File 160 from Flight 733 was discarded as it is a calibration file erroneously associated with this program. Contrary to Filament 5, observations of G49 during Flight 728 do not show any obvious discrepancy with those obtained during Flights 726 and 733. The final level 4 data product was obtained by mosaicking four pointings with overlapping fields of view (AORs #88, 89, 90, and 91).

Appendix C
Extended Analysis of the Polarization Data in Filament 5

As noted in Section 2.1.1 and Appendix B, Filament 5 was the only bone in our sample observed with HAWC+ in polarization using both chop-nod and scan modes. It is therefore the only target where we can effectively quantify the differences between these two modes. We also used the data for Filament 5 to investigate the effect of the SOFIA Redux scan mode reduction parameters *fixjumps* and *rounds*. Finally, Filament 5 is also the only bone with observations at 53 μm (band *A*), which we also present in this appendix.

We focus first on the differences in the Stokes *I* total intensity and the polarization angle θ between the two observing modes. As a reminder, the polarization angle θ is a function of both Stokes Q and U (see Equation (6)), and it is the crucial quantity to characterize the plane-of-sky magnetic field structure in the bones. For this analysis, we use the data in the ICRS reference frame as it is the default format used by the reduction pipeline. We therefore use Stokes $Q_{\rm icrs}$ and $U_{\rm icrs}$ instead of Stokes $Q_{\rm gal}$ and $U_{\rm gal}$, and the resulting polarization angle θ is defined following the IAU convention from celestial north to east. In Figure 18, we use the magnetic field angle θ_B, which is simply $\theta_B = \theta + 90^\circ$, to better relate the different data reduction results with those from Figures 2–11.

Figure 18 presents the inferred magnetic field maps of Filament 5 for different data reduction products in chop-nod and scan modes. As illustrated by the intensity contours in each panel, the chop-nod data recover more low-level extended emission than the scan mode data. However, the chop-nod data also display significant negative flux that does not exist in the scan mode data (see also the left panel of Figure 19), which is indicative of bright sources in one or both of the "off" positions for the chop-nod observations. These characteristics fit the expected limitations of the chop-nod and scan observing modes, as discussed in Appendix A. Considering that all the bones observed for FIELDMAPS are in crowded regions of the sky in the far-infrared, the existence of significant negative sources in the chop-nod data for Filament 5 is further evidence supporting the choice of scan mode when observing for this survey.

Figure 19 shows the comparison in Stokes *I* total intensity and in polarization angle θ between chop-nod and scan mode data for Filament 5. The Stokes *I* intensity and the polarization angle θ are, respectively, identified as I_{ch} and θ_{ch} for the chop-nod data, and I_{sc} and θ_{sc} for the scan data. These maps were obtained by reprojecting the scan data to the same grid as the chop-nod data using the REPROJECT package. As noted previously, the intensity ratio map in the left panel of Figure 19 exhibits regions with negative flux close to the source, which also impacts the surrounding areas. The region with the largest angle difference in the right panel is also the one closest to this negative flux in the south part of the map.

We fitted a linear relation $I_{sc} = a\, I_{ch} + b$ to the intensities measured in the chop-nod and scan mode data for the pixels plotted in the left panel of Figure 19. We found a coefficient $a = 0.95$ and a constant $b = -4.5$ mJy arcsec^{-1}. While some additional low-level flux is recovered in the chop-nod data, the linear trend between the data products is only 5% away from a perfect 1:1 correlation, which is comparable to the calibration uncertainties for HAWC+ (D. A. Harper et al. 2018). For the difference of polarization angles between the two modes for the pixels shown in the right panel of Figure 19, we find an average value $\langle \theta_{ch} - \theta_{sc} \rangle$ of $2\overset{\circ}{.}8$ and a standard deviation of $15\overset{\circ}{.}0$. As a reference, the median angle uncertainty δ_θ for each mode in these pixels is approximately 5°, with a minimum of 1° and a maximum of 9°. Overall, we find a reasonably good agreement between the chop-nod and scan data for the pixels that can be directly compared in Filament 5.

To investigate the effect of the two observing modes on the quantities derived in Section 3.5 for Filament 5, we fitted a power law following Equation (9) to the relation between the polarization fraction *P* and the Stokes *I* intensity. We specifically limited our analysis to the region displayed in Figure 18. For the chop-nod data, we find a power-law index $\alpha = -0.78 \pm 0.01$, while the scan data give an index $\alpha = -0.69 \pm 0.01$. Of note, using a subset of the scan data for Filament 5 gives a shallower result for the index α than reported in Figure 16. However, the difference $\Delta\alpha = 0.09$ between the chop-nod and scan data is larger than the fit uncertainties of 0.01. This could be an indication that the statistical uncertainties reported in Section 3.5 for the power-law fits may be underestimating the real measurement uncertainties when including the entire bone. Additionally, an underestimation of Stokes *I* from extended emission in the scan data could lead to a significantly different index α, as seen in the right panel of Figure 27 in Appendix I.

We also tested scan mode data reduction products using differing parameters when running SOFIA Redux. Figure 18 shows the results for the data product used in this paper (top right panel), the data product obtained when using *fixjumps* = *False* (bottom left panel), and the data product obtained when using *rounds* = 60 (bottom right panel). While not pictured, we also ran a reduction with *fixjumps* = *True* and *rounds* = 15. Increasing the number of iterations in the pipeline from 30 to 60 appears to help recover additional vectors in the middle clump of Filament 5, which agree with those from the chop-nod data, but otherwise, improvements elsewhere are minor. The largest increase in the number of recovered vectors is when we use *fixjumps* = *False*. However, there is a nearly 90° difference, in the polarization angles measured in the southern part of the plots in Figure 18, between the *True* and *False* products. Critically, the chop-nod map shows a closer agreement with the scan mode data using *fixjumps* = *True*. Increasing the number of detections is meaningless if the recovered angles cannot be trusted in parts of the map, and so, a conservative approach using the *fixjumps* = *True* parameter is warranted in our systematic reduction of the bones for FIELDMAPS.

In general, the *fixjumps* parameter is useful when an HAWC+ detector displays an anomalously high flux relative to its neighbors, which usually appear as a "worm" on the Stokes *I* map of the final data reduction product (M. Clarke & R. V. Vliet 2023). Otherwise, the resulting polarization maps should be mostly comparable between *fixjumps* = *False* and

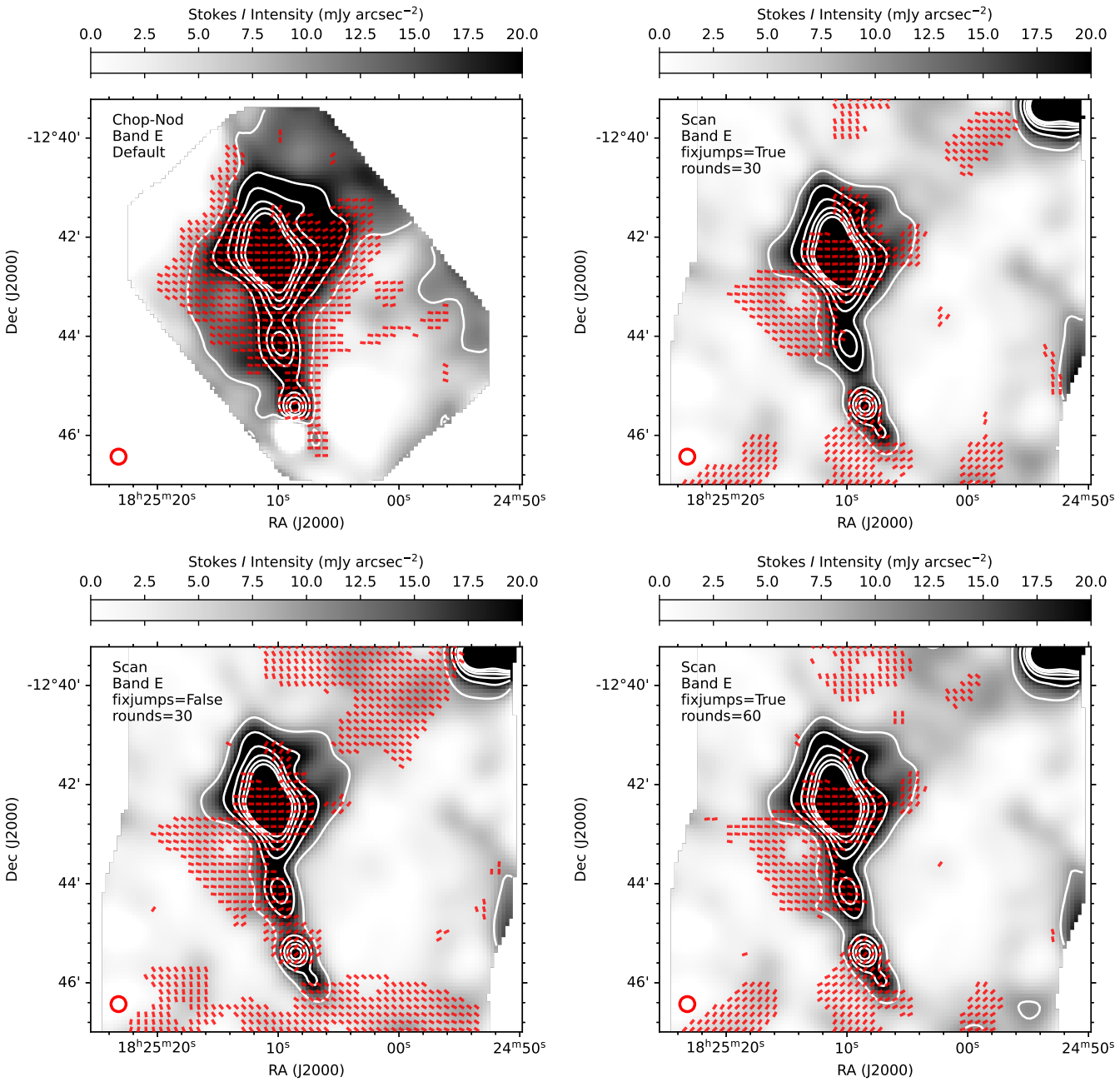

Figure 18. The magnetic field structure (red single-length vectors) inferred from HAWC+ 214 μm (band *E*) observations for four different data reduction procedures for Filament 5. Every other vector is plotted. The gray scale is the measured 214 μm Stokes *I* total intensity, and the white contours trace levels of 10–60 mJy arcsec^{-2} by steps of 10 mJy arcsec^{-2}. The red circle shows the beam of HAWC+ at 214 μm. Top left: chop-nod data reduced using the default pipeline parameters. Top right: scan mode data reduced using *rounds* = *30* and *fixjumps* = *True* (see also Figure 5 for a full map). Bottom left: scan mode data reduced using *rounds* = *30* and *fixjumps* = *False*. Bottom right: scan mode data reduced using *rounds* = *60* and *fixjumps* = *True*.

True. Several factors may have contributed to seeing such a strong difference between these two values in our data for Filament 5. First, the region shown in Figure 18 lies at the interface between two distinct pointings, which could make it more susceptible to potential edge effects, such as higher noise. Additionally, the coverage between the two fields is uneven due to losing the data from Flight 728 (see Appendix B), with the northernmost field showing a higher noise level by approximately a factor of 2. A greater emphasis was put on acquiring more even coverage of the bones in subsequent observations for the survey, but unfortunately, the SOFIA mission concluded before Filament 5 could be revisited.

Interestingly, the polarization vectors seen in the brightest region of Figure 18 agree somewhat between the *fixjumps* = *False* and *True* data products. Since the dust emission is much weaker south of this region (see the bottom panel of Figure 5), a plausible explanation would be that a detector flux jump while this pointing was observed may have had a greater effect on the background subtraction in the Stokes parameters due to the relatively low signal-to-noise emission. An inspection of each data product, all available in the online repository, reveals that this is indeed the location where the Stokes *U* maps differ the most, which would explain the observed changes in polarization angle.

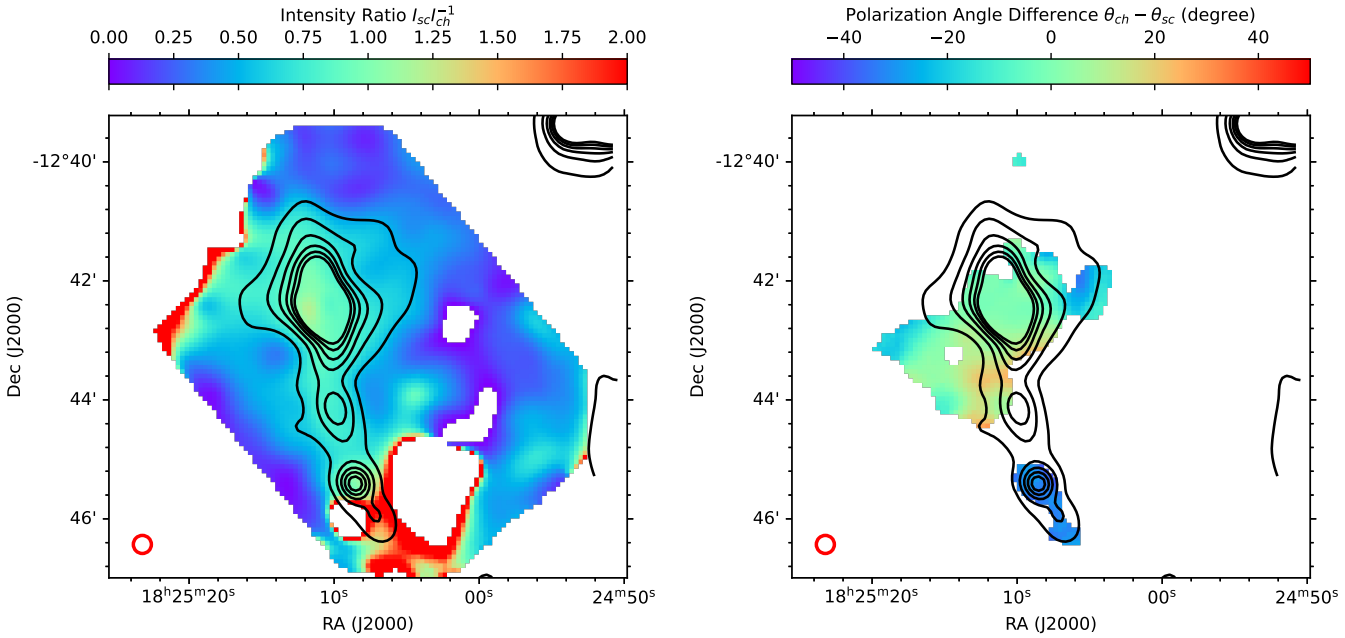

Figure 19. Comparison between chop-nod and scan mode data for Filament 5. The Stokes I, Q, and U data from the scan mode observations were regridded to match the chop-nod data. The black contours trace the Stokes I total intensity from the scan mode map from 10 to 60 mJy arcsec^{-1} by steps of 10 mJy arcsec^{-1}. The HAWC+ beam is given as a red circle in each panel. Left: the intensity ratio $I_{sc}I_{ch}^{-1}$ is shown on a rainbow scale for the pixels where $I > 0$ in both maps. Right: the difference of the polarization angles $\theta_{ch} - \theta_{sc}$ is shown on a rainbow scale for the pixels where $P/\delta_P > 3$, $P < 30\%$, and $I/\delta_I > 10$ in both maps.

Finally, we present in Figure 20 the polarization and plane-of-sky magnetic field maps of Filament 5 derived from 53 μm (band A) chop-nod observations with HAWC+. The smaller FOV in band A covers only the brightest, northernmost clump shown in Figure 18. This region is associated with the massive IRAS 18223-1243 YSO (S. J. Chan et al. 1996) and its compact H II region (M. Sewilo et al. 2004), making it a clear site of high-mass star formation. In order to compare the polarization angles between the two wavelengths, we reprojected the scan data at 214 μm to the same grid as the chop-nod data at 53 μm. We find a mean angle difference $\langle\theta_{53} - \theta_{214}\rangle$ of $-13\overset{\circ}{.}3$ and a standard deviation of $12\overset{\circ}{.}0$. While the 214 μm observations are significantly oversampled, this comparison shows that the 53 μm polarization data exhibit more structure at smaller scales while still being mostly aligned in the same direction overall. Following Equation (9), we also fitted a power-law function to the relation between the polarization fraction P and the Stokes I total intensity at 53 μm, and we find a power-law index α of -0.88 ± 0.01.

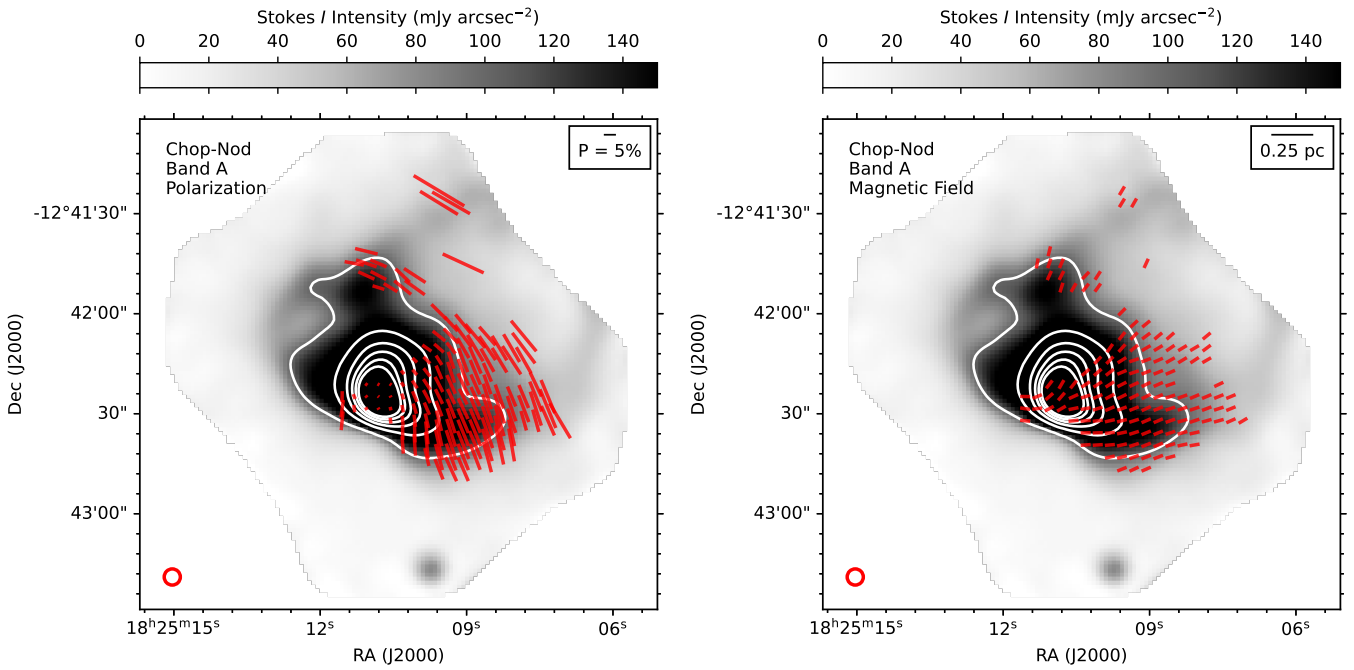

Figure 20. Chop-nod observations of Filament 5 with HAWC+ at 53 μm (band *A*). The gray scale is the measured 53 μm Stokes *I* total intensity, and the white contours trace levels of 100–600 mJy arcsec^{-2} by steps of 100 mJy arcsec^{-2}. The red circle shows the beam of HAWC+ at 53 μm. Left: polarization map shown as red vectors with the length representing the polarization fraction *P*. Right: inferred magnetic field map shown as red single-length vectors. A scale length of 0.25 pc is given for reference.

Appendix D
Reference Frame Correction in Filament 4

Due to a communication error between the instrument and the telescope array during SOFIA Flight 684 (2020 September 10), all the observations taken for Filament 4 on that night had incorrect WCS information in their headers. Instead of discarding the data from this flight, which represented nearly half of the total observations for Filament 4, we attempted to measure this coordinate shift and apply a correction directly to the headers of the level 2 data before the calibration and merging steps described in Section 2.1.3.

The HAWC+ coverage for Filament 4 contains a candidate massive YSO associated with an HII region that appears as a near-perfect circle for the SOFIA beam at 214 μm (G021.3570-00.1795 from J. S. Urquhart et al. 2009, also IRAS 18279-1024). This fortunate occurrence provided us with a reference source that could be easily fitted with a 2D Gaussian, thus helping to accurately determine its centroid position in data from both Flights 684 and 685.

Before we proceeded to fix the WCS information, however, we first completed a visual inspection of each HAWC+ polarization data set obtained during Flight 684, and compared them with those from Flight 685. As mentioned in Appendix B, we removed files 25–28 due to displaying a seemingly larger coordinate shift than the rest of the data. We could not measure this shift accurately since the FOV for these files did not include G021.3570-00.1795, and so removing them served as a precaution to avoid including a potential pointing error in the final data product. We also removed files 74–77, as they showed an obvious pointing instability between individual half-wave plate positions, leading to duplicated sources in the data.

Reducing the remaining files for Flight 684 created six level 2 data products, three of which contained G021.3570-00.1795 in their FOV. We used the CENTROID_2DG function from the PHOTUTILS package to fit a 2D Gaussian to this source and determine its centroid position for each level 2 file. The pointing error was measured with the standard deviation of the fitted centroid positions in each file. For Flight 684, we found a pointing error of 0.42 pixel in R.A. and 0.16 pixel in decl. For Flight 685, the pointing error of the four level 2 data products containing G021.3570-00.1795 is 0.05 pixel in R.A. and 0.04 pixel in decl. While the pointing accuracy for Flight 685 is superior, finding a subpixel pointing accuracy (or less than a quarter of the beam size) for Flight 684 nevertheless reassured us that a single positional shift could be implemented to fix all six level 2 products from this flight.

We calculated the required positional correction by taking the difference of the average centroid position of G021.3570-00.1795 between Flights 684 and 685, which is $-0\overset{\circ}{.}049397$ in R.A. and $0\overset{\circ}{.}130828$ in decl. The six corrected level 2 data products for Flight 684 were then generated with new headers where these values were added to the original CRVAL1 and CRVAL2 keywords. Finally, all the corrected level 2 data products from Flight 684 were combined with those from Flight 685 in the SOFIA Redux pipeline to obtain updated level 3 and level 4 products for Filament 4. For future reference, the level 2 files and the Python codes used for this reference frame correction in Filament 4 are included in the online data repository for this paper.

Appendix E
Reprojection to Galactic Coordinates

E.1. SOFIA

After the FIELDMAPS data have been reduced following the procedure described in Section 2.1.3, each level 4 data product was transformed from the ICRS to the GCS. In this

appendix, we describe in detail the steps of this conversion process. The codes used for the reprojection to Galactic coordinates for each bone are included as part of the FIELDMAPS data release.

First, for each extension of the original data products, a copy of the FITS header is used as a template where only specific keywords are modified. The CTYPE1, CTYPE2, and WCSNAME keywords are updated to reflect the new GCS reference frame. The CRVAL1 and CRVAL2 values are converted from ICRS to GCS using Astropy's SkyCoord class. The NAXIS1 and NAXIS2 values are increased to allow for the rotation of the FOV without cropping any astronomical data.

These modified FITS headers are then used as the reference when reprojecting each extension of the level 4 data products from ICRS to GCS. Specifically, we use the reproject_exact function from the REPROJECT Python package. These reprojected extensions are then recombined into a new FITS container, including a copy of the three tabular extensions described in Table 2 of M. S. Gordon et al. (2018).

In order to complete the conversion to the GCS reference frame, the Stokes $Q_{\rm icrs}$ and $U_{\rm icrs}$ parameters have to be recalculated to obtain Stokes $Q_{\rm gcs}$ and $U_{\rm gcs}$. To achieve this, we must first determine the rotation of the polarization angle from $\theta_{\rm icrs}$ to $\theta_{\rm gcs}$ on the plane on the sky for each pixel position. This rotation is described by the following equation (I. Appenzeller 1968; G. Panopoulou et al. 2016; G. V. Panopoulou et al. 2016):

$$\theta_{\rm gcs} - \theta_{\rm icrs} = \frac{180^\circ}{\pi} \arctan \times \left(\frac{\sin(l_{\rm cnp} - l)}{\tan b_{\rm cnp} \cos b - \sin b \cos(l_{\rm cnp} - l)} \right), \quad \text{(E1)}$$

where l and b are the Galactic longitude and latitude in radians of a given pixel. We use the two-argument arctan 2 function in Python to lift the quadrant degeneracy of arctan when dividing the Stokes U and Q parameters. The coordinates $l_{\rm cnp}$ and $b_{\rm cnp}$ of the celestial north pole are 2.145 radians (122.°9) and 0.473 radians (27.°1), respectively.

The polarization intensity I_p should remain the same in both reference frames, so we have

$$I_p = \sqrt{Q_{\rm icrs}^2 + U_{\rm icrs}^2} = \sqrt{Q_{\rm gcs}^2 + U_{\rm gcs}^2}. \quad \text{(E2)}$$

Knowing the rotated polarization angle $\theta_{\rm gcs}$, we can then use the definition of the Stokes parameters from Section 3.2 to find $Q_{\rm gcs} = I_p \cos(2\,\theta_{\rm gcs})$ and $U_{\rm gcs} = I_p \sin(2\,\theta_{\rm gcs})$. The Stokes I total intensity also does not depend on the reference frame ($I_{\rm gcs} = I_{\rm icrs}$), and the same can be assumed for the error maps of each Stokes parameter (δI, δQ, δU).

With the Stokes $I_{\rm gcs}$, $Q_{\rm gcs}$, and $U_{\rm gcs}$ parameters, we can use Equations (4) through (7) to recalculate the polarization properties of the bones, such as the debiased polarization fraction P, the polarization angle θ, the magnetic field angle θ_B, and their related uncertainties. While they are not directly used in this paper, we nonetheless run the original data products in the ICRS reference frame through the same equations to provide data products with polarization properties calculated following an identical procedure in each coordinate system. These files are all available through the survey's data repository.

E.2. Planck

Polarization angles from Planck observations are measured clockwise from Galactic north to west (Planck Collaboration et al. 2015a) in a similar manner to the COSMO/HEALPix convention (K. M. Górski et al. 2005), which is opposite to the IAU's convention of measuring polarization counterclockwise from north to east (e.g., J. P. Hamaker & J. D. Bregman 1996). While this work uses the same GCS frame as the Planck data, we follow the IAU convention for measuring polarization angles from Galactic north to east. This results in a sign difference between the Stokes $U_{\rm cmb}$ parameters from the Planck archival data and the Stokes U_P parameters from this work, assuming the units for the Planck data have already been converted using the values from Table 6 of Planck Collaboration et al. (2014).

As before, the polarized intensity I_p is unaffected by the choice of reference frame,

$$I_p = \sqrt{Q_{\rm cmb}^2 + U_{\rm cmb}^2} = \sqrt{Q_P^2 + U_P^2}, \quad \text{(E3)}$$

and the polarization angle ψ for Planck in the COSMO convention is defined using the Stokes $Q_{\rm cmb}$ and $U_{\rm cmb}$ parameters as follows:

$$\psi = \frac{180^\circ}{2\pi} \arctan\left(\frac{Q_{\rm cmb}}{U_{\rm cmb}} \right). \quad \text{(E4)}$$

Since the only difference between the two reference frames is the direction from which the angle is measured relative to Galactic north, the relation between the polarization angle ψ in the COSMO convention and the polarization angle θ_P in the GCS reference frame for Planck is simply given by

$$\theta_P = \frac{180^\circ}{\pi} \arctan\left(\frac{-\sin\psi}{\cos\psi} \right), \quad \text{(E5)}$$

with the Stokes parameters $Q_P = I_p \cos 2\,\theta_P$ and $U_P = I_p \sin 2\,\theta_P$. Using these equations, we easily verify that only the sign of Stokes U changes between the two measurement conventions. In each case, as with Equation (E1), we use the arctan 2 function in Python to avoid the inherent quadrant degeneracy of arctan. Finally, with Stokes Q_P and U_P in the GCS frame, the polarization properties for the Planck data are recalculated using Equations (4) through (7).

Appendix F
Comparison with Herschel Data

As noted in Section 2.2 and in Appendix A, the removal of the atmospheric background from HAWC+ observations creates a discrepancy between the background fluxes measured by SOFIA and Herschel. In this appendix, we use the maps of the hydrogen column density $N_{\rm H_2}$ and dust temperature T_d derived from Herschel observations for the FIELDMAPS bones to quantify this difference in the measured flux densities at 214 μm between the two observatories.

The flux density I_ν at a frequency ν for dust thermal emission is obtained from the following modified blackbody equation:

$$I_\nu = N_d\, \kappa_\nu\, B_\nu(T_d), \quad \text{(F1)}$$

where N_d is the dust column density, κ_ν is the dust opacity at frequency ν (e.g., V. Ossenkopf & T. Henning 1994), and

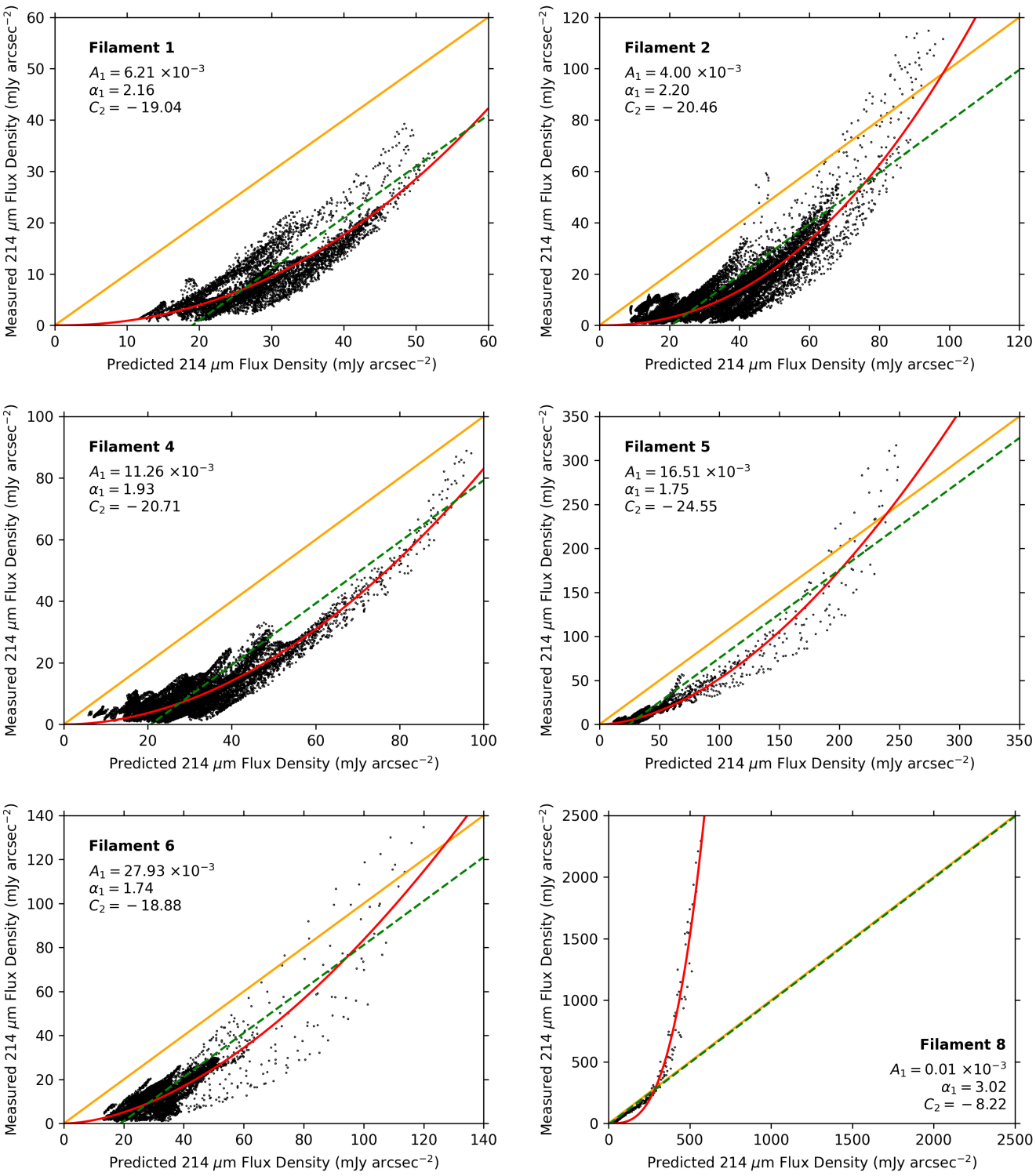

Figure 21. Comparison between the measured and predicted flux densities at 214 μm for each FIELDMAPS bone. Continued on Figure 22. The measured flux densities are taken from the HAWC+ Stokes I total intensity maps shown in the bottom panels of Figures 2–11. The predicted flux densities are calculated from Equation (F1) using the Herschel-derived maps of hydrogen column density $N_{\rm H_2}$ and dust temperature T_d. The full orange line shows a 1:1 relation between the predicted $I_{\rm est}$ and measured I_m flux densities, the full red line shows a power-law fit of the form $I_m = A_1\, I_{\rm est}^{\alpha_1}$, and the dashed green line shows a constant linear regression $I_m = I_{\rm est} + C_2$.

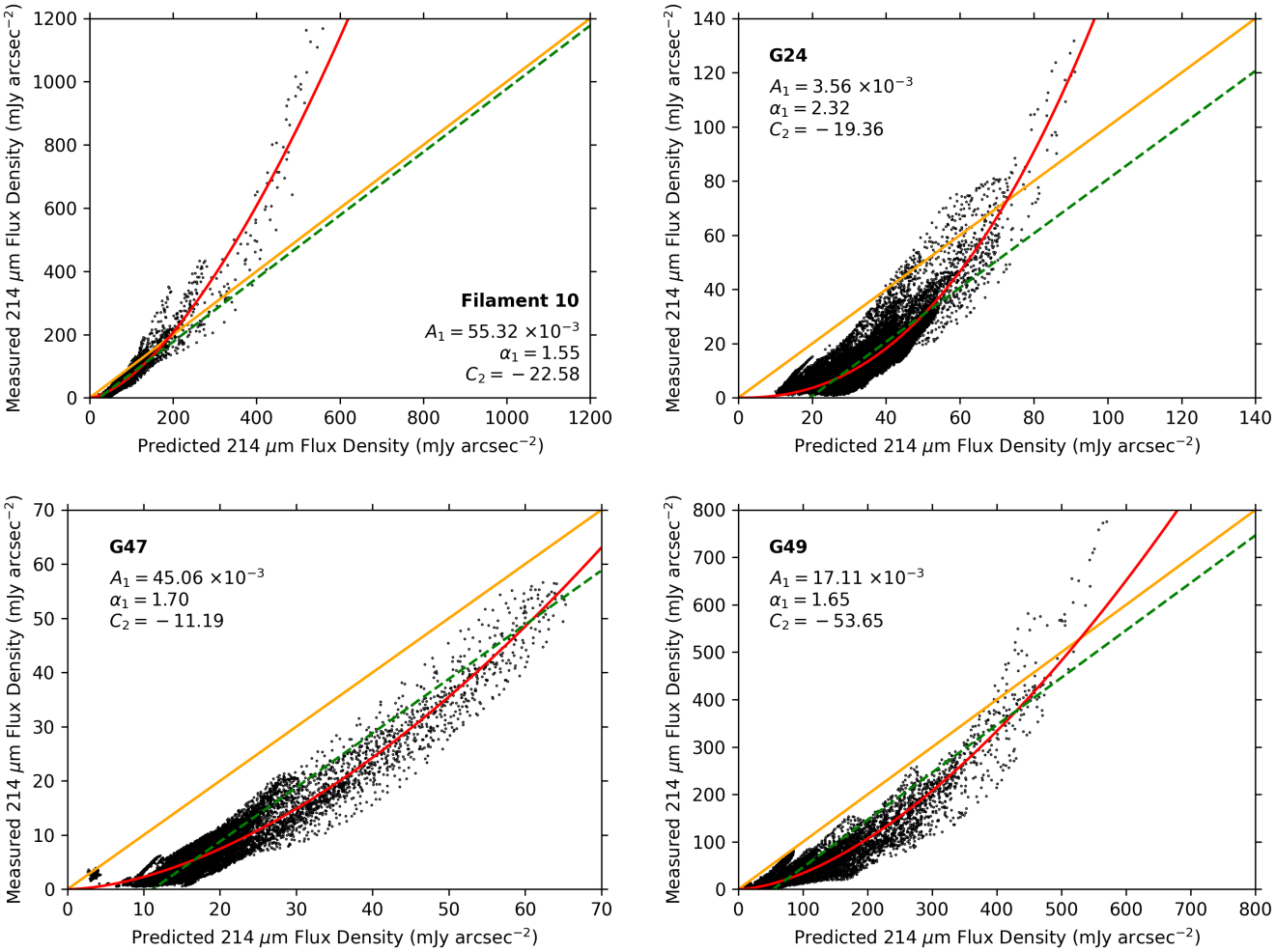

Figure 22. Comparison between the measured and predicted flux densities at 214 μm for each FIELDMAPS bone. Continued from Figure 21. The measured flux densities are taken from the HAWC+ Stokes I total intensity maps shown in the bottom panels of Figures 2–11. The predicted flux densities are calculated from Equation (F1) using the Herschel-derived maps of hydrogen column density N_{H_2} and dust temperature T_d. The full orange line shows a 1:1 relation between the predicted I_{est} and measured I_m flux densities, the full red line shows a power-law fit of the form $I_m = A_1\, I_{est}^{\alpha_1}$, and the dashed green line shows a constant linear regression $I_m = I_{est} + C_2$.

$B_\nu(T_d)$ is Planck's law for a blackbody for a dust temperature T_d. In the far-infrared, the dust opacity κ_ν can be expressed as a power law (R. H. Hildebrand 1983):

$$\kappa_\nu = \kappa_0 \left(\frac{\nu}{\nu_0}\right)^\beta, \tag{F2}$$

where κ_0 is the opacity at the reference frequency ν_0, and β is the spectral index of the emissivity. The relation between the column densities of the dust N_d (in g cm^{-2}) and the molecular hydrogen N_{H_2} (in cm^{-2}) is given by

$$N_d = \frac{\mu\, m_H\, N_{H_2}}{R_{g/d}}, \tag{F3}$$

where μ is the mean molecular weight of the gas, m_H is the mass of the hydrogen atom, and $R_{g/d}$ is the gas-to-dust ratio. For this work, we use the same parameters as Appendix B of K. Wang et al. (2015), which are a mean molecular weight μ of 2.8 (J. Kauffmann et al. 2008), a gas-to-dust ratio $R_{g/d}$ of 100, a reference dust opacity κ_0 of 4.0 cm^2 g^{-1} at a frequency ν_0 of 505 GHz, and a spectral index of the emissivity β of 1.75.

For each bone, using Equations (F1)–(F3), we create a map of predicted flux densities at 214 μm from the Herschel-derived maps of the hydrogen column density N_{H_2} and dust temperature T_d. These maps are regridded using the REPROJECT Python package to match the Stokes I maps of the HAWC+ observations. Figures 21 and 22 show the comparison between the HAWC+-measured and Herschel-predicted flux densities at 214 μm for each pixel with a detection of polarization (i.e., $I/\delta_I > 10$, $P/\delta_P > 3$, and $P < 30\%$). The pixels that pass the selection criteria for polarization are the most relevant in the context of this work, but they may not fully cover the range of differences between SOFIA and Herschel flux measurements.

In each panel of Figures 21 and 22, we plot three relations between the measured and predicted flux densities. First, we show the 1:1 relation for reference, a power-law fit, and a linear relation assuming a constant offset between the two sets of data. Overall, we find that the predicted Herschel flux densities tend to be larger than those measured with HAWC+

at lower values, as expected for a difference in the background levels. However, a constant flux offset is insufficient to fully describe the differences between the data, as the flux densities are closer together at higher levels. In some cases, the flux densities measured with HAWC+ are even significantly larger than those predicted from the Herschel data. This behavior could be explained by the dilution of sources with high fluxes by the larger Herschel beam (36.″4, see Section 2.2), or by the inaccuracy of fitting the dust thermal emission using the properties of a single dust population and a fixed spectral index β. Additionally, while a power law can reproduce the relation between SOFIA and Herschel at higher flux densities, there is significant variation in the measured spectral indices α_1, which means that such a simple relation is also insufficient to systematically describe the discrepancies between the two observatories.

Appendix G
Debiasing HAWC+ Data

In Section 3.2, we note the need to debias the polarized intensity I_p. The polarized intensity I_p follows a Rice distribution that has a positive bias, which is more significant when the signal-to-noise ratio is low (K. Serkowski 1958; J. F. C. Wardle & P. P. Kronberg 1974; K. Pattle et al. 2019). From Equation (3), we therefore expressed the debiased polarized intensity I'_P as

$$I'_p = \sqrt{I_p^2 - \delta_{I_p}^2} = \sqrt{Q^2 + U^2 - \delta_{I_p}^2}, \tag{G1}$$

with the uncertainty δ_{I_p}:

$$\delta_{I_p} = \sqrt{\frac{(Q\ \delta_Q)^2 + (U\ \delta_U)^2}{Q^2 + U^2}}, \tag{G2}$$

where δ_Q and δ_U are the uncertainties for Stokes Q and U, respectively, and assuming a propagation of noncorrelated errors.

However, an alternative approach is given by M. S. Gordon et al. (2018) and M. Clarke et al. (2022) for debiasing HAWC + data. Specifically, using the notation from M. S. Gordon et al. (2018), the biased percent polarization p is given by

$$p = 100\% \sqrt{\left(\frac{Q}{I}\right)^2 + \left(\frac{U}{I}\right)^2}, \tag{G3}$$

with the uncertainty δ_p:

$$\begin{aligned}\delta_p &= \frac{100\%}{I} \sqrt{\left[\frac{(Q\ \delta_Q)^2 + (U\ \delta_U)^2}{Q^2 + U^2}\right] + \left[\left(\frac{Q}{I}\right)^2 + \left(\frac{U}{I}\right)^2\right]\delta_I^2} \\ &= 100\% \frac{I_p}{I} \sqrt{\left(\frac{\delta_{I_p}}{I_p}\right)^2 + \left(\frac{\delta_I}{I}\right)^2},\end{aligned} \tag{G4}$$

with δ_I being the uncertainty on Stokes I, and assuming the cross-terms δ_{QU}, δ_{QI}, and δ_{UI} are negligible. The debiased percent polarization p' is then

$$p' = \sqrt{p^2 - \delta_p^2}, \tag{G5}$$

and, following the notation from M. S. Gordon et al. (2018), the resulting debiased polarized intensity $I_{p'}$ is

$$I_{p'} = \frac{p'\, I}{100\%}, \tag{G6}$$

which is not identical to Equation (G1), due in part to the presence of the signal-to-noise ratio δ_I/I for the total intensity in Equations (G4) and (G5).

The extensions of the FITS files produced directly by the HAWC+ pipeline follow the debiasing from Equations (G5) and (G6), while the data products for FIELDMAPS follow the debiasing from Equation (G1). We argue here that both methods are essentially equivalent for the polarization detection thresholds used for this work: $p/\delta_p > 3$, $I/\delta_I > 10$, and $p < 30\%$.

First, the polarization fraction p for dust thermal emission in the Galaxy is generally expected to be below 30%, with Planck finding a maximum $p_{\max}$ of $22.5^{+3.5}_{-1.5}\%$ (Planck Collaboration et al. 2020c), and thus $I_p \leqslant 0.3\, I$. Furthermore, due to how Stokes I, Q, and U are measured (M. Clarke et al. 2022), the uncertainties δ_Q and δ_U tend to be slightly larger than δ_I (see Table 3), which following Equation (G2) leads to $\delta_{I_p} \geqslant \delta_I$. The δ_{I_p}/I_p relation can then be approximated by

$$\frac{\delta_{I_p}}{I_p} \geqslant \frac{\delta_I}{0.3\, I}. \tag{G7}$$

In this example, if we use the lower limit of 10 for I/δ_I, then we find $I_p/\delta_{I_p} \leqslant 3$. When squared, the inverse ratio of these quantities gives

$$\left(\frac{\delta_I}{I}\right)^2 \left(\frac{\delta_{I_p}}{I_p}\right)^{-2} \leqslant 0.09. \tag{G8}$$

In this extreme example, we find that $(\delta_{I_p}/I_p)^2$ is at least 10 times larger than $(\delta_I/I)^2$. However, more generally, lower values of p and a higher signal-to-noise I/δ_I will exacerbate this difference, and so, we can confidently write

$$\left(\frac{\delta_{I_p}}{I_p}\right)^2 \gg \left(\frac{\delta_I}{I}\right)^2. \tag{G9}$$

Using Equation (G9), we can now simplify Equation (G4) to become

$$\delta_p \approx 100\% \frac{I_p}{I} \sqrt{\left(\frac{\delta_{I_p}}{I_p}\right)^2} = 100\% \frac{\delta_{I_p}}{I}, \tag{G10}$$

which when substituted in Equation (G5) leads to

$$p' = \frac{100\%}{I} \sqrt{I_p^2 - \delta_{I_p}^2} = 100\% \frac{I'_p}{I} = P, \tag{G11}$$

where P is the debiased polarization fraction defined in Equation (4). Through the approximation given in Equation (G9), we have recovered both the debiased polarized intensity from Equations (3) and (G1), but also an equation of the same form as the relation between p' and $I_{p'}$ from Equation (G6). We therefore conclude that, at least for the signal-to-noise thresholds used in this work, both debiasing methods are nearly indistinguishable.

Appendix H
Angle Dispersion in G49

Figure 23 provides the four histograms used to calculate the circular means and standard deviations given in Table 4 of Section 3.4 for four regions in G49. These regions are 91″ by

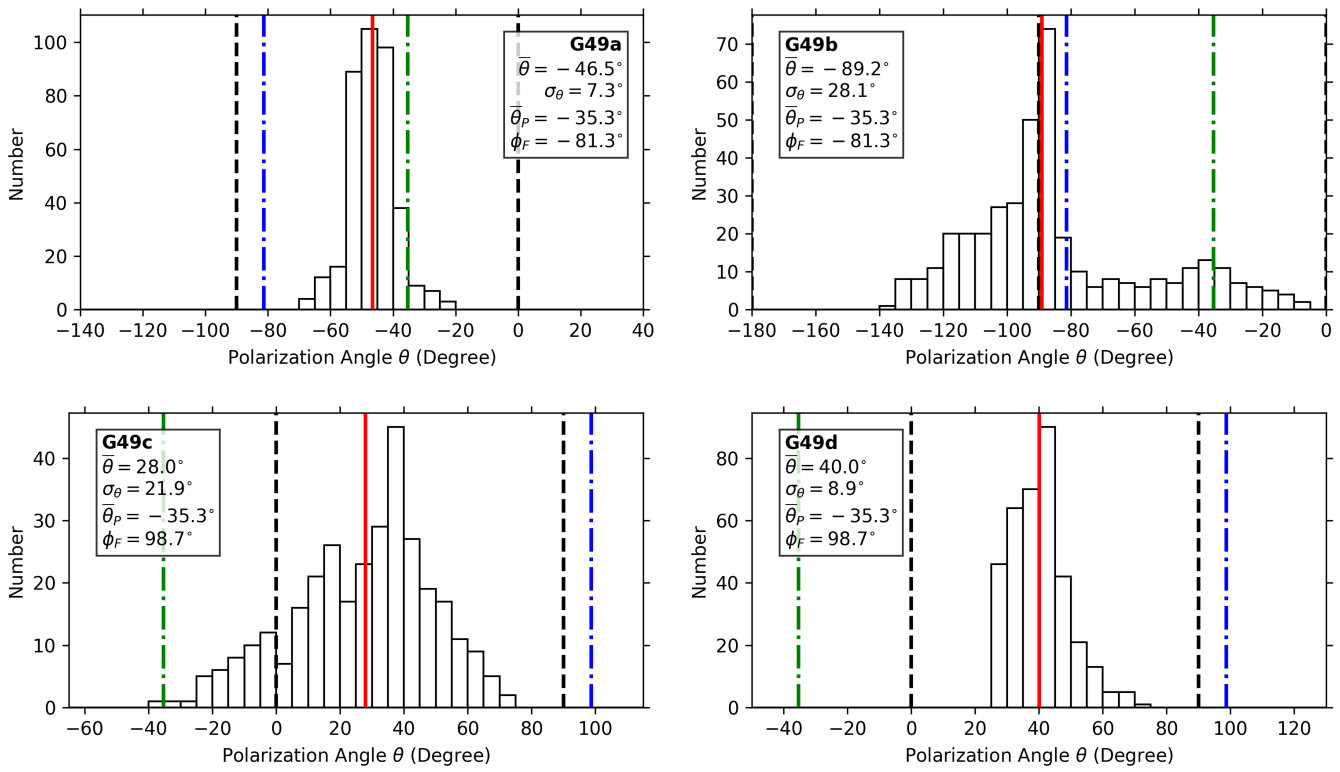

Figure 23. Histograms of polarization angles θ for the four regions of G49 listed in Table 4. All angles are provided relative to Galactic north. The bin size of the histograms is 5°. The full red line is the circular mean $\overline{\theta}$ of the distribution, the green dashed–dotted line is the circular mean of the Planck polarization angles $\overline{\theta}_P$, and the blue dashed–dotted line is the fitted orientation ϕ_F of the filament (see Section 3.4). Each histogram is centered on the bin containing the circular mean $\overline{\theta}$. Black dashed lines indicate angles of −90°, 0°, and 90° for clarity. The measured circular standard deviation σ_θ for each cloud is also given within the insets. The inferred magnetic field orientation θ_B is obtained from rotating the polarization angle θ by 90°.

91″ boxes positioned on the four brightest peaks in G49 at 214 μm, as displayed in the top panel of Figure 11. The histograms follow the same format as those shown in Figures 12 and 13.

Appendix I
Additional Figures

Additional figures for each bone can be found in the online repository for the FIELDMAPS survey. While we could not include all these figures in the paper, we present in this appendix those created for Filament 10 as an example of their contents. Figure 24 shows the polarization vectors from the bottom panel of Figure 8, but plotted on the Herschel-derived map of dust temperatures T_d instead. In a similar manner to Figure 17, Figure 25 shows the relations between the polarization fraction P and the gas column density $N_{\rm H_2}$, and between the polarization fraction P and the dust temperature T_d, for Filament 10. In each case, the HAWC+ data were smoothed and reprojected to the resolution and pixel scale of the column density and dust temperature maps. Alternative figures using the same nonsmoothed vector catalogs as Figures 16 and 17 are also available on Dataverse. A power law of the form $P \propto N_{\rm H_2}^{\gamma}$ if fitted for the column density. Figure 26 displays the result of the FILFINDER algorithm for Filament 10, as well as the linear fit described in Section 3.4.1 for the filament orientation ϕ_F. In Figure 27, we compare the effect of using HAWC+ and Herschel flux densities (see Appendix F) for the relation between the polarization fraction P and the Stokes I total intensity. The left panel of Figure 27 is a reproduction of the panel for Filament 10 in Figure 17. In each case, we fit a power law of the form $P = A\, I^{\alpha}$, as described in Section 3.5.

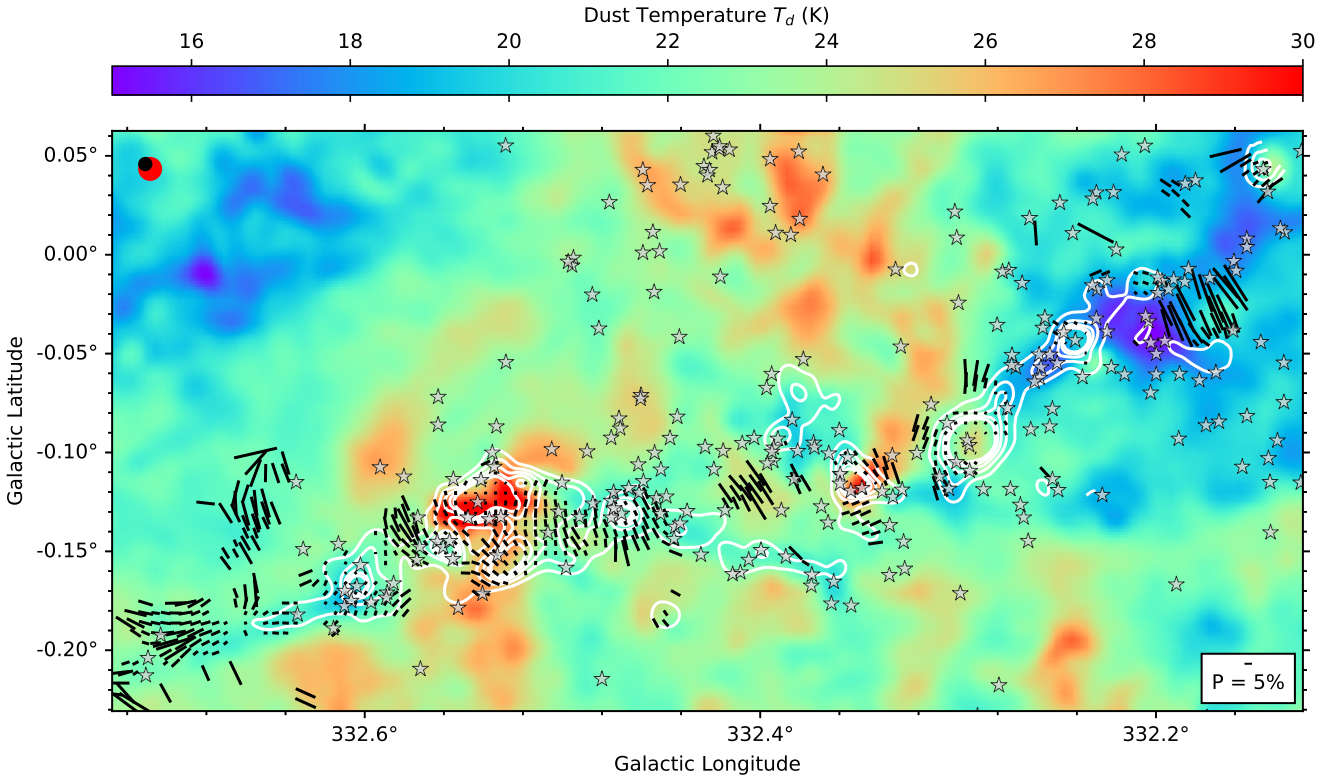

Figure 24. The polarization vectors (black) plotted on a color map of dust temperatures T_d for Filament 10. The vector length shows the polarization fraction P, and only every fourth vector is plotted. The white contours trace reference levels of the Stokes I total intensity. Known YSOs are identified with star symbols. The circles denote the beam sizes of HAWC+ (black) and Herschel (red).

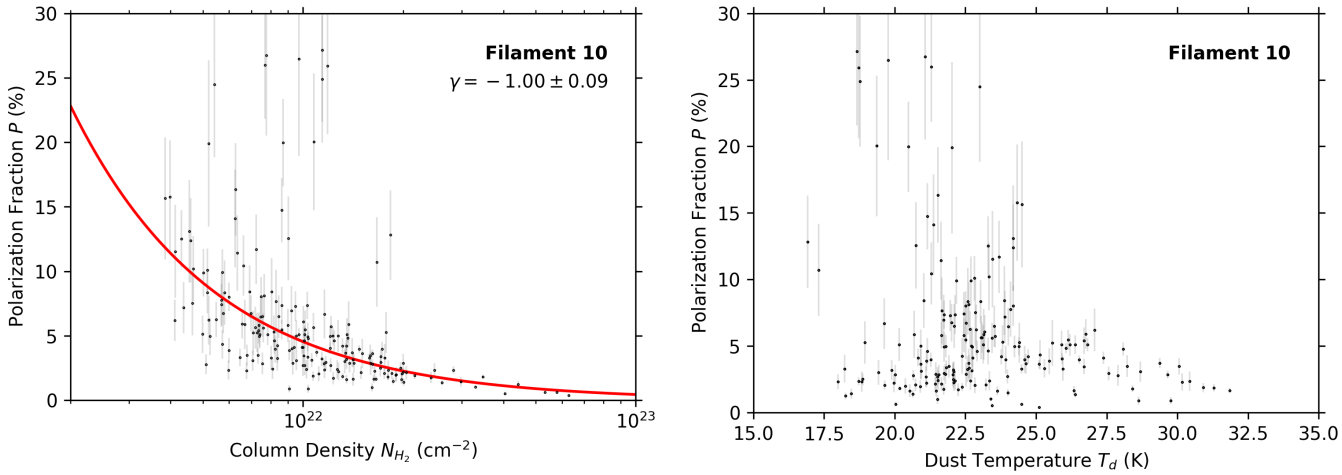

Figure 25. Polarization fraction P as a function of the gas column density N_{H_2} (left panel) and the dust temperature T_d (right panel) for Filament 10. The full red line traces a power-law fit of the form $P \propto N_{H_2}^{\gamma}$. The HAWC+ data was smoothed and reprojected to share the same resolution and pixel scale as the Herschel column density and temperature maps described in Section 2.2. Only every other vector from the resulting smoothed catalog is plotted and used for the fit, and the uncertainty in P is shown as gray lines.

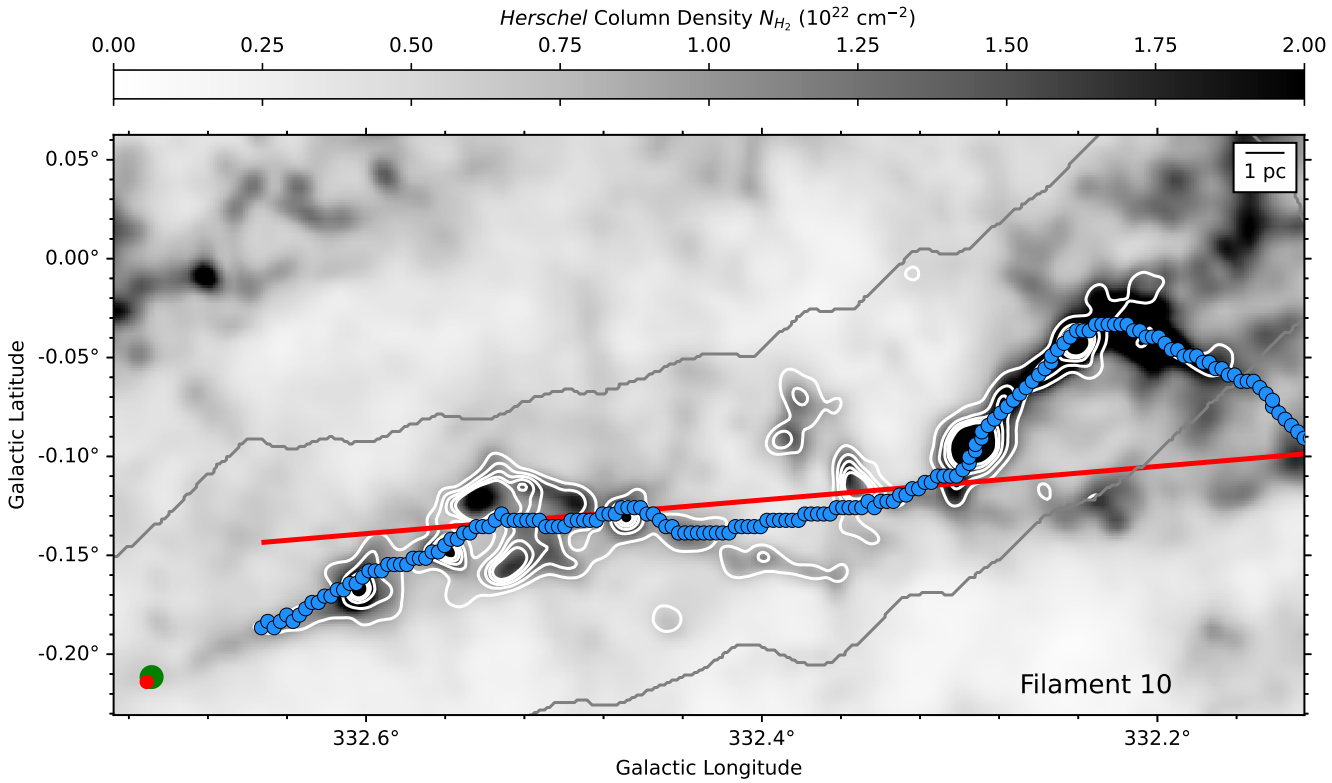

Figure 26. Filament orientation for Filament 10. The blue circles show the result from the FILFINDER algorithm for the spine of the filament. The red line is the linear regression used to calculate the filament orientation ϕ_F.

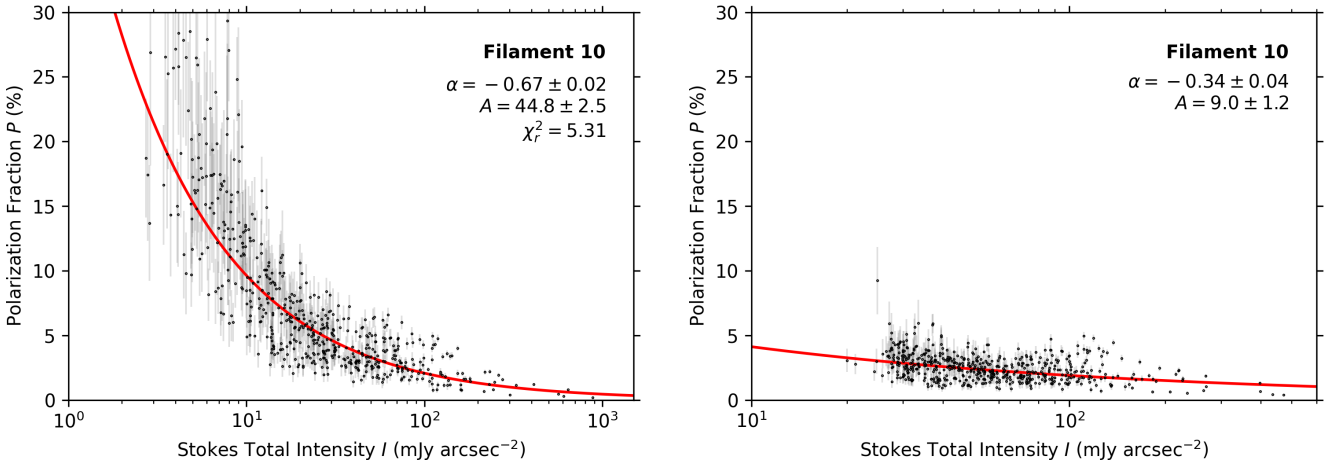

Figure 27. Polarization fraction P as a function of the Stokes I total intensity for Filament 10. The left panel shows the same relation as in Figure 17 as reference, while the right panel substitutes the Stokes I total intensity by the Herschel-derived flux densities at 214 μm from Appendix F. In each panel, the data is fitted with a power law of the form $P = A\, I^{\alpha}$. Only every fourth vector is plotted and used for the fit, and the uncertainty in P is shown as gray lines.

Appendix J
Spitzer Images

As noted in Section 3.1, we have created composite red (24 μm), green (8.0 μm), and blue (3.6 μm) images of the FIELDMAPS targets from data obtained by the GLIMPSE (R. A. Benjamin et al. 2003) and MIPSGAL (S. J. Carey et al. 2009) surveys with Spitzer. Figures 28–32 present the resulting images for all the FIELDMAPS bones for the regions displayed in Figures 2–11, except for Filament 4, which is already shown in Figure 1. Each figure identifies the positions of Class I, II, III, and flat-spectrum YSOs, as well as masers when available. Contours show Herschel-derived $N_{\rm H_2}$ column densities to more easily identify the denser regions of the filaments. As in Figure 1, the color levels were chosen to highlight the infrared-dark features of the bones. However, this process was complicated by the fact that some bones are saturated in the Spitzer bands, with G24 being the most extreme example. Reference lengths of 1 pc are also provided for each bone using the distances listed in Table 2. These composite images illustrate the wide range of star-forming conditions covered by the FIELDMAPS bones.

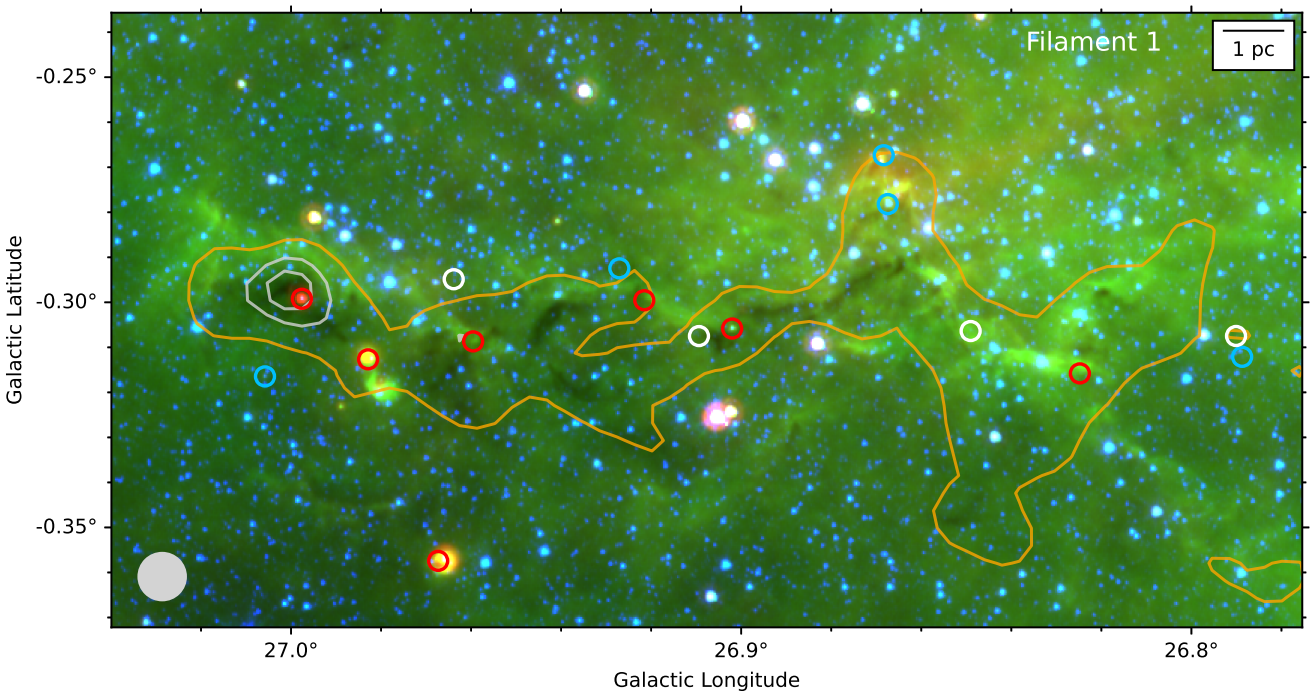

Figure 28. Spitzer red (24 μm), green (8.0 μm), and blue (3.6 μm) composite image for Filament 1. The color levels were chosen to highlight infrared-dark features. Class I and flat-spectrum (red), Class II (blue), and Class III (white) YSOs from the literature are identified with circles. The three contours trace Herschel-derived N_{H_2} column densities of 0.5, 1.0, and 1.5 $\times$ 10^{22} cm^{-2}, with the lowest level identified in orange for clarity. The Herschel beam is given by the gray circle at the bottom left.

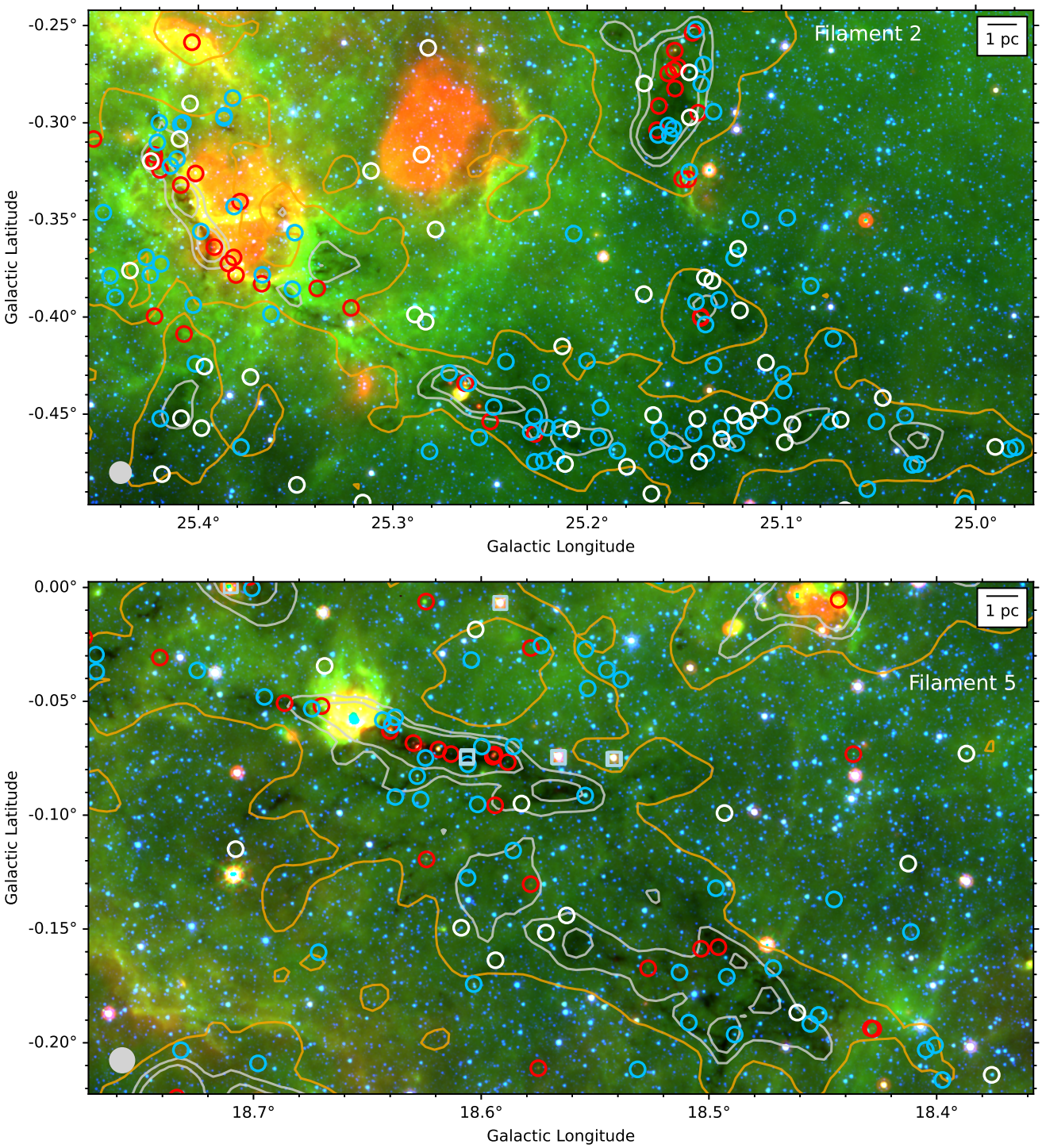

Figure 29. Spitzer red (24 μm), green (8.0 μm), and blue (3.6 μm) composite image for Filament 2 (top) and Filament 5 (bottom). The color levels were chosen to highlight infrared-dark features. Class I (green), flat-spectrum (violet), Class II (blue), and Class III (red) YSOs from the literature are identified with star symbols. Masers are identified with squares when available. The three contours trace Herschel-derived N_{H_2} column densities of 0.5, 1.0, and 1.5 $\times$ 10^{22} cm^{-2}, with the lowest level identified in orange for clarity. The Herschel beam is given by the gray circle at the bottom left.

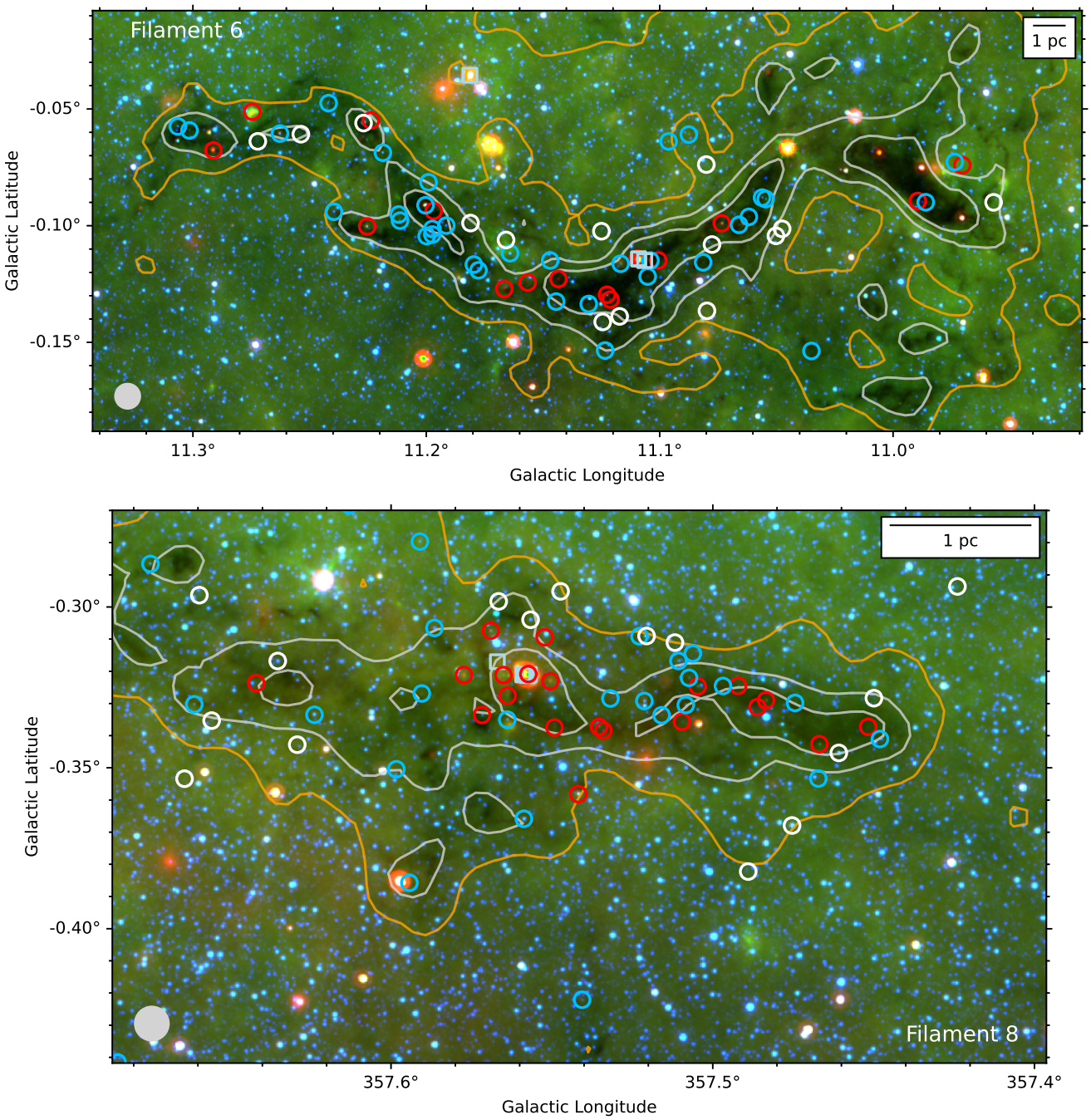

Figure 30. Spitzer red (24 μm), green (8.0 μm), and blue (3.6 μm) composite image for Filament 6 (top) and Filament 8 (bottom). The color levels were chosen to highlight infrared-dark features. Class I and flat-spectrum (red), Class II (blue), and Class III (white) YSOs from the literature are identified with circles. Masers are identified with squares when available. The three contours trace Herschel-derived N_{H_2} column densities of 0.5, 1.0, and 2.0 $\times$ 10^{22} cm^{-2}, with the lowest level identified in orange for clarity. The Herschel beam is given by the gray circle at the bottom left.

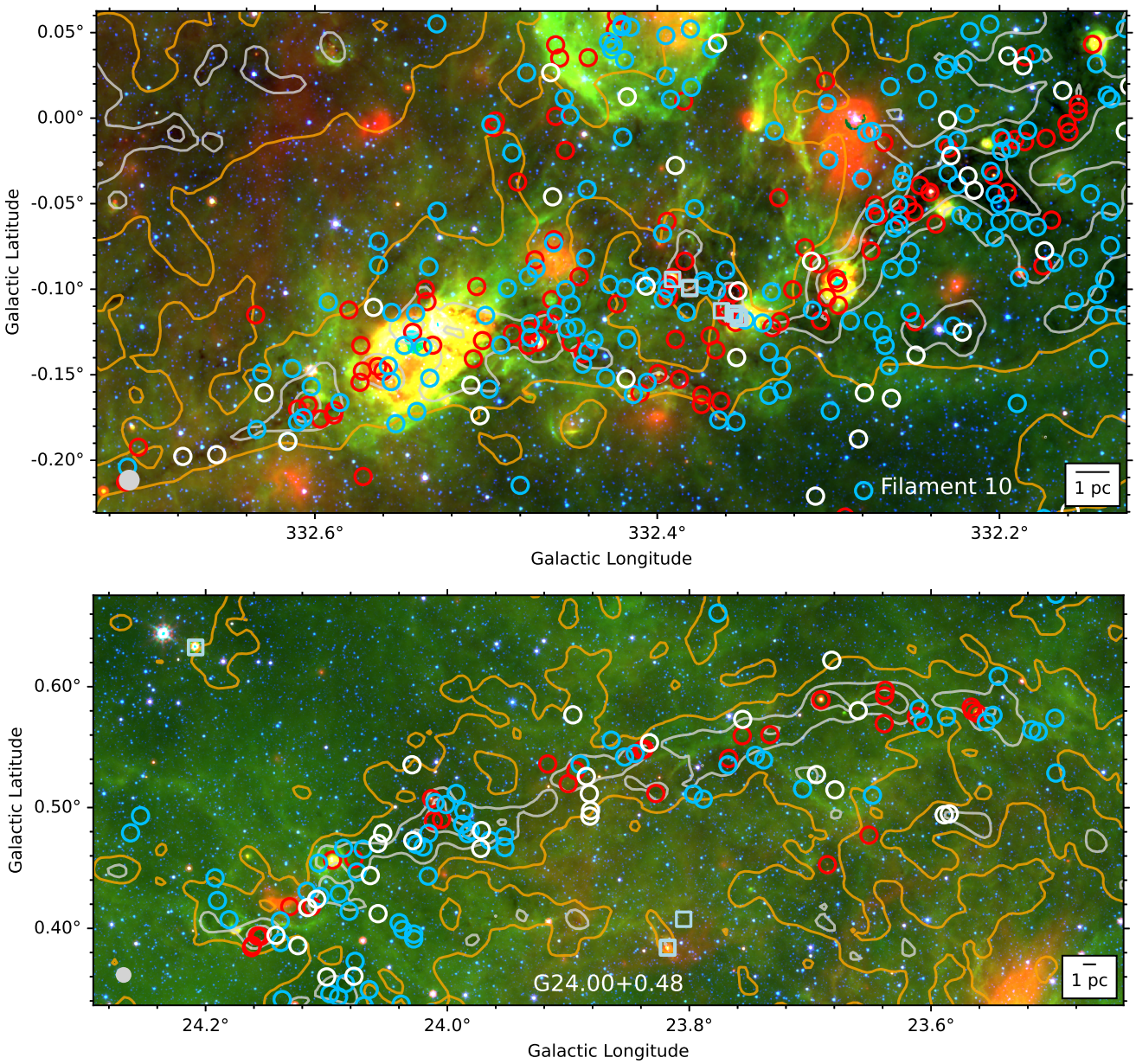

Figure 31. Spitzer red (24 μm), green (8.0 μm), and blue (3.6 μm) composite image for Filament 10 (top) and G24 (bottom). The color levels were chosen to highlight infrared-dark features. Class I (green), flat-spectrum (violet), Class II (blue), and Class III (red) YSOs from the literature are identified with star symbols. Masers are identified with squares when available. The three contours trace Herschel-derived N_{H_2} column densities of 0.5, 1.0, and 2.0 $\times$ 10^{22} cm^{-2}, with the lowest level identified in orange for clarity. The Herschel beam is given by the gray circle at the bottom left.

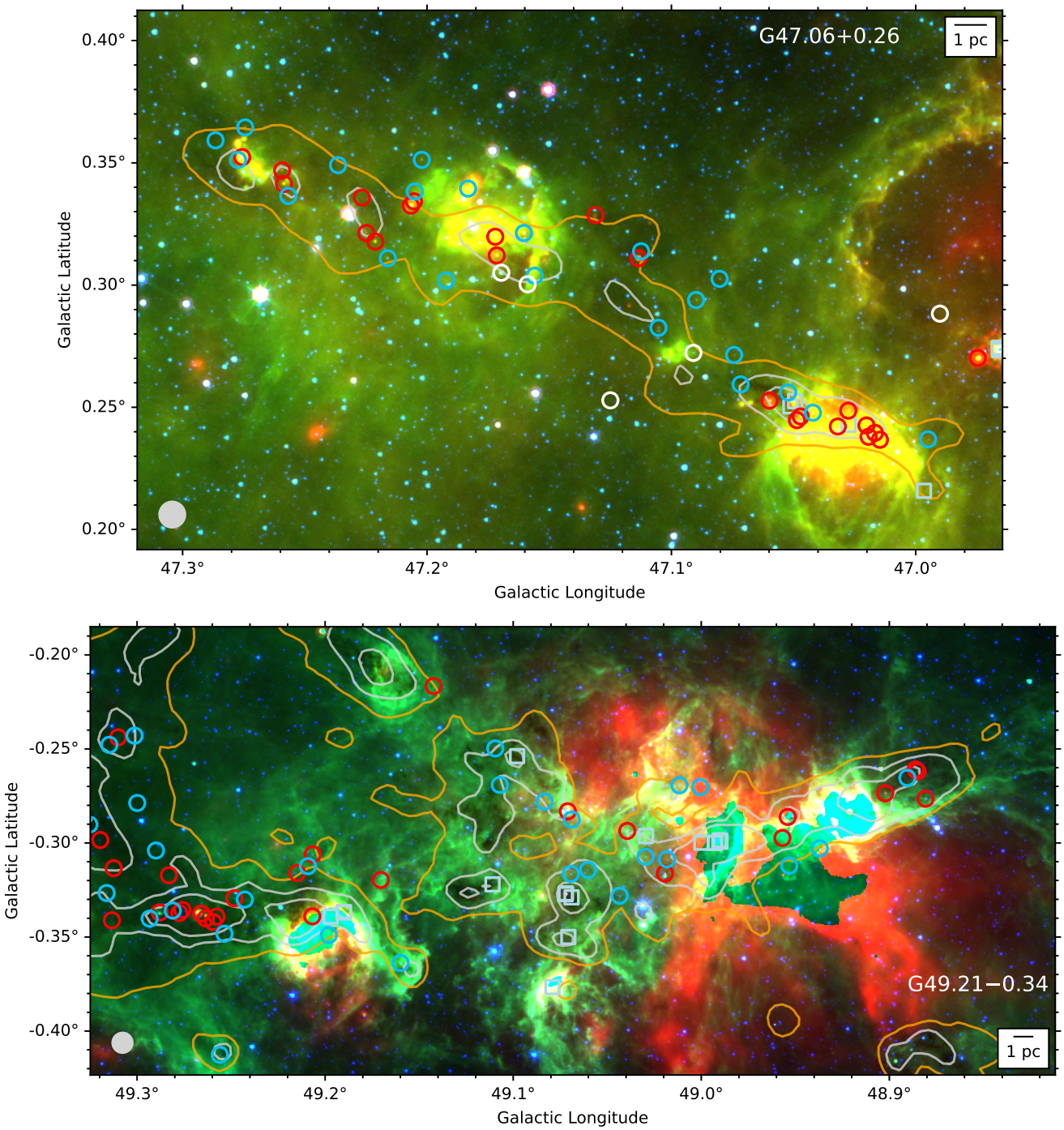

Figure 32. Spitzer red (24 μm), green (8.0 μm), and blue (3.6 μm) composite image for G47 (top) and G49 (bottom). The color levels were chosen to highlight infrared-dark features, but we note that G49 is heavily saturated in these Spitzer bands. Class I and flat-spectrum (red), Class II (blue), and Class III (white) YSOs from the literature are identified with circles. Masers are identified with squares when available. The three contours trace Herschel-derived N_{H_2} column densities of 0.5, 1.0, and 2.0 $\times$ 10^{22} cm^{-2}, with the lowest level identified in orange for clarity. The Herschel beam is given by the gray circle at the bottom left.

ORCID iDs

Simon Coudé https://orcid.org/0000-0002-0859-0805
Ian W. Stephens https://orcid.org/0000-0003-3017-4418
Philip C. Myers https://orcid.org/0000-0002-2885-1806
Nicole Karnath https://orcid.org/0000-0003-3682-854X
Andrés E. Guzmán https://orcid.org/0000-0003-0990-8990
Catherine Zucker https://orcid.org/0000-0002-2250-730X
B.-G. Andersson https://orcid.org/0000-0001-6717-0686
Zhi-Yun Li https://orcid.org/0000-0002-7402-6487
Leslie W. Looney https://orcid.org/0000-0002-4540-6587
Giles Novak https://orcid.org/0000-0003-1288-2656
Thushara G. S. Pillai https://orcid.org/0000-0003-2133-4862
Sarah I. Sadavoy https://orcid.org/0000-0001-7474-6874
Patricio Sanhueza https://orcid.org/0000-0002-7125-7685
Archana Soam https://orcid.org/0000-0002-6386-2906

References

Abreu-Vicente, J., Ragan, S., Kainulainen, J., et al. 2016, A&A, 590, A131
Alves, F. O., Frau, P., Girart, J. M., et al. 2014, A&A, 569, L1
Andersson, B. G., Karoly, J., Bastien, P., et al. 2024, ApJ, 963, 76
Andersson, B. G., Lazarian, A., & Vaillancourt, J. E. 2015, ARA&A, 53, 501
André, P., Di Francesco, J., Ward-Thompson, D., et al. 2014, in Protostars and Planets VI, ed. H. Beuther et al. (Tucson, AZ: Univ. Arizona Press), 27
Aniano, G., Draine, B. T., Gordon, K. D., & Sandstrom, K. 2011, PASP, 123, 1218
Appenzeller, I. 1968, ApJ, 151, 907
Arzoumanian, D., Furuya, R. S., Hasegawa, T., et al. 2021, A&A, 647, A78
Astropy Collaboration, Price-Whelan, A. M., Lim, P. L., et al. 2022, ApJ, 935, 167
Astropy Collaboration, Price-Whelan, A. M., Sipőcz, B. M., et al. 2018, AJ, 156, 123
Astropy Collaboration, Robitaille, T. P., Tollerud, E. J., et al. 2013, A&A, 558, A33
Beck, R. 2015, A&ARv, 24, 4
Benjamin, R. A., Churchwell, E., Babler, B. L., et al. 2003, PASP, 115, 953
Bennett, M., & Bovy, J. 2019, MNRAS, 482, 1417
Bešlić, I., Coudé, S., Lis, D. C., et al. 2024, A&A, 684, A212
Bethell, T. J., Chepurnov, A., Lazarian, A., & Kim, J. 2007, ApJ, 663, 1055
Beuther, H., Walsh, A., Wang, Y., et al. 2019, A&A, 628, A90
Borlaff, A. S., Lopez-Rodriguez, E., Beck, R., et al. 2021, ApJ, 921, 128
Borlaff, A. S., Lopez-Rodriguez, E., Beck, R., et al. 2023, ApJ, 952, 4
Bradley, L., Sipőcz, B., Robitaille, T., et al. 2024, astropy/photutils: v1.13.0, Zenodo, doi:10.5281/zenodo.12585239
Butterfield, N. O., Chuss, D. T., Guerra, J. A., et al. 2024a, ApJ, 963, 130
Butterfield, N. O., Guerra, J. A., Chuss, D. T., et al. 2024b, ApJ, 968, 63
Carey, S. J., Clark, F. O., Egan, M. P., et al. 1998, ApJ, 508, 721
Carey, S. J., Feldman, P. A., Redman, R. O., et al. 2000, ApJL, 543, L157
Carey, S. J., Noriega-Crespo, A., Mizuno, D. R., et al. 2009, PASP, 121, 76
Chan, S. J., Henning, T., & Schreyer, K. 1996, A&AS, 115, 285
Chandrasekhar, S., & Fermi, E. 1953, ApJ, 118, 113
Chapman, N. L., Goldsmith, P. F., Pineda, J. L., et al. 2011, ApJ, 741, 21
Ciesla, L., Dowell, C. D., Sauvage, M., et al. 2025, JATIS, 11, 031625
Clarke, M., Perera, D., Berthoud, M., et al. 2022, HAWC+ DRP User's Manual SOF-US-HBK-OP10-2008 Rev. L, https://irsa.ipac.caltech.edu/data/SOFIA/docs/sites/default/files/2022-12/hawc_users_revL.pdf
Clarke, M., & Vliet, R. V. 2023, SOFIA-USRA/sofia_redux: v1.3.2, Zenodo, doi:10.5281/zenodo.7783303
Comrie, A., Wang, K.-S., Hsu, S.-C., et al. 2021, CARTA: The Cube Analysis and Rendering Tool for Astronomy, v2.0.0, Zenodo, doi:10.5281/zenodo.4905459
Coudé, S., Bastien, P., Houde, M., et al. 2019, ApJ, 877, 88
Crutcher, R. M., Nutter, D. J., Ward-Thompson, D., & Kirk, J. M. 2004, ApJ, 600, 279
Dame, T. M., Hartmann, D., & Thaddeus, P. 2001, ApJ, 547, 792
Davis, L. 1951, PhRv, 81, 890
Doi, Y., Hasegawa, T., Bastien, P., et al. 2021a, ApJ, 914, 122
Doi, Y., Hasegawa, T., Furuya, R. S., et al. 2020, ApJ, 899, 28
Doi, Y., Nakamura, K., Kawabata, K. S., et al. 2024, ApJ, 961, 13
Doi, Y., Tomisaka, K., Hasegawa, T., et al. 2021b, ApJL, 923, L9
Dotson, J. L. 1996, ApJ, 470, 566
Dowell, C. D., Cook, B. T., Harper, D. A., et al. 2010, Proc. SPIE, 7735, 77356H
Dowell, C. D., Hensley, B. S., & Sauvage, M. 2025, JATIS, 11, 031624
Egan, M. P., Shipman, R. F., Price, S. D., et al. 1998, ApJL, 494, L199
Fanciullo, L., Kemper, F., Pattle, K., et al. 2022, MNRAS, 512, 1985
Fazio, G. G., Hora, J. L., Allen, L. E., et al. 2004, ApJS, 154, 10
Girart, J. M., Rao, R., & Marrone, D. P. 2006, Sci, 313, 812
Glenn, J., Meixner, M., Bradford, C. M., et al. 2025, JATIS, 11, 031628
Goodman, A. A., Alves, J., Beaumont, C. N., et al. 2014, ApJ, 797, 53
Goodman, A. A., Bastien, P., Myers, P. C., & Menard, F. 1990, ApJ, 359, 363
Gordon, M. S., Lopez-Rodriguez, E., Andersson, B. G., et al. 2018, arXiv:1811.03100
Górski, K. M., Hivon, E., Banday, A. J., et al. 2005, ApJ, 622, 759
GRAVITY Collaboration, Abuter, R., Amorim, A., et al. 2019, A&A, 625, L10
GRAVITY Collaboration, Abuter, R., Amorim, A., et al. 2021, A&A, 647, A59
Guzmán, A. E., Sanhueza, P., Contreras, Y., et al. 2015, ApJ, 815, 130
Hamaker, J. P., & Bregman, J. D. 1996, A&AS, 117, 161
Harper, D. A., Runyan, M. C., Dowell, C. D., et al. 2018, JAI, 7, 1840008
Hennebelle, P., Pérault, M., Teyssier, D., & Ganesh, S. 2001, A&A, 365, 598
Henning, T., Linz, H., Krause, O., et al. 2010, A&A, 518, L95
Hildebrand, R. H. 1983, QJRAS, 24, 267
Hildebrand, R. H., Davidson, J. A., Dotson, J. L., et al. 2000, PASP, 112, 1215
Hix, R., He, C.-C., & Ricotti, M. 2023, MNRAS, 522, 6203
Hoang, T., & Lazarian, A. 2008, MNRAS, 388, 117
Hoang, T., Tram, L. N., Lee, H., & Ahn, S.-H. 2019, NatAs, 3, 766
Houde, M., Vaillancourt, J. E., Hildebrand, R. H., Chitsazzadeh, S., & Kirby, L. 2009, ApJ, 706, 1504
Hull, C. L. H., Plambeck, R. L., Kwon, W., et al. 2014, ApJS, 213, 13
Jackson, J. M., Finn, S. C., Chambers, E. T., Rathborne, J. M., & Simon, R. 2010, ApJL, 719, L185
Johnstone, D., Fiege, J. D., Redman, R. O., Feldman, P. A., & Carey, S. J. 2003, ApJL, 588, L37
Jones, T. J., Bagley, M., Krejny, M., Andersson, B. G., & Bastien, P. 2015, AJ, 149, 31
Jones, T. J., Kim, J.-A., Dowell, C. D., et al. 2020, AJ, 160, 167
Kaminsky, A., Bonne, L., Arzoumanian, D., & Coudé, S. 2023, ApJ, 948, 109
Kauffmann, J., Bertoldi, F., Bourke, T. L., Evans, N. J., II, & Lee, C. W. 2008, A&A, 487, 993
Koch, E. W., & Rosolowsky, E. W. 2015, MNRAS, 452, 3435
Kovács, A. 2008a, Proc. SPIE, 7020, 70201S
Kovács, A. 2008b, Proc. SPIE, 7020, 702007
Kwon, J., Doi, Y., Tamura, M., et al. 2018, ApJ, 859, 4
Lawrence, A., Warren, S. J., Almaini, O., et al. 2007, MNRAS, 379, 1599
Lazarian, A., & Hoang, T. 2007, MNRAS, 378, 910
Lee, D., Berthoud, M., Chen, C.-Y., et al. 2021, ApJ, 918, 39
Li, J. J., Immer, K., Reid, M. J., et al. 2022, ApJS, 262, 42
Liu, H. B., Qiu, K., Zhang, Q., Girart, J. M., & Ho, P. T. P. 2013, ApJ, 771, 71
Lopez-Rodriguez, E., Beck, R., Clark, S. E., et al. 2021, ApJ, 923, 150
Lopez-Rodriguez, E., Borlaff, A. S., Beck, R., et al. 2023, ApJL, 942, L13
Lopez-Rodriguez, E., Clarke, M., Shenoy, S., et al. 2022a, ApJ, 936, 65
Lopez-Rodriguez, E., Mao, S. A., Beck, R., et al. 2022b, ApJ, 936, 92
Lumsden, S. L., Hoare, M. G., Urquhart, J. S., et al. 2013, ApJS, 208, 11
Martin-Alvarez, S., Lopez-Rodriguez, E., Dacunha, T., et al. 2024, ApJ, 966, 43
Mathis, J. S., Rumpl, W., & Nordsieck, K. H. 1977, ApJ, 217, 425
Matthews, B. C., Fiege, J. D., & Moriarty-Schieven, G. 2002, ApJ, 569, 304
Michail, J. M., Ashton, P. C., Berthoud, M. G., et al. 2021, ApJ, 907, 46
Minniti, D., Lucas, P. W., Emerson, J. P., et al. 2010, NewA, 15, 433
Molinari, S., Swinyard, B., Bally, J., et al. 2010, PASP, 122, 314
Monsch, K., Pineda, J. E., Liu, H. B., et al. 2018, ApJ, 861, 77
Montier, L., Plaszczynski, S., Levrier, F., et al. 2015, A&A, 574, A136
Morii, K., Sanhueza, P., Nakamura, F., et al. 2023, ApJ, 950, 148
Moullet, A., Kataria, T., Lis, D., et al. 2023, arXiv:2310.20572
Naghizadeh-Khouei, J., & Clarke, D. 1993, A&A, 274, 968
Ngoc, N. B., Diep, P. N., Hoang, T., et al. 2023, ApJ, 953, 66
Ossenkopf, V., & Henning, T. 1994, A&A, 291, 943
Ostriker, E. C., Stone, J. M., & Gammie, C. F. 2001, ApJ, 546, 980
Padoan, P., Goodman, A., Draine, B. T., et al. 2001, ApJ, 559, 1005
Palmeirim, P., André, P., Kirk, J., et al. 2013, A&A, 550, A38
Panopoulou, G., Tassis, K., Blinov, D., et al. 2016, MNRAS, 462, 2011
Panopoulou, G. V., Psaradaki, I., & Tassis, K. 2016, MNRAS, 462, 1517
Paré, D., Butterfield, N. O., Chuss, D. T., et al. 2024, ApJ, 969, 150
Paré, D. M., Chuss, D. T., Karpovich, K., et al. 2025, ApJ, 978, 28
Pattle, K., & Fissel, L. 2019, FrASS, 6, 15

Pattle, K., Fissel, L., Tahani, M., Liu, T., & Ntormousi, E. 2023, in ASP Conf. Ser. 534, Protostars and Planets VII, ed. S. Inutsuka et al. (San Francisco, CA: ASP), 193
Pattle, K., Lai, S.-P., Hasegawa, T., et al. 2019, ApJ, 880, 27
Pattle, K., Lai, S.-P., Wright, M., et al. 2021, MNRAS, 503, 3414
Pattle, K., Ward-Thompson, D., Berry, D., et al. 2017, ApJ, 846, 122
Pelkonen, V. M., Juvela, M., & Padoan, P. 2009, A&A, 502, 833
Perault, M., Omont, A., Simon, G., et al. 1996, A&A, 315, L165
Peretto, N., & Fuller, G. A. 2009, A&A, 505, 405
Pilbratt, G. L., Riedinger, J. R., Passvogel, T., et al. 2010, A&A, 518, L1
Pillai, T., Kauffmann, J., Tan, J. C., et al. 2015, ApJ, 799, 74
Pillai, T., Wyrowski, F., Carey, S. J., & Menten, K. M. 2006a, A&A, 450, 569
Pillai, T., Wyrowski, F., Menten, K. M., & Krügel, E. 2006b, A&A, 447, 929
Pillai, T. G. S., Clemens, D. P., Reissl, S., et al. 2020, NatAs, 4, 1195
Pillsworth, R., & Pudritz, R. E. 2024, MNRAS, 528, 209
Pillsworth, R., Roscoe, E., Pudritz, R. E., & Koch, E. W. 2025, ApJ, 987, 20
Planck Collaboration, Ade, P. A. R., Aghanim, N., et al. 2011, A&A, 536, A1
Planck Collaboration, Ade, P. A. R., Aghanim, N., et al. 2014, A&A, 571, A9
Planck Collaboration, Ade, P. A. R., Aghanim, N., et al. 2015a, A&A, 576, A104
Planck Collaboration, Ade, P. A. R., Aghanim, N., et al. 2015b, A&A, 576, A106
Planck Collaboration, Ade, P. A. R., Aghanim, N., et al. 2016, A&A, 586, A138
Planck Collaboration, Aghanim, N., Akrami, Y., et al. 2020a, A&A, 641, A1
Planck Collaboration, Aghanim, N., Akrami, Y., et al. 2020b, A&A, 641, A3
Planck Collaboration, Aghanim, N., Akrami, Y., et al. 2020c, A&A, 641, A12
Price, S. D., Egan, M. P., Carey, S. J., Mizuno, D. R., & Kuchar, T. A. 2001, AJ, 121, 2819
Ragan, S. E., Henning, T., Tackenberg, J., et al. 2014, A&A, 568, A73
Reid, M. J., Dame, T. M., Menten, K. M., & Brunthaler, A. 2016, ApJ, 823, 77
Reid, M. J., Menten, K. M., Brunthaler, A., et al. 2019, ApJ, 885, 131
Rieke, G. H., Young, E. T., Engelbracht, C. W., et al. 2004, ApJS, 154, 25
Robitaille, T., & Bressert, E., 2012 APLpy: Astronomical Plotting Library in Python, Astrophysics Source Code Library, ascl:1208.017
Robitaille, T., Deil, C., & Ginsburg, A., 2020 reproject: Python-based astronomical image reprojection, Astrophysics Source Code Library, ascl:2011.023
Sadavoy, S. I., Di Francesco, J., Johnstone, D., et al. 2013, ApJ, 767, 126
Sanhueza, P., Contreras, Y., Wu, B., et al. 2019, ApJ, 886, 102
Sanhueza, P., Jackson, J. M., Foster, J. B., et al. 2012, ApJ, 756, 60
Serkowski, K. 1958, AcA, 8, 135
Sewilo, M., Watson, C., Araya, E., et al. 2004, ApJS, 154, 553
Skrutskie, M. F., Cutri, R. M., Stiening, R., et al. 2006, AJ, 131, 1163
Soam, A., Pattle, K., Ward-Thompson, D., et al. 2018, ApJ, 861, 65
Stephens, I. W., Coudé, S., Myers, P. C., et al. 2025, ApJ, 995, 181
Stephens, I. W., Looney, L. W., Dowell, C. D., Vaillancourt, J. E., & Tassis, K. 2011, ApJ, 728, 99
Stephens, I. W., Myers, P. C., Zucker, C., et al. 2022, ApJL, 926, L6
Svoboda, B. E., Shirley, Y. L., Battersby, C., et al. 2016, ApJ, 822, 59
Tahani, M. 2022, FrASS, 9, 940027
Tahani, M., Bastien, P., Furuya, R. S., et al. 2023, ApJ, 944, 139
Tan, J. C., Beltrán, M. T., Caselli, P., et al. 2014, in Protostars and Planets VI, ed. H. Beuther et al. (Tucson, AZ: Univ. Arizona Press), 149
Tomisaka, K. 2014, ApJ, 785, 24
Tomisaka, K. 2015, ApJ, 807, 47
Tram, L. N., Hoang, T., Lee, H., et al. 2021a, ApJ, 906, 115
Tram, L. N., Hoang, T., Lopez-Rodriguez, E., et al. 2021b, ApJ, 923, 130
Tram, L. N., Hoang, T., Wiesemeyer, H., et al. 2024, A&A, 689, A290
Urquhart, J. S., Figura, C. C., Moore, T. J. T., et al. 2014, MNRAS, 437, 1791
Urquhart, J. S., Hoare, M. G., Purcell, C. R., et al. 2009, A&A, 501, 539
Vallée, J. P. 2008, AJ, 135, 1301
Vidal, M., Leahy, J. P., & Dickinson, C. 2016, MNRAS, 461, 698
Wang, K., Testi, L., Burkert, A., et al. 2016, ApJS, 226, 9
Wang, K., Testi, L., Ginsburg, A., et al. 2015, MNRAS, 450, 4043
Wang, K., Zhang, Q., Testi, L., et al. 2014, MNRAS, 439, 3275
Ward-Thompson, D., Pattle, K., Bastien, P., et al. 2017, ApJ, 842, 66
Wardle, J. F. C., & Kronberg, P. P. 1974, ApJ, 194, 249
Wright, E. L., Eisenhardt, P. R. M., Mainzer, A. K., et al. 2010, AJ, 140, 1868
Wu, Y. W., Sato, M., Reid, M. J., et al. 2014, A&A, 566, A17
Zhang, M., Kainulainen, J., Mattern, M., Fang, M., & Henning, T. 2019, A&A, 622, A52
Zhao, B., Pudritz, R. E., Pillsworth, R., Robinson, H., & Wadsley, J. 2024, ApJ, 974, 240
Zucker, C., Alves, J., Goodman, A., Meingast, S., & Galli, P. 2023, in ASP Conf. Ser. 534, Protostars and Planets VII, ed. S. Inutsuka et al. (San Francisco, CA: ASP), 43
Zucker, C., Battersby, C., & Goodman, A. 2015, ApJ, 815, 23
Zucker, C., Battersby, C., & Goodman, A. 2018, ApJ, 864, 153
Zucker, C., Smith, R., & Goodman, A. 2019, ApJ, 887, 186